

GLOBAL MODELING OF NEBULAE WITH PARTICLE GROWTH, DRIFT AND EVAPORATION FRONTS. I: METHODOLOGY AND TYPICAL RESULTS

PAUL R. ESTRADA

Carl Sagan Center, SETI Institute, 189 N. Bernardo Ave. # 100, Mountain View, CA 94043

JEFFREY N. CUZZI

Ames Research Center, NASA; Mail Stop 245-3, Moffett Field, CA 94035

AND

DEMITRI A. MORGAN

USRA, NASA Ames Research Center, Mail Stop 245-3, Moffett Field, CA 94035

Draft version December 22, 2015

ABSTRACT

We model particle growth in a turbulent, viscously evolving protoplanetary nebula, incorporating sticking, bouncing, fragmentation, and mass transfer at high speeds. We treat small particles using a moments method and large particles using a traditional histogram binning, including a probability distribution function of collisional velocities. The fragmentation strength of the particles depends on their composition (icy aggregates are stronger than silicate aggregates). The particle opacity, which controls the nebula thermal structure, evolves as particles grow and mass redistributes. While growing, particles drift radially due to nebula headwind drag. Particles of different compositions evaporate at “evaporation fronts” (EFs) where the midplane temperature exceeds their respective evaporation temperatures. We track the vapor and solid phases of each component, accounting for advection and radial and vertical diffusion. We present characteristic results in evolutions lasting 2×10^5 years. In general, (a) mass is transferred from the outer to inner nebula in significant amounts, creating radial concentrations of solids at EFs; (b) particle sizes are limited by a combination of fragmentation, bouncing, and drift; (c) “lucky” large particles never represent a significant amount of mass; and (d) restricted radial zones just outside each EF become compositionally enriched in the associated volatiles. We point out implications for mm-submm SEDs and inference of nebula mass, radial banding, the role of opacity on new mechanisms for generating turbulence, enrichment of meteorites in heavy oxygen isotopes, variable and nonsolar redox conditions, primary accretion of silicate and icy planetesimals, and the make-up of Jupiter’s core.

Keywords: accretion, accretion disks – planets and satellites: formation – protoplanetary disks

1. INTRODUCTION

The very early evolution of solids, as they first decouple from cosmic gas in the protoplanetary nebula and grow into planetesimals such as we see today (asteroids and TNOs) remains poorly understood. We call this stage of growth *primary accretion*. The physics of subsequent or *secondary accretion* by mutual collisions (including gravitational effects) and sweepup of smaller objects is better understood and the process is more well characterized (for a recent review, see, e.g., Raymond et al. 2014). In this stage, gravitational focusing by larger objects (so-called runaway accretion) has traditionally played a dominant role, and nebula gas a lesser role, but recently it has been shown that gas can play an important role even during this secondary stage (Ormel & Klahr 2010; Lambrechts & Johansen 2012). Either way, studies of secondary accretion generally make arbitrary assumptions regarding the sizes of the primary bodies that provide their initial conditions.

Pioneering studies by Weidenschilling (1980, 1984, 1988), Meakin & Donn (1988), Weidenschilling et al. (1989), Donn (1990), Blum & Münch (1993), Dominik & Tielens (1997), Blum & Wurm (2000), Blum et al. (2000) and others since (see Testi et al.

2014, and Johansen et al. 2014, 2015 for reviews including more recent references) have illustrated the importance of the messy physics of sticking and bouncing of grainy, porous, irregular particles. Weidenschilling (1984) recognized the important role of gas turbulence and the great difficulty of forming large objects by “incremental growth”¹ in the presence of turbulence, due to a combination of fragmentation, slow growth, and rapid radial drift. Consequently, nearly all Weidenschilling’s subsequent models (Weidenschilling 1997, 2000, 2004, 2011) have emphasized conditions where global nebula gas turbulence is vanishingly small, allowing a dense layer of particles to settle to the midplane; this layer itself is stirred by a small amount of self-generated turbulence (Weidenschilling 1980; Cuzzi et al. 1993, 1994; Weidenschilling 1995; Barranco 2005; Johansen et al. 2006; Bai & Stone 2010), which is however insufficient to suppress incremental growth by sticking.

The possibility of such a nonturbulent environment has also motivated a completely different approach to primary accretion through various kinds of midplane parti-

¹ We define incremental growth as slow and steady growth by particles of a given size to larger sizes, by simple physical collision and sticking of same-and-smaller-size particles.

cle layer instabilities (Safronov 1972, Goldreich & Ward 1973, Sekiya 1983 *et seq.*, Garaud & Lin 2004, Goodman & Pindor 2000, Youdin & Goodman 2005, and subsequent workers). In these models, the uncertain properties of sticking are ultimately made irrelevant by the dominant role of local gravitational and/or drag instabilities which lead directly to km-and-larger planetesimals (see Chiang & Youdin 2010 for a review that emphasizes work of this type). Midplane instability models all require significant *initial* enhancements of the midplane solids-to-gas ratio before they can operate. Because settling of particles into dense midplane layers is frustrated by turbulent vertical diffusion, this requirement in turn places restrictive conditions on the level of global turbulence and/or global mass enhancement, especially for the mm-size particles that dominate primitive asteroids (for a discussion, see Cuzzi & Weidenschilling 2006).

The level of global nebula turbulence remains very much a matter of active debate. While the predictions of recent MHD models have been trending towards very low intensity near-midplane turbulence (Bai & Stone 2013; Bai 2014), purely hydrodynamical turbulence has been making a comeback (Nelson et al. 2013; Marcus et al. 2013, 2014; Stoll & Kley 2014, see Turner et al. (2014) for a review). Moreover, a number of meteoritic and cometary properties point to an extended period of asteroid formation (Connelly et al. 2012; Kita & Ushikubo 2012; Kita et al. 2013) and an extended radial range of mixing of mineral constituents (Zolensky et al. 2006; Jozwiak et al. 2012), which are both difficult to reconcile with a globally nonturbulent nebula in the region of planetesimal formation. It seems appropriate to face the implications of moderate turbulence squarely, including the various barriers it presents to incremental growth.

Once particles grow into the cm-m size range, depending on location, they drift radially at a rapid pace because of headwind drag with the more slowly rotating, pressure-supported gas (Weidenschilling 1977; Cuzzi & Weidenschilling 2006; Weidenschilling 2006; Johansen et al. 2014). This drift can potentially transport particles great distances while they grow only slowly, because turbulence stirs their “feedstock” and leads to collision velocities which are erosive or destructive. Because particles found at any distance from the sun may have originated at greater distances, proper models should ideally treat the entire radial extent of the nebula at once.

Early global models with growth and drift were presented by Stepinski & Valageas (1996, 1997) and Kornet et al. (2004), but these were simplified in several ways. Ciesla & Cuzzi (2006) studied the implications of drift with simplified growth models, and Garaud (2007) developed a more comprehensive model including an evolving nebula with several volatile species, but still with a simplified growth model. Brauer et al. (2008) were the first to present a complete global (1D) model of particle growth and drift with a detailed model of sticking, which was enabled by an elaborate implicit numerical solution to the cumbersome coagulation equation. They demonstrated, described, and motivated the various barriers to growth (both fragmentation and drift), while assuming a steady-state, non-evolving gas disk. Hughes & Armitage (2010, 2012) presented models with evolving gas disks, but a very simple sticking algorithm

emphasizing the possible differences between viscosity ν and the diffusivity D . Birnstiel et al. (2010, 2011, 2012a) extended the Brauer results to evolving disks, using their implicit numerical approach, and added several new aspects, including composition-dependent sticking (ice *vs.* silicate); their particle collision velocities remained single-valued as a function of particle size, following Ormel & Cuzzi (2007). Their model opacity did not account for the evolving particle size distribution, and the only evaporation they included was the silicate evaporation front at 1500K where all the solids evaporated. There was no explicit treatment of the behavior of vapor of different species.

In the last decade or so, a large and still growing body of experimental work has clarified and refined sticking coefficients for granular particles of various composition, porosity, and relative velocity (Güttler et al. 2010). The most detailed coagulation models which employ this detailed sticking physics encounter a “bouncing barrier” for mm-cm size particles in moderate turbulence (Zsom et al. 2010). This means that, while small particles can grow by sticking because their collision velocities are very small, the very act of growing leads them to acquire relative velocities in turbulence (Völk et al. 1980; Carballido et al. 2008, 2010; Pan & Padoan 2010, 2013, 2014; Hubbard 2012, 2013; Pan et al. 2014a,b) that exceed the sticking threshold at fairly small sizes - in the mm-cm range at 2.5AU. This “bouncing barrier” is in intriguing agreement with the sizes of ubiquitous “chondrules” dominating primitive meteorites, but it poses a problem for actually forming the asteroidal parents of those very meteorites. Sophisticated variants of this model showed that weak dm-size agglomerates of dust-rimmed “chondrules” could be formed, but only in very low levels of nebula turbulence (Ormel et al. 2008). Windmark et al. (2012a,b), Garaud et al. (2013), and Drazkowska et al. (2013, 2014) refined collision models to include a probability distribution function (PDF) for collision velocity, adding a growth path involving fragmentation of a smaller projectile along with mass transfer to a larger target (Wurm et al. 2005; Beitz et al. 2011). They all found that some very few “lucky” large particles could form, although the quantitative details were found to be highly sensitive to the numerics of mass histogram binning. However, these studies either neglected the radial headwind drift or assumed arbitrary radial “pressure bumps” to prevent it, thus giving only an upper limit on the abundance of large “lucky” particles. Our models include not only bouncing and partial or total fragmentation effects, mass- and velocity-dependent sticking coefficients, velocity PDFs and “lucky” particles, but also include full radial drift and a viscously evolving background gas nebula (section 2).

Sticking properties also depend on particle composition. From laboratory studies and material properties, it is becoming clear that where temperatures are low enough for water ice or methanol to form, sticking is significantly more effective (Bridges et al. 1996; Wada et al. 2009), so larger and stronger particles can grow more robustly (Okuzumi et al. 2012). Thus, accretion might operate differently inside and outside of the “snowline”, strengthening the need for global models. Growth might be faster in the cold outer regions, even while subsequent

radial drift might carry this material to the inner solar system where the now ice-free refractory material might grow less robustly. Our models include these material-dependent sticking properties.

Of course, the nebula is warmer at smaller radial distances from the sun, due to a combination of solar heating and viscous dissipation. Drifting particles do not just get “lost to the sun” but evaporate their volatiles along the way (Morfill & Völk 1984; Hueso & Guillot 2003; Cuzzi & Zahnle 2004; Kornet et al. 2004; Ciesla & Cuzzi 2006; Garaud 2007). Each volatile, including ices and silicates, has its own *Evaporation Front* (EF) and our model treats them all. Such EFs have a number of important implications, creating deviations from some uniform “cosmic” abundance of the different materials. Amongst the meteoritical implications of such deviations are the enrichment of nebula vapor in H_2O , with chemical and mineralogical implications (Fedkin & Grossman 2006), and the transport of O-isotopes formed and frozen out in the outer nebula to the inner nebula where they can become incorporated into meteorites (Yurimoto et al. 2007). Each of these processes has a timescale associated with it (now poorly known), that can in principle be modeled and tied to meteoritical data. In studies of other materials besides H_2O , Pasek et al. (2005) and Ciesla (2015) have modeled variable sulfur chemistry, and Yang & Ciesla (2012) have modeled temporal and radial variations of the nebula D/H ratio due to transport, but in neither case were radial drift of large particles included. It is a goal of our models to treat these processes.

In calculating the thermal evolution of the nebula, our model incorporates two other significant advances. First, the nebula opacity is calculated self-consistently as particles grow (Sec. 2.3.2). This is very important because once a particle exceeds the typical wavelength of thermal emission, its opacity decreases linearly with its radius. In all other models to date, either ISM (tiny grain) opacities are assumed even while we know growth must be occurring, or some other arbitrary “representative” value of opacity is assumed. Secondly, we model the plausible luminosity evolution of the early sun. In the first 10^5 - 10^6 years of its life, the sun’s luminosity is $10\times$ to $3\times$ larger than its main sequence value (Kusaka et al. 1970; D’Antona & Mazzitelli 1994). Naturally this will have implications for the locations of the “snowline” and other evaporation fronts.

In addition to the bouncing, fragmentation, and radial drift barriers (which are driven by aerodynamical forcing of particle velocities by eddies on a range of scales), turbulent nebulae present one additional barrier to incremental growth. In global turbulence, small gas *density* fluctuations associated with pressure fluctuations amongst large scale eddies gravitationally excite random velocities of objects in the km- and larger size range, much like giant molecular clouds scatter stars in our galaxy. These relative velocities actually increase with planetesimal size because of the slower damping for larger objects (Nelson & Gressel 2010; Gressel et al. 2012). Ida et al. (2008) showed that these velocities are strongly disruptive for $1 - 10$ km objects for nominal levels of nebula turbulence (objects of 100km size and larger are stabilized by their own self gravity). This serial gauntlet of barriers to growth in turbulence was discussed

further by Ormel & Okuzumi (2013) and Johansen et al. (2014).

Recent years have seen the emergence of “leapfrog” models that circumvent *all* these barriers, producing 10-100km size primitive bodies directly, in one stage, from mm-dm size objects. A discussion of these models (Cuzzi et al. 2001, 2008, 2010, 2014b; Cuzzi & Hogan 2012; Johansen et al. 2007, 2009, 2011; Chambers 2010; Carrera et al. 2015) is beyond the scope of this paper (for a recent review, see Johansen et al. 2015) but they share a preference for local enhancement of solids over the cosmic abundance ratio by factors of 10 or more. It is possible that radial drift can scavenge the outer reaches of the nebula, and contribute to such an enhancement of solids in the inner nebula; even the region of TNO formation might, in principle, be augmented in solids by strong radial drifts scavenging the rarefied outer nebula at hundreds of AU from the sun (Stepinski & Valageas 1996, 1997; Hughes & Armitage 2010, 2012). It may even be that such radial redistribution might lead to the “stubby” radial distribution of solids that Desch (2007) noted is the implication of pre-migration planetary distributions. Ciesla & Cuzzi (2006) found only small degrees of enhancement for the inner solar system, but they made several simplifying assumptions. In this paper we discuss the possibilities for large-scale rearrangement of the solids-to-gas ratio in the nebula, as a function of time.

Given the wide range in timescales associated with modeling the nebula over its entire radial extent, which could extend to as much as ~ 1000 AU, coupled with the computationally expensive implementation of the collisional coagulation equation (Smoluchowski 1916) has previously made such modeling efforts prohibitive. This has typically restricted global models to, for example, either studying dust growth and redistribution alone (e.g., Brauer et al. 2008; Birnstiel et al. 2010), or studying compositional enhancements at evaporation fronts (EFs) due to simplified assumptions about growth (e.g., Cuzzi & Zahnle 2004; Ciesla & Cuzzi 2006; Garaud 2007) or ones that treat growth more carefully, but neglect radial drift (Windmark et al. 2012a,b; Garaud et al. 2013). Taken together these processes are likely to be critical to the evolutionary history of solids and condensibles.

Our model incorporates what may be an even faster numerical approach than that of Brauer et al. (2008) (the method of moments, see section 2.4) which avoids direct calculations of the detailed size distribution for small particles, while still continuing to treat the larger particles explicitly with detailed size, strength, and relative velocity distributions, and our opacity uses the local, evolving size distribution. It is the large particles that are of most interest for radial transport of solids, and it is the details of *their* sizes that may ultimately distinguish between various proposed “leapfrog” models of planetesimal formation, so they receive a higher-fidelity treatment using the full coagulation equation.

2. NEBULA MODEL

The simulations presented in this paper are done using a new $1 + 1\text{D}$ radial nebula code that is capable of simultaneously treating particle growth and radial migra-

Table 1
Selected Symbols and Parameters used in this paper

Symbol	Definition	Section
c	gas sound speed	sec. 2.1
$D_{v,d}$	(vapor, “dust”) diffusion coefficient	Sec. 2.2.2
h_d	effective vertical scale height of “dust” subdisk	Sec. 2.2.3
i, j, k	indices for species, radial bin, and mass	Sec. 2
L_*	time variable stellar luminosity	Sec. 2.3.1
m, m', m_k	particle mass	Sec. 2.4
m_*, r_*	fragmentation mass and radius	Sec. 2.4.2
$\dot{M}, \dot{M}_i^{v,d}$	mass accretion rate, general and for species i vapor and dust	Sec. 2.1, b.2
M_D	initial disk mass	sec. 2.1
M_k^m	total mass of “migrators” m_k in a radial bin	Sec. 2.4.4
Q_T, Q_d	Toomre parameters for gas and particle subdisk	Sec. 2
Q_*, C_0	specific energy for fragmentation and bouncing	Sec. 2.4.2
Q_a, Q_s, Q_e, Q'_e	radiation transfer efficiencies of particles	Appendix A.3
R, R_0	radial coordinate, and initial disk radius	Sec. 1, 2.1
r, r_k	particle radii, general or for mass m_k	Sec. 2.1, 2.4
r_M	radius of particle containing most mass in radial bin	Sec. 2.4.6
r_L	radius of largest particle in radial bin	Sec. 2.4.1, 3.1.1
St, St_L, St_M	particle Stokes number = $t_s \Omega$	Sec. 2.2.1, 3.2
St_*, St_b, St_d	fragmentation, bouncing and drift Stokes numbers	Sec. 3.2, 4.2
$S_{b,*}(m, m'); S_{k,l}$	sticking coefficients for bouncing or fragmentation	Sec. 2.4.2, 2.4.4
T, T_{ph}	disk midplane and photospheric temperature	Sec. 2.3.1
t_s	particle stopping time	Sec. 2.2.1
u, v	gas radial and azimuthal velocity	Sec. 2.4.3
U_k, V_k	radial and azimuthal velocity for mass m_k	Sec. 2.4.3
V_{rad}	radial drift velocity of m_k	Sec. 2.2.2, 2.4.5, Eq. 51
\tilde{V}_g	viscous accretion velocity of nebula gas	Sec. 2.1, Eqs. 2, 6
$V_{v,d}$	radial drift velocity (vapor, mass-weighted solid)	Sec. 2.2.2
α_t	turbulence parameter	Sec. 2.1
$\alpha_i^{v,d}$	(vapor, solid) mass fraction in species i	Sec. 2.2
$\Delta t_{min}, \Delta t_{sync}$	minimum code timestep and synchronization timestep	Sec. 2
ΔV_{pg}	particle-gas relative velocity	Sec. 2.4.2, 2.4.3
$\Delta V_{pp}, \Delta V_{k,l}^{pp}$	particle-particle relative velocity	Sec. 2.4.2, 2.4.3, 2.4.4
κ	Rosseland mean opacity	sec. 2.3.1, 2.3.2, Appendix A.3
λ_{mfp}	molecular mean free path	Sec. 2.2.1
ν, ν_m	turbulent and molecular viscosity	Sec. 2.1
Ω	Keplerian orbit frequency	Sec. 1, 2
ρ	gas mass density	Sec. 2.1
ρ_d^d	“dust” particle mass density for mass m_k	Sec. 2.2.2, 2.4.3
ρ_k^d	“migrator” particle mass density for mass m_k	Sec. 2.4.4
ρ_k^m	particle material (internal) mass density	Sec. 2.4.1
ρ_p	volume mass density of solids in “dust” population	Sec. 2.2.2
ρ_d	collision cross section	Sec. 2.4.2, 2.4.4
$\sigma, \sigma(m, m')$	gas surface mass density	Sec. 2
Σ	(vapor, solid) surface mass density in species i	Sec. 2.2.2
$\Sigma_i^{v,d}$	optical depth at thermal wavelengths = $\kappa \Sigma$	Sec. 2.3.1
τ		

tion over many decades of particle size, while simulating the dynamical and thermal evolution of the circumstellar gas disk. Our model includes self-consistent growth and radial drift of particles of all sizes, accounts for the vertical diffusion and settling of smaller grains, radial diffusion and advection of dust and vapor phases of multiple species, and a self-consistent calculation of opacity and disk temperature which allows us to track the evaporation and condensation of the various species as they are transported throughout the disk. Our code is parallelized in radial bins which is a natural step in attacking problems of this magnitude. The development of further innovations and techniques to treat some of the more computationally expensive processes helps to make the problem even more tractable up to and including additional parallelization in mass bins.

In our code, several indices will be used. In general, we reserve the index j to refer to quantities that are functions of semimajor axis, k will be used to refer to the histogram of particle masses, whereas the index i

will exclusively be used for compositional species. As the need arises for additional indices, we assign the index l for dummy variables. For our model variables, a lack of subscript generally refers to a nebular quantity such as the gas surface density Σ , or the pressure scale height H . The subscripts or superscripts d, v or m refer to properties of the dust, vapor or migrators as described in the following sections. We specifically draw attention to the fact that there are many different velocities that will be discussed in this paper; the ones most widely used are referenced in **Table 1**. Finally, quantities that can be generally referred to will be done so using a subscript, such as the total volume density of solid material ρ_d , whereas the same quantity that is specific to a radial bin will have the subscript transposed to a superscript with the index used as the subscript, e.g., ρ_j^d . Most of the relevant parameters used in our code are summarized in Table 1.

We define the minimum time step Δt_{min} in our code to be a fraction of the innermost radial bin’s orbital pe-

riod $P = 2\pi/\Omega$, where $\Omega = \sqrt{GM_\star/R^3}$ is the orbital frequency, M_\star is the stellar mass, G is the gravitational constant, and R is the semi-major axis. This presents a dilemma in that the dynamical times in the innermost portions of the disk where evolution generally happens more quickly can be orders of magnitude shorter than those in the outer regions of the disk. Using the same time step globally is thus inefficient.

In order to somewhat circumvent this problem, we employ an asynchronous time stepping scheme which works as follows. Each radial location in the disk R has its own time step Δt associated with it that is the same fraction of its orbital period as is Δt_{\min} . We compare the time “elapsed” in a radial bin with the total simulation time $t_{\text{sim}} = I\Delta t_{\min}$, where I is the number of iterations the code has currently executed. If a bin has executed N steps, then its next execution will occur if $(N+1)\Delta t \leq I\Delta t_{\min}$. When the condition is satisfied, the counter N is incremented by 1 and a time step is executed for that bin. In this fashion the global “time step” for the code is the fraction of the orbital period we choose, usually $\leq P/4$. The innermost radial bin is called every iteration, but we avoid unnecessary calls to other radial bins.

Having each radial location effectively at a different evolutionary time poses a problem for the transport of material across radial boundaries, either through diffusion or radial drift. We thus introduce the concept of the “synchronization time”, a predefined number of steps N_{sync} in which we periodically bring the simulation to the same time globally. When $\text{MOD}(I, N_{\text{sync}}) = 0$, all radial bins are executed with the time step $\Delta t_{\text{sync}} = N_{\text{sync}}\Delta t_{\min} - N\Delta t$. In this paper we choose values $N_{\text{sync}} \leq 100$. During the synchronization step we execute global calculations such as the nebula gas evolution (Sec. 2.1), solve the diffusion-advection equation (Sec. 2.2), determine the disk temperature (Sec. 2.3.1) and write out simulation data. On the other hand, radial drift of material can be on time scales which are quite fast so that waiting for a synchronization step is not practical. Instead, we have developed a method to account for radial drift that is called at all Δt (Sec. 2.4.5). Once a synchronization step is completed, the time counters (I, N) are set back to zero. In full global simulations, this synchronization step will still happen much sooner than an orbit period in the outermost portions of the disk, but the savings in time can be significant.

2.1. Gas Evolution

For this work, we use a radial 1-D model for the time-dependent evolution of the gas surface density $\Sigma(R, t)$ and radial velocity $V_g(R, t)$. In the case that the gravitational potential is due to a central point mass M_\star , the equations for the radial evolution and velocity of the nebula gas under viscosity ν can be derived from the continuity and angular momentum conservation equations, and are given by (Pringle 1981)

$$\frac{\partial \Sigma}{\partial t} = \frac{3}{R} \frac{\partial}{\partial R} \left\{ R^{1/2} \frac{\partial}{\partial R} (R^{1/2} \nu \Sigma) \right\}, \quad (1)$$

$$V_g = -\frac{3}{R^{1/2} \Sigma} \frac{\partial}{\partial R} (R^{1/2} \nu \Sigma). \quad (2)$$

The corresponding disk mass accretion rate is then $\dot{M} = -2\pi R \Sigma V_g$ where the sign is chosen such that a positive value of \dot{M} indicates accretion onto the central star. The total viscosity ν can be related to “ α -models” in which $\nu = \alpha_t c H = \alpha_t c^2 / \Omega$, where α_t parametrizes the turbulent intensity, H is the nebula gas pressure scale height, and the gas sound speed can be expressed in terms of temperature T as

$$c = \left(\frac{\gamma k_B T}{\mu_H} \right)^{1/2}. \quad (3)$$

In Eq. (3) above, k_B is the Boltzmann constant, the adiabatic index $\gamma = 1.4$ for a diatomic gas and $\mu_H = 3.9 \times 10^{-24}$ g is the mean mass per molecule in a mixture of hydrogen gas that has $\sim 20\%$ helium by number.

It is generally assumed that the disk is gravitationally stable to fragmentation. We monitor the stability of the disk in our code through the Toomre parameter (Toomre 1964)

$$Q_T = \frac{c \Omega}{\pi G \Sigma}. \quad (4)$$

Values of Q_T less than unity lead to disk fragmentation, but for values $Q_T \lesssim 2$ the disk is described as weakly unstable and may lead to the formation of clumps. However, these clumps only form if the disk is atypically massive or cold (Rafikov 2005), and unless there are processes to keep the disk unstable, it is assumed that weak gravitational instabilities quickly lead to stabilization of the disk via the excitation of spiral density waves. The process is thus self-limiting to the extent that these waves carry away angular momentum that spread the disk, lowering Σ . If Toomre-unstable conditions arise, we can introduce a moderately large value of α_t until stable conditions resume. In practice, however, this does not happen in the disk models presented in this paper.

We derive initial conditions for our disk models using the analytical expressions from Lynden-Bell & Pringle (1974), as generalized by Hartmann et al. (1998), which are parametrized by some initial disk mass M_D and radius R_0 . In determining the initial gas surface density and radial velocity, the value and radial dependence of the turbulent viscosity is expressed as a general power law of the form $\nu = \nu_0 (R/R_0)^\beta$ (e.g., Hartmann et al. 1998). These assumptions lead to simple 1-D, vertically integrated and averaged expressions which can be readily derived from Hartmann et al. (1998) given here for $t = 0$:

$$\Sigma(R, 0) = \frac{M_D}{\pi R_0^2} \left(\frac{2-\beta}{2} \right) \left(\frac{R}{R_0} \right)^{-\beta} e^{-(R/R_0)^{2-\beta}}; \quad (5)$$

$$V_g(R, 0) = -\frac{3\nu_0}{2R} \left(\frac{R}{R_0} \right)^\beta \left[1 - (4-2\beta) \left(\frac{R}{R_0} \right)^{2-\beta} \right], \quad (6)$$

where $\nu_0 = \alpha_t c_0^2 / \Omega_0$, with all quantities evaluated at R_0 . Typical ranges for the power law exponent that characterize plausible extremes of nebula radial variation are $0 \leq \beta \leq 3/2$ (e.g., Cuzzi et al. 2003). Hartmann et al. (1998) favor $M_D = 0.2 M_\odot$, $R_0 = 10$ AU and $\beta = 1$

based on young star statistics and we use these as fiducial values in this paper. The scale parameter R_0 can also be chosen to match solar system specific angular momentum (Cuzzi et al. 2003, $R_0 = 4.5$) or by other criteria (Yang & Ciesla 2012, $R_0 = 53$). Indeed the nominal value of R_0 has more often been set at larger values 20–60 AU (Ciesla & Cuzzi 2006; Garaud 2007; Brauer et al. 2008; Hughes & Armitage 2012; Yang & Ciesla 2012) than chosen here but the rationale is not always clear. We note that these choices simply provide initial conditions for the disk’s surface density profile in terms of the initial disk mass M_D , and that the viscosity of the disk will in general not follow a single power law distribution – either initially, or as a function of time due to particle growth, changing opacity, and our self-consistent calculation of the disk temperature (see Sec. 2.3). Thus, at subsequent timesteps the actual viscous evolution equations are integrated using the actual local properties. However, as noted in section 4, these choices do influence disk evolution at early times of interest.

2.2. Evolution of Dust and Vapor

A self consistent calculation of the disk temperature requires that we also know the distribution of dust and vapor within the disk, and the initial distribution is established during our first calculation of the disk temperature. Our model is capable of tracking any number of species in both the vapor and solid phase. We define the concentrations of each species i such that

$$\alpha_i^{v,d} = \frac{\Sigma_i^{v,d}}{\Sigma}, \quad (7)$$

is the fractional mass of constituent i , or the ratio of surface density of solids or vapor to the gas surface density. In this paper, we include only five different species which are listed in **Table 2** along with their corresponding condensation temperatures T_i , densities ρ_i and initial concentrations x_i in the solid state. We denote by f_d , f_v and f_m the total fractional amounts of the dust, vapor, and migrator (see Sec. 2.4.4) components within the disk. For instance, $f_d = \sum_i \alpha_i^d$. These quantities are updated locally at every time step Δt , and globally at every synchronization step t_{sync} .

2.2.1. Particle Stokes Number and Stopping Times

Treating the growth and redistribution of solids in the nebula concomitant with its gas and thermal evolution is a key aspect of this work, and is essential for a self-consistent model of the nebula. Initially, the dust-to-gas ratio in the disk is assumed to be of order $\sim 10^{-2}$ which is consistent with values for the ISM. At this average abundance, the mass volume density of solid material ρ_d does not affect the motion of the gas unless settling of dust particles leads to a layer in the midplane with density $\rho_d \geq \rho$, where ρ is the gas mass density (Nakagawa et al. 1986). In fact, we can define an equivalent condition to Eq. (4) for the dust $Q_d = \Omega^2 / \pi G \rho_d$, such that if $Q_d \lesssim Q_T$, the condition for gravitational instability of the dust layer may be satisfied (Safronov 1991; Cuzzi et al. 1993). However, even for $Q_d \gg Q_T$, collectively the dust can play a significant role in the disk’s thermal evolution and thus affect Σ and V_g through the temperature distribution, if a large fraction of the

dust particle sizes remain small such that the opacity remains high (Sec. 2.3.2). In particular, differences in the growth and migration rate, as well as the possibility for evaporation and condensation of solid grains, can lead to significant radial variation in the distribution of solids.

For a large range of solids-to-gas ratios, the influence of the nebula gas on the motion of the particles over the full spectrum of sizes can be described by the dimensionless Stokes number

$$\text{St} \equiv \frac{t_s}{t_{\text{ed}}}, \quad (8)$$

where t_s is the particle stopping time, and t_{ed} is some eddy turnover time, which we choose here to be the integral scale, or turnover time of the largest eddy in the turbulence. This is generally assumed (and has been shown) to be Ω^{-1} for global turbulence (Cuzzi et al. 2001; Johansen et al. 2007; Carballido et al. 2010). The particle stopping time is defined as the time needed for the gas drag force to dissipate a particle’s momentum relative to the gas. The drag force on a particle of radius r depends on the size of the particle relative to the molecular mean free path λ_{mfp} , and can be separated into two distinct flow regimes:

$$t_s = \frac{\rho_p}{\rho} \frac{r}{c} \quad \text{if } r \leq (9/4)\lambda_{\text{mfp}}; \quad (9)$$

$$t_s = \frac{8}{3} \frac{\rho_p}{\rho} \frac{r}{C_d \Delta V_{\text{pg}}} \quad \text{if } r > (9/4)\lambda_{\text{mfp}}, \quad (10)$$

where ρ_p is the particle material density (section 2.4.1). Equation 9 describes the *Epstein flow* regime in which smaller grains are well coupled to the gas flow and relative velocities between grains are small. In the larger particle *Stokes flow* regime (Eq. [10]), particles become increasingly less coupled to the gas flow and their stopping times are affected by the drag coefficient C_d which depends on a particle Reynolds number Re_p that is itself a function of the relative velocity ΔV_{pg} between the particle and the gas (Weidenschilling 1977).

In our code, we calculate the particle-to-gas and particle-to-particle relative velocities over the evolving size distribution which can cover many decades in mass. As growth proceeds to larger sizes, some particles will remain in the Epstein flow regime, while larger ones will be subject to Stokes flow. We use a bridging expression that provides a smooth transition between the two regimes after Podolak et al. (1988). Our treatment of the stopping times is described in further detail in Appendix A.4.

2.2.2. Radial Diffusion-Advection

We determine the radial motion of the solid and vapor fractions of all compositional species by solving the advection-diffusion equation

$$\frac{\partial \Sigma_i^{v,d}}{\partial t} = \frac{1}{R} \frac{\partial}{\partial R} \left\{ R D_{v,d} \Sigma \frac{\partial \alpha_i^{v,d}}{\partial R} - R V_{v,d} \Sigma_i^{v,d} \right\} + S_i, \quad (11)$$

where $\Sigma_i^{v,d}$ is the surface density for dust (d) or vapor (v) of species i , $V_{v,d}$ is a net, inertial space advection velocity, and $D_{v,d}$ is the diffusivity.

Table 2
List of Species

Species	T_{sp} (K)	ρ_{sp} (g cm $^{-3}$)	x_{sp} ($T < T_{\text{sp}}$)
Iron	1810	7.8	1.26×10^{-4}
Silicates	1450	3.4	3.41×10^{-3}
Troilite	680	4.8	7.68×10^{-4}
Organics	425	1.5	4.132×10^{-3}
Waterice	160	0.9	5.55×10^{-3}

The separately treated term \mathcal{S}_i represents sources and sinks for “dust” and vapor for species i which, in our treatment, includes the growth, radial drift and destruction of migrating material (Sec. 2.4.4). The sign of the advection velocity in Eq. (11) is such that $V_{v,d} < 0$ indicates inward radial velocity, and $V_{v,d} > 0$ outward radial velocity.

For the vapor phase, we assume $D_v = D_g = \nu/\text{Sc}_g$ (Hughes & Armitage 2010), where the gas diffusivity D_g is the ratio of the viscosity to the Schmidt number Sc_g (which we take to be unity in this work, see Appendix B) and the vapor advection velocity is just that of the gas; $V_v = V_g$ (equations 2 and 6). The particle diffusivity $D_d = D_g/(1 + \text{St}^2)$ (Youdin & Lithwick 2007; Carballido et al. 2011) and V_d are determined at radius R through a mass-weighted mean of all grain sizes in the dust population (indexed by k):

$$D_d = \sum_k \frac{\rho_k^d}{\rho_d} \left(\frac{D_g}{1 + \text{St}_k^2} \right); \quad (12)$$

$$V_d = \sum_k \frac{\rho_k^d}{\rho_d} V_k^{\text{rad}}, \quad (13)$$

where $\rho_d = \sum_k \rho_k^d$ is the total mass volume density of solids in the subdisk layer (see Sec. 2.2.3). The radial velocity V_k^{rad} in Eq. (13) properly takes into account the radial drift of particles *relative to the gas* due to the local pressure gradient (e.g., Nakagawa et al. 1986; Takeuchi & Lin 2002) and is described in more detail in Sec. 2.4.5 (Eq. [50]).

The sign of the mean radial drift velocity depends on the particle size (large particles drift inwards and small ones are advected outwards). We utilize a power law distribution in particle mass for the dust population with a typical exponent $q = 11/6$, which is representative of a collisional population (see Sec. 2.4.1), so that most of the mass will be in the largest sizes and the mean velocity will always be inward. However, the mass average approach by itself as written in Eq. (13) would fail to take into account that the smallest grains would still move with the gas, and in the outer parts of the disk, this flow may be outward. In order to account for this in our code, we treat the dust as two separate populations and define a mean velocity for each, V_d^+ which characterizes the mass fraction in small particles that move with the gas, and V_d^- which characterizes the larger grains that radially drift inward. Before calculating the mean drift velocities, we determine the grain size that separates the two populations, and define the total fractional mass in each population which is used as a weighting factor when

solving the advection-diffusion equation (see Appendix A.2).

2.2.3. Vertical Diffusion and Subdisk Height

We treat the vertical diffusion and settling of dust grains in the “+1D” part of our code using an analytical solution combining elements of Dubrulle et al. (1995); Cuzzi & Weidenschilling (2006) and Youdin & Lithwick (2007) to calculate the particle distribution as a function of height z in the disk. The vertical scale height h_d of particles with mass m is defined as

$$h_d(m) = H(1 + \text{St}/\alpha_t)^{-1/2}. \quad (14)$$

This solution bears a resemblance to that of Garaud (2007, her Eq. 22) but includes a number of subtleties (see Appendix B).

To calculate a characteristic scale height h_d for the local particle subdisk as a whole, we specify a representative particle mass as either half the fragmentation barrier mass m_* or the largest particle mass $m_L/2$ (if no particles have yet reached m_* ; see Sec. 2.4.2), based on focused 2D calculations that follow growth as a function of height at a given radius R . In future refinements, a value of h_d could be tracked for all particle sizes, giving a complete size distribution as a function of altitude (as for instance in Sec. 2.4.3, Eq. [38]). The relative velocities (Sec. 2.4.3) are also defined at the same representative h_d . The layer of thickness h_d defines the volume accessible to particles growing in the midplane.

2.3. Disk Thermal Evolution

2.3.1. Temperature

We calculate the protoplanetary disk midplane and photosphere temperatures self-consistently, assuming that the nebula is heated by a combination of internal viscous dissipation \dot{E}_ν , at a rate proportional to Σ and ν and thus primarily near the midplane, and external illumination \dot{E}_\star by the stellar luminosity L_\star (which can vary with time; see below). The stellar luminosity heats the upper layers of the disk on both sides, and thus indirectly the material beneath (e.g., Ruden & Pollack 1991; Woolum & Cassen 1999; Ciesla 2010). The thermal energy of the disk is radiated into space from the photosphere at $T_{\text{ph}}(R, t)$, the altitude where the optical depth at thermal wavelengths measured vertically outwards is roughly unity. For cosmic abundance and a standard ISM-MRN grain size distribution, the photosphere lies at a distance $H_{\text{ph}} \sim \pm 3 - 5 H$ from the midplane. On each face of the nebula, we can express the energy balance as $\sigma_{\text{SB}} T_{\text{ph}}^4 = \dot{E}_\nu/2 + \dot{E}_\star$, where σ_{SB} is the Stefan-Boltzmann constant. In reality, the disk has an optically thin hot exosphere (Chiang & Goldreich 1997; Dullemond et al. 2002) which indirectly warms the disk photosphere to T_{ph} , but it can be shown that modeling direct deposition of solar energy at, and thermal radiation by, the disk photosphere leads to the same T_{ph} . Note that Eq. (12a) of Chiang & Goldreich (1997) has an extraneous factor of $2^{1/4}$ which is removed by integration over all angles of the optically thin emission from the superheated exosphere slab, as for instance in Nakamoto & Nakagawa (1994).

We are primarily interested in the midplane temperature T , because planetesimals and boulder-size drifting particles which transport solids radially and feed EFs lie mostly near the midplane and not at high altitudes. The midplane temperature is influenced both by \dot{E}_ν and \dot{E}_\star . The external irradiation is both deposited and re-radiated at the disk photosphere, producing zero net vertical flux through the rest of the disk in steady state and thus a vertically constant temperature below the photosphere in the absence of other energy sources. The energy produced by viscous dissipation must flow vertically away from the midplane (assuming it is primarily produced there, as we do) to the photosphere to be radiated away, leading to a vertical thermal gradient. The resulting temperature distribution depends on whether the disk is optically thick or thin. Nakamoto & Nakagawa (1994) suggest a “bridging” expression that covers both of these regimes (their Eq. A15), which can be simplified to:

$$\sigma_{\text{SB}}T^4 = \left(\frac{3\tau}{8} + \frac{1}{2\tau}\right) \frac{\dot{E}_\nu}{2} + \dot{E}_\star, \quad (15)$$

where τ is the full optical depth of the nebula at thermal wavelengths. Between $\pm H_{\text{ph}}$, $\tau = \kappa\Sigma/2$, where κ is the average thermal opacity. Energy from infall shocks was also included by Nakamoto & Nakagawa (1994), but we do not treat it in this paper.

Comparing Eq. (15) to that for the disk surface shows that the midplane temperature responds differently to internal and external energy sources. Regarding internal sources, most previous workers have treated only the optically thick limit ($3\tau/8$ term above). For instance, Cassen (1994), and Woolum & Cassen (1999) generalized the classical radiative transfer solution for a layer of optical depth $\tau \gg 1$ which they defined from the midplane outwards as $T^4 = (3/4)\tau T_{\text{ph}}^4$. This is the classical Eddington solution where all the energy is produced at the bottom of the layer, and is thus only half of the value in Eq. (15). Cassen (1993; and others subsequently) merely stated that the leading factor of $3/8$ applies to the more realistic situation where the energy production is vertically distributed and roughly proportional to the mass density. The derivation of the $3/8$ factor for the regime of interest can be extracted from Shakura & Sunyaev (1973), and assumes constant κ which, for large optical depths, is the Rosseland mean opacity (see Sec. 2.3.2).

The $1/2\tau$ term in Eq. (15) treats the opposite limit where significant internally generated energy must be radiated away, but the nebula opacity capable of doing this is low, for instance, if most of the grains have evaporated. In this optically thin regime the emitted flux from each face is given by $2\tau\sigma_{\text{SB}}T^4$, where τ is the full optical depth, and the factor of 2 comes from integrating intensity over all angles. In this regime, temperature is roughly independent of altitude ($T \sim T_{\text{ph}}$).

We assume a local, vertically integrated viscous dissipation rate $\dot{E}_\nu = (9/4)\Sigma\nu\Omega^2$ which is closely related to the mass accretion rate (Lin & Papaloizou 1985). Shakura & Sunyaev (1973) note that the local energy production rate \dot{E}_ν differs by a factor of three from the local rate of release of gravitational potential energy. The stellar flux on each disk face is given by

$$\dot{E}_\star = \frac{L_\star\phi}{4\pi R^2} = \phi\sigma_{\text{SB}}T_\star^4 \left(\frac{R_\star}{R}\right)^2, \quad (16)$$

where ϕ is some grazing incidence angle depending on disk geometry, and the stellar luminosity is $L_\star = 4\pi R_\star^2\sigma_{\text{SB}}T_\star^4$, with R_\star and T_\star the stellar radius and photospheric temperature. The incidence angle ϕ which determines the solar disk heating differs considerably between so-called “flat” disks, having photospheric height H_{ph} a constant fraction of the distance R from the star, and “flared” disks where dH_{ph}/dR increases with R , which leads to much larger thickness. Whether the disk is flared or flat has implications for the gas mass densities we use to determine particle interactions, growth and drift (Sec. 2.4.1). For the more realistic flared disks, values of ϕ were derived by Kenyon & Hartmann (1987), and Ruden & Pollack (1991), and reiterated by Chiang & Goldreich (1997), who also derive the general radial variation

$$\phi(R) \sim 0.4 \frac{R_\star}{R} + R \frac{d}{dR} \left(\frac{H_{\text{ph}}}{R}\right) \sim 0.005 R_{\text{AU}}^{-1} + 0.05 R_{\text{AU}}^{2/7}, \quad (17)$$

where R_{AU} is radial distance in AU, and the first term on the RHS is the “flat disk” value (e.g., Adams & Shu 1986). The second term on the RHS can be understood as a manipulated version of the incidence angle at the photosphere of a flared disk given more obviously by $dH/dR - H/R$. Thus the illumination term is dominated by flared disk geometry in general. Iterative treatment of $\phi(R)$, depending on T_{ph} and L_\star , is left for future work.

In one subtle difference, Chiang & Goldreich (1997) and Ruden & Pollack (1991) appear to assume that each disk face sees only half of the stellar flux, while Ciesla (2009, 2010) assumes that the entire star is visible and the flux normal to itself at the disk face is simply $L_\star/4\pi R^2 = \sigma_{\text{SB}}T_\star^4(R_\star/R)^2$. For the entire star to be visible from some point at (R, H_{ph}) , the opaque disk must vanish inside of a radius $R_{\text{min}}(R)$, where the photosphere height is $H_{\text{ph,min}}$, such that

$$\frac{H_{\text{ph,min}} + R_\star}{R_{\text{min}}} \sim \frac{H_{\text{ph}} + R_\star}{R}, \quad (18)$$

so using $H_{\text{ph}}/R \sim 0.2 R_{\text{AU}}^{2/7}$ (Chiang & Goldreich 1997) at both R and R_{min} , we find

$$R_{\text{min}}(R) = R \left[1 + 0.2 \frac{R}{R_\star} R_{\text{AU}}^{2/7}\right]^{-1}. \quad (19)$$

That is, even from a point on the disk photosphere at 3 AU from the star, the entire stellar disk can be seen unless the opaque nebula disk extends further inwards than $3R_\star$, and the stellar disk becomes more visible at larger distances. Thus we will assume the full stellar flux illuminates each face of the disk (this is possible because the disk is flared and not planar). On the other hand, the value of ϕ adopted by Ciesla (2009, 2010) is several times smaller than the values given by Eq. (17) above, reducing the stellar flux accordingly. The equation determin-

ing the midplane temperature must be solved iteratively using a root finding algorithm:

$$\sigma_{\text{SB}} T^4 = \frac{9}{8} \nu \Sigma \Omega^2 \left(\frac{3\tau}{8} + \frac{1}{2\tau} \right) + \frac{L_* \phi}{4\pi R^2}, \quad (20)$$

where the Rosseland mean opacity κ is a function of τ through the τ -dependent (T -dependent) dominant wavelength, the evolving particle size distribution, and the solids fractions of all species i .

We employ a time variable luminosity $L_*(t)$ using the model of D’Antona & Mazzitelli (1994, Table 3) for a $1 M_\odot$ star. We fit a polynomial to these authors’ tabulated values, which cover a time scale of $7 \times 10^4 - 1 \times 10^8$ years after collapse. This gives an initial stellar luminosity of $L_* \approx 12 L_\odot$ at 7×10^4 years, which we use as the starting time for our simulations, dropping to perhaps $3 L_\odot$ at 10^6 years.

2.3.2. Rosseland Mean Opacity

The expressions from Sec. 2.3.1 relating the midplane temperature to the sources of energy assume a wavelength-independent or grey opacity. The transfer of thermal radiation in regions of high optical depth is maximized at wavelengths where opacity is *low*. The standard treatment is to define a Rosseland mean opacity κ from the basic wavelength-dependent opacity κ_λ , weighting the inverse (the transparency) at wavelength λ by the derivative of the Planck function $dB_\lambda(T)/dT$ which manifests the local flux gradient:

$$\kappa^{-1} = \frac{\int \kappa_\lambda^{-1} \frac{dB_\lambda}{dT} d\lambda}{\int \frac{dB_\lambda}{dT} d\lambda} = \frac{\pi}{4\sigma_{\text{SB}} T^3} \int \kappa_\lambda^{-1} \frac{dB_\lambda}{dT} d\lambda. \quad (21)$$

The Planck opacity, which is preferred for low optical depth regions (e.g., Nakamoto & Nakagawa 1994), can be calculated similarly through a straight average of the wavelength-dependent opacities κ_λ as weighted by the Planck function $B_\lambda(T)$. Pollack et al. (1994) show that the distinction between the Rosseland and Planck opacities is not large for small solid particles, and thus as previously stated we include only the Rosseland mean opacity in our temperature calculations.

We utilize a new opacity model in order to determine the κ_λ , which is fully described in Cuzzi et al. (2014; their Appendix A contains a derivation of Eq. [21]), which can be easily incorporated into evolutionary models at little computational cost. We utilize realistic material refractive indices for a cosmic abundance suite that likely characterizes nebula solids: water ice, silicates, refractory organics, iron sulfide and metallic iron (summarized in Table 2). These indices and relative abundances are taken from Pollack et al. (1994), but alternate tabulations can readily be used in our code (e.g., Draine & Lee 1984; Henning et al. 1999). We briefly summarize how the opacity model of Cuzzi et al. (2014a) is applied in our model in Appendix A.3.

2.4. Solid Body Growth

Global modeling of the aggregation and radial evolution of solids in the protoplanetary nebula is required over time scales of millions of years in order to understand many key aspects of primitive bodies. A key

feature of our model is the capability of modeling particle growth over many decades of particle size, from sub-micron-sized dust to meter-sized and larger boulders which can radially drift large distances as they grow.

Growth by sticking in the protoplanetary disk starts with sub-micron grains which are dynamically coupled to the nebula gas, and proceeds incrementally through larger sizes that collide at larger relative velocities (Sec. 2.4.3). The growth of aggregates continues at a rate determined by local nebula conditions until some “bouncing barrier” is reached where collisional energy cannot be dissipated, but remains inadequate to destroy the colliding particles (see Sec. 1). The particle size where this occurs depends on assumed particle strength and the local value of turbulent α_t .

The bouncing barrier is not impermeable, but merely slows growth by restricting collision partners. Growth beyond the bouncing barrier may continue by accretion of sufficiently smaller particles, through a transition regime of “sub-migrators” where particles are highly susceptible to mutual collisional destruction (fragmentation) as they drift radially, to “migrators” which have grown large enough to have a much lower probability of destruction (Estrada & Cuzzi 2009). The latter particles can drift large distances and grow further, perhaps even into planetesimals.

The treatment of growth up to the bouncing and/or fragmentation barriers has until recently presented the most significant challenge, because a full-scale solution to the problem of dust coagulation for a size spectrum at every spatial location in the disk, and as a function of time, has been computationally prohibitive, and as a result previous models have been limited in different ways (see Sec. 1). Growth through the transitional sub-migrator and migrator regimes between dust and planetesimals, and associated radial drift over long times, is even less thoroughly studied. In our model, we use the moments method of Estrada & Cuzzi (2008) to greatly accelerate coagulation modeling up to the bouncing barrier, as described below in Sec. 2.4.1. Growth beyond the bouncing barrier through the transitional regimes is treated explicitly in the traditional way, as described in Sec. 2.4.4.

In this paper we do not treat collective concentration or sweepup effects such as streaming instabilities (Goodman & Pindor 2000; Youdin & Goodman 2005, see however, Sec. 4.2), turbulent concentration (Cuzzi et al. 2008, 2010), or “pebble accretion” (Ormel & Klahr 2010; Lambrechts & Johansen 2012). All these subsequent processes depend strongly on initial local conditions (primarily, particle size and abundance) which are determined by sticking for some given α_t in the presence of drift, and it is those conditions which are the outcome of the models described here.

2.4.1. Coagulative Grain Growth

The standard approach to modeling dust coagulation involves solving some form of the collisional coagulation equation (Smoluchowski 1916)

$$\frac{df(m, t)}{dt} = \frac{1}{2} \int_0^m K(m - m', m') f(m - m', t) \times f(m', t) dm' - \int_0^\infty K(m, m') f(m, t) f(m', t) dm', \quad (22)$$

where $f(m, t)$ is the particle number density per unit mass for mass m , and the collisional kernel $K(m, m')$ contains all of the relevant information about the interacting masses m and m' , such as their mutual relative velocities, collisional cross-sections, and sticking efficiencies, and can include other properties such as particle porosities (e.g., see Estrada & Cuzzi 2008). The difficulty with the application of Eq. (22) that has made global models of nebula evolution intractable is that the calculation is computationally expensive. Coagulative grain growth can span many decades of particle mass which may require $\sim 10^2 - 10^3$ bins or more depending on desired accuracy, and at least the first integral of Eq. (22) must be solved for *each* mass bin, thus solving Eq. (22) at every spatial location and at every time step can become intractable. It has been shown that taking shortcuts with the number of mass bins risks producing artificial growth.

Estrada & Cuzzi (2008, 2009) developed a scheme for modeling coagulative growth that overcomes these difficulties and that lends itself quite nicely to problems in which one is interested in globally simulating the evolution of solids over a wide range of sizes where the detailed size distribution *at small sizes* both has a generally predictable form, and is of secondary interest. This approach uses a finite number of moments \mathcal{M}_l of the particle mass distribution, defined by

$$\mathcal{M}_l = \int_0^\infty m^l f(m, t) dm, \quad (23)$$

to track general properties of the particle population over time under the assumption that the general form of the particle mass distribution up to some fragmentation mass m_* is known. Note that, by this definition of $f(m)$, the mass volume density in a bin of width dm is $m f(m) dm$. In the moments method, the coagulation equation is reduced to a set of ordinary differential equations

$$\frac{d\mathcal{M}_l}{dt} = \int_0^\infty \int_0^\infty \left[\frac{1}{2} (m + m')^l - m^l \right] \times K(m, m') f(m, t) f(m', t) dm dm', \quad (24)$$

which leads to a closed set of equations as long as the total number of powers of m in the expression on the RHS is $\leq l$, which is true even for the realistic collisional kernel we use. In this work, we assume that the dust mass distribution is a power law $f(m) \propto m^{-q}$ with (potentially variable) exponent q . The assumption of a power law distribution for the dust population is motivated by a number of detailed models (e.g., Weidenschilling 1997, 2000; Dullemond & Dominik 2005; Brauer et al. 2008; Birnstiel et al. 2010, 2011, 2012a) that show distributions with nearly constant mass per decade up to some upper limit which grows with time until a frustration limit is reached (see Estrada & Cuzzi 2008).

Under the assumption of a powerlaw with fixed exponent q , we can derive an equation for the time rate of change of the particle mass m_L that characterizes the largest mass in the distribution, until m_L gets as large as the fragmentation mass (see next section) (Eq. (28) of Estrada & Cuzzi 2008):

$$\frac{dm_L}{dt} = (3 - q)(2 - q)\rho\Gamma_2 \left[(3 - q) \times (m_L^{2-q} - m_{\min}^{2-q}) \times m_L^{2-q} - (2 - q) (m_L^{3-q} - m_{\min}^{3-q}) m_L^{1-q} \right]^{-1}. \quad (25)$$

For $q < 2$, m_L is represented by the upper end of what we will refer to as the “dust” mass distribution. For $q = 2$, there is equal mass per decade, whereas for $q > 2$, most of the mass is in the smaller particles and the mass m_L will depend on the smallest size in the distribution. In Eq. (25), Γ_2 is an integral over the collisional kernel derived from Eqns. (23-24) for $l = 2$ (see Estrada & Cuzzi 2008):

$$\Gamma_2 = \int_{m_{\min}}^{m_L(t)} \int_{m_{\min}}^{m_L(t)} K(m, m') m^{1-q} m'^{1-q} dm dm'. \quad (26)$$

The definition of the kernel $K(m, m')$ is discussed in Sec. 2.4.2. We solve Eqns. (25) and (26) using a 4th order Runge-Kutta method.

Because we assume a fixed power law representation of the dust particle mass distribution, its mass histogram is defined by the moments at any time, the index q , and for any resolution, by its lower and upper bounds. We define a particle radius distribution logarithmically spaced from lower bound r_{\min} to upper bound r_L :

$$r_k = r_{\min} (r_L / r_{\min})^{\frac{k-1}{n_p-1}}, \quad (27)$$

where n_p defines the number of points per decade of radius. Drazkowska et al. (2013, 2014) have emphasized the importance of maintaining good mass resolution in brute-force solutions of the coagulation equation, finding that ~ 40 bins per mass decade (or ~ 120 per radius decade) are generally required. However, such a large number of bins is not required for the moments method, given our assumption of a power law distribution in the dust component. We typically use 20 – 100 bins per radius decade to calculate the relative velocities, which is more than sufficient. The particle masses can then be determined using the average dust particle material density ρ_p , which we determine from the fractional masses of solid species:

$$\rho_p = \frac{\sum_i \alpha_i^d}{\sum_i \alpha_i^d \rho_i}, \quad (28)$$

where ρ_i is the material density of species i (see Table 2). In this paper, we always assume that the initial distribution has $r_{\min} = 0.1 \mu\text{m}$, and $r_L(t=0) = 1 \mu\text{m}$ at all R . Though the density of dust particles evolves as their composition changes, and thus m_{\min} is not a true constant, the minimum *radius* r_{\min} is a constant in our evolutions. Much like modeling a variable q , we could in the future model a different or variable r_{\min} by employing the

appropriate number of moments (see Estrada & Cuzzi 2008). The logarithmic binning in r_k (and thus m_k) is used as the basis for calculations of relative velocities (Sec. 2.4.3), for characterizing the reservoir of “dust” material that migrators may sweep up (Sec. 2.4.4), and to compute the opacity (Sec. 2.3.2).

We also note that, it is fairly straightforward to implement particle porosity in the growth parts of our code (see Estrada & Cuzzi 2008). Particle porosity may be very important (see, e.g. Ormel et al. 2008; Zsom et al. 2010; Okuzumi et al. 2012) in allowing for particles to effectively grow to larger sizes while maintaining low St. Thus, their radial drift times would be longer perhaps allowing them to circumvent the radial drift barrier (see Sec. 2.4.5 and 4.1). Furthermore, the particle porosity can itself evolve with size which would also affect the opacity in addition to stopping times. Our code can handle this modification, but we leave this further layer of complexity for a later paper.

2.4.2. Particle Sticking, Bouncing and Fragmentation

The collisional kernel $K(m, m')$ can be factored into three components:

$$K(m, m') = \sigma(m, m') \Delta V_{pp}(m, m') S(m, m'), \quad (29)$$

where $\sigma(m, m') = K_0(m^{1/3} + m'^{1/3})^2$ is the collisional cross section between masses m and m' , $K_0 = \pi(3/4\pi\rho_p)^{2/3}$, and $\Delta V_{pp}(m, m')$ is their relative velocity. The kernel properties depend on the size distribution of particles, the individual particle densities, the total mass fraction of solids, and ambient nebula conditions.

We define sticking coefficients $S(m, m')$, which depend on the particle masses and relative velocities, to capture both the “bouncing barrier” and the “fragmentation barrier” as follows. The first barrier encountered by growing particles is the bouncing barrier, when $S_b(m, m') \rightarrow 0$ according to:

$$S_b(m, m') = 1 - \frac{m}{m + m'} \frac{\Delta^2 V_{pp}(m, m')}{V_b^2} \geq 0. \quad (30)$$

We adopt a bouncing prescription using the second row of Fig. 11 of Güttler et al. (2010) in which the threshold velocity for bouncing collisions between similar-sized compact silicate aggregates can be approximated as $V_b = (C_0/m')^{1/2}$, where the constant $C_0 = 10^{-7} \text{ g cm}^2 \text{ s}^{-2}$. Particle pairs that have $S_b = 0$ are considered to have sufficient energy to avoid sticking, but insufficient energy to fragment.

In a similar way we adopt a condition for the fragmentation of a target with mass m' by a projectile of mass m :

$$S_*(m, m') = 1 - \frac{m}{m + m'} \frac{\Delta^2 V_{pp}(m, m')}{Q_*} \geq 0. \quad (31)$$

Equations (30) and (31) account for bouncing and fragmentation criteria implicitly (e.g., Windmark et al. 2012a, 2013) by smoothly decreasing $S_{b,*}(m, m')$ from 1 at zero collision velocity to 0 for a particle pair colliding with a mass-dependent collision velocity.

The particle fragmentation strength is captured through the parameter Q_* , which has the dimensions of velocity squared as in Eq. (30). We follow Stewart & Leinhardt (2009) and Beitz et al. (2011) for weak silicate particles of comparable mass, colliding at low relative velocity. We include a compositional variation in Q_* , motivated by recent results that suggest that icy particles are “stickier” or stronger, and might grow larger, faster, and with higher porosities than silicate particles (Wada et al. 2009, 2013; Okuzumi et al. 2012, see also Sec. 1). We determine the local value of Q_* by a mass weighted average over the species making up the composition of a grain

$$Q_*(R) = \sum_i Q_i \alpha_i^d(R) / f_d(R), \quad (32)$$

Because we consider icy particles to be stickier, we also scale the bouncing threshold velocity by a factor of 10 (or 100 in energy) as we do for the fragmentation. Although the kernel can also include particle porosities (see Estrada & Cuzzi 2008), we do not include them explicitly for this paper. In practice this leads to $Q_* \simeq 4 \times 10^5$ outside the ice line, and $Q_* = 10^4$ inside.

The fragmentation barrier mass m_* is determined by the condition that the energy per unit mass in a collision between a target particle of mass $m' = m_*$ and some other particle $m \leq m_*$ exceeds the strength of the particle Q_* . In turbulent conditions, m_* is the mass of a particle that is destroyed upon colliding with a comparable mass particle. However, the radius of the particle that satisfies the condition in Eq. (31) may be smaller than m_* under low turbulence conditions where headwind-drag-driven velocities dominate (See next section).

Once the fragmentation barrier is reached for a target particle, our code provides a reservoir of material (with an associated *creation rate*) from which growth may proceed by sweep up of smaller grains, but which remains subject to destruction by particles of comparable or smaller sizes. These particles represent the lower end of the submigrator population. Particles that are fragmented release their mass into the background “dust” population with its current local size distribution. We treat the fragmentation of particles statistically (see Sec. 2.4.6) as well as mass transfer between them (Sec. 2.4.4). Thus we believe our model captures the essential physics of recent experimental outcomes and models regarding collisional sticking, bouncing and fragmentation (Güttler et al. 2009, 2010; Zsom et al. 2010, 2011; Weidling et al. 2012; Windmark et al. 2012a).

2.4.3. Relative Particle Velocities

We include a variety of sources for the particle relative velocities: Brownian motion, pressure gradient, vertical settling and turbulence. We briefly summarize them here, while giving a more detailed description of how we calculate them in Appendix A.4.

The thermal motion of particles, Brownian motion, is dependent upon the masses of the particles m and m' , and the ambient nebula temperature

$$\Delta V_{\text{Bro}}(m, m') = \sqrt{\frac{8k_B T}{\pi} \frac{(m + m')}{mm'}}, \quad (33)$$

and is only effective for the smaller particles near the

lower bound of our mass distribution.

The pressure-induced, or systematic dust velocities result from the gas in the nebula orbiting at slightly less than the local Kepler velocity. In a rotating frame, a parcel of gas experiences an outward directed pressure gradient force that counters the inward force of solar gravity. The dust particles do not feel this radial pressure gradient force directly, but experience an azimuthal drag force from the more slowly rotating gas, leading to size-dependent radial and azimuthal velocities. In cases where the local solids fraction is high and affects the gas velocity, particle and gas relative velocities must be determined iteratively. To ensure correct results in all regimes, we routinely solve for these components of the velocity from a set of equations generalized from Nakagawa et al. (1986) by Estrada & Cuzzi (2008) for a particle size distribution (though, also see Tanaka et al. 2005):

$$\frac{\partial U_k}{\partial t} = -A_k \rho (U_k - u) + 2\Omega V_k; \quad (34)$$

$$\frac{\partial V_k}{\partial t} = -A_k \rho (V_k - v) - \frac{1}{2}\Omega U_k, \quad (35)$$

$$\frac{\partial u}{\partial t} = -\sum_l A_l \rho_l^d (u - U_l) + 2\Omega v - \frac{1}{\rho} \frac{\partial p}{\partial R}, \quad (36)$$

$$\frac{\partial v}{\partial t} = -\sum_l A_l \rho_l^d (v - V_l) - \frac{1}{2}\Omega u, \quad (37)$$

where (U_k, V_k) are the radial and azimuthal velocity components for particles of mass m_k , (u, v) are those for the gas, $A_k = (\rho t_k^s)^{-1}$, and

$$\rho_k^d = \sqrt{\frac{2}{\pi}} \frac{\Sigma_k^d}{2h_k^d} e^{-\frac{1}{2}(z/h_k^d)^2} \quad (38)$$

is the mass volume density of mass bin k where h_k^d is the scale height of m_k (see Sec. 2.2.3).

Equations (34-37) represent a set of $2n + 2$ equations in $2n + 2$ unknowns where n is the number of particle bins in the distribution given that there are n_p particle bins per decade radius (see Sec. 2.4.1 and Appendix B). We solve this system of equations using a matrix method as defined in Appendix A.4. The pressure gradient in Eq. (36), where p is the gas pressure, can be expressed in terms of the more familiar η parameter as $-(1/\rho)\partial p/\partial R = 2\Omega\eta V_K$, where

$$\eta(R, t) = -\frac{1}{2} \left(\frac{c}{V_K} \right)^2 \frac{R^{5/2}}{\Sigma T^{1/2}} \frac{\partial}{\partial R} \left[R^{3/2} \Sigma T^{1/2} \right], \quad (39)$$

and V_K is the local Kepler velocity (Nakagawa et al. 1986; Cuzzi et al. 1993). Pressure gradients can be quite steep near the outer edge of the disk, and can lead to rapid inward migration of even very small particles. In most cases, when the local particle density is small compared to the gas density, the particle drift velocity U_k can be well approximated by (Weidenschilling 1977, Cuzzi and Weidenschilling 2006):

$$U_k = \frac{2\text{St}_k \eta V_K}{1 + \text{St}_k^2}. \quad (40)$$

For the turbulence-induced velocities, we use the closed form prescriptions for a particle size distribution of Ormel & Cuzzi (2007). The relative velocity with respect to the gas is then $V_{\text{pg}}^2 = v_t^2 - V_t^2$ (Cuzzi & Hogan 2003; Ormel & Cuzzi 2007), where the turbulent gas velocity is given by $v_t = \alpha_t^{1/2} c$ (see, e.g., Cuzzi et al. 2001), and V_t is the average inertial space particle velocity due to turbulence. The particle-to-particle turbulent relative velocities ΔV_{12} (Eq. (16) Ormel & Cuzzi 2007) are less straightforward because of the different coupling that exists between particles and eddies of different sizes. Recent numerical simulations have obtained results differing from these parametrizations by a factor of order unity depending on St (Hubbard 2012; Pan & Padoan 2013). It remains unclear how much of this difference arises from the relatively low Reynolds number of the numerical simulations, relative to the inertial range turbulent kinetic energy spectrum of the actual nebula which is assumed by Ormel and Cuzzi (2007). For more discussion, see Cuzzi & Hogan (2003).

From the various contributions, we calculate the particle-to-gas relative velocities for a particle of mass m which we use to calculate the particle stopping times;

$$\Delta V_{\text{pg}} = [(U - u)^2 + (V - v)^2 + W^2 + V_{\text{pg}}^2]^{1/2}, \quad (41)$$

where $W = -\Omega^2 z t_s$ is the particle vertical settling velocity, in which the vertical coordinate z is generally taken to be the subdisk scale height h_D (see Sec. 2.2.3). The particle-to-particle relative velocities are then given by

$$\Delta V_{\text{pp}}(m, m') = [(\Delta V_{\text{Bro}})^2 + (\Delta V_{\text{pre}})^2 + (\Delta V_{12})^2]^{1/2}, \quad (42)$$

where $(\Delta V_{\text{pre}})^2 = (U - U')^2 + (V - V')^2 + (W - W')^2$. If we are strictly in the Epstein flow regime, then the stopping times do not depend on ΔV_{pg} , so ΔV_{pp} can be calculated in a straightforward manner from the velocity components. However, if there are particles in the Stokes flow regime, then the stopping times depend on ΔV_{pg} and iterations are needed to converge to a proper solution (see Appendix A.4).

We note that in Eq. (41), we have summed the mean relative velocity between the gas and particle in quadrature with that of the fluctuating turbulent relative velocity which is not strictly correct. A similar argument can be made for the inclusion of ΔV_{pre} in Eq. (42) which we take to be the mean collision velocity. It has been argued by Garaud et al. (2013) that this construct is not accurate when the dominant velocities are systematic. However, in the models we present here, the turbulent velocities dominate the systematic ones so that we do not expect that any differences will be significant. We leave a more proper treatment for future work.

2.4.4. Migrators and Growth Beyond the Fragmentation Barrier by Mass Transfer

Once the fragmentation barrier m_* has been reached, we employ a more sophisticated, semi-analytical and statistical algorithm for the further growth of particles. In this regime, we track mass and radial drift explicitly for a population ranging from “submigrators” which are subject to mutual collisional destruction from particles of similar size or smaller, to “migrators”, which have grown large enough to have a much lower probability of destruction and may grow by mass transfer between them and particles of smaller size (Windmark et al. 2012a; Garaud et al. 2013). Disrupted submigrators and migrators are distributed back into the dust population with the same q . The migrator distribution is defined on a continuous, time-dependent mass grid where the width of each mass bin can vary due to different rates of growth for different sized particles. Thus the evolving mass histogram for $m > m_*$ does not follow a power law in general.

Beyond the fragmentation barrier, particles can still grow through incremental means, by the sweepup of smaller material. The simplest expression for incremental growth assumes perfect sticking between a particle and (smaller) feedstock particles so that, schematically,

$$\frac{dm}{dt} = \sigma \Delta V_d \rho_d, \quad (43)$$

where σ is the collision cross section and ΔV_d is some characteristic relative velocity between m and the feedstock population (see, e.g., Cuzzi et al. 1993; Brauer et al. 2008). We generalize this to a size distribution, in which sticking is not assumed to be perfect, to define the growth rate of a migrator $m_k > m_*$:

$$\frac{dm_k}{dt} = \sum_{l=1}^{n_*} \sigma_{k,l} S_{k,l} \Delta V_{k,l}^{\text{pp}} \rho_l^d + \sum_{l=n_*+1}^k \sigma_{k,l} S_{k,l} \Delta V_{k,l}^{\text{pp}} \rho_l^m, \quad (44)$$

where $S_{k,l}$ are the sticking coefficients, the index n_* refers to the fragmentation barrier mass bin, and $\Delta V_{k,l}^{\text{pp}}$ is the relative velocity between m_k and m_l . The first term on the RHS is due to the dust population, and the second term the migrator population. The volume density of migrators ρ_k^m is defined in terms of the total mass of solids in a migrator mass bin, M_k^m , and the total volume of the particle sublayer, of vertical thickness $2h_d$ near the midplane, from where migrators can accrete other material

$$\rho_k^m = \frac{M_k^m}{2\mathcal{A}h_d}, \quad (45)$$

where \mathcal{A} is the surface area of the radial bin. Equation (44) allows for a migrator m_k to accrete other particles of $m_l \leq m_k$, but the sticking will be zero for a large range of size pairs when the collision specific energy exceeds Q_* (or C_o).

On the other hand, there are outcomes of high-velocity collisions which lead to growth of the target particle, which have been observed and studied experimentally (e.g., Wurm et al. 2005; Kothe et al. 2010). Specifically, the impact velocity may be insufficient to fragment the larger target particle, but sufficient to fragment the smaller particle and allow deposition of mass on the

larger particle - if the efficiency of accretion ϵ_{ac} exceeds that of erosion ϵ_{er} . We use the model of Windmark et al. (2012a,b), in which the threshold for fragmentation is both mass and velocity dependent, to account for this process:

$$\mu(m, V_{\text{cm}}) = C_w m^{-0.068} V_{\text{cm}}^{-0.43}, \quad (46)$$

where V_{cm} is the relative velocity of the target and impactor in the center of mass frame, the coefficient $C_w = 3.27 \text{ g}^{-0.068}$ and masses and velocities are in cgs units. In order to account for the stickiness of icy particles (see Sec. 2.4.2), we scale C_w by a factor $(Q_*/10^4)^{0.21}$. The fragmentation threshold is reached when $\mu = 1$. We apply Eq. (46) to both m_l and m_k where the center of mass velocities are given by

$$V_k^{\text{cm}} = \frac{\Delta V_{\text{pp}}}{1 + m_k/m_l}; \quad V_l^{\text{cm}} = \frac{\Delta V_{\text{pp}}}{1 + m_l/m_k}. \quad (47)$$

Fragmentation with mass transfer only occurs when $\mu_k \geq 1$ and $\mu_l < 1$ (see Windmark et al. 2012a). If this condition is satisfied, we then calculate the efficiency of accretion from (Beitz et al. 2011; Windmark et al. 2012a)

$$\epsilon_{\text{ac}} = -6.8 \times 10^{-3} + 2.8 \times 10^{-4} \left(\frac{m_l}{4.1 \text{ g}} \right)^{0.16} \Delta V_{\text{pp}}, \quad (48)$$

and the efficiency of erosion (Windmark et al. 2012a)

$$\epsilon_{\text{er}} = 9.3 \times 10^{-6} \left(\frac{m_l}{m_0} \right)^{0.15} \Delta V_{\text{pp}} - 0.4, \quad (49)$$

where $m_0 = 3.5 \times 10^{-12} \text{ g}$ is a monomer mass. The erosion efficiency is an interpolation between the experimental results of several workers (Paraskov et al. 2007; Teiser & Wurm 2009; Schräpler & Wurm 2011). A successful transfer of mass to the larger particle m_k occurs then if $\Delta m_k/m_l = \epsilon_{\text{ac}} - \epsilon_{\text{er}} > 0$, which is assigned to the value of $S_{k,l}$ in Eq. (44). Inspection of Eqs. (48) and Eq. (49) demonstrates that for a given impactor mass m_l , higher relative velocities are required to initiate erosion versus accretion. As an example, for a $m_k = 1 \text{ g}$ target particle being impacted by a projectile with $m_l = 0.05 \text{ g}$ for a relative velocity of 5 m s^{-1} , the target particle accretes roughly 6% of the impactor with no net erosion. On the other hand, for the same pair impacting at 15 m s^{-1} , the target particle accretes over 20% of the impactor, but also experiences $\sim 7\%$ erosion. In our treatment, the remaining projectile mass, which by definition is fragmented, as well as the eroded mass are assumed to be returned to the dust population.

Finally, once migrators are large enough that $\Delta^2 V_{\text{pp}} \lesssim 2Q_*$, they can accrete migrators as large as themselves in pairwise mergers if they collide. A check is made to ensure that no more mass is “accreted” in a timestep than actually exists locally (for more detail, see Appendix A.5).

2.4.5. Radial Drift and Evaporation Fronts (EFs)

Due to variable coupling with the nebula gas, particles of different size will drift radially at different rates with respect to the gas. The radial drift velocity for a particle of mass m_k has two contributions (e.g., see Takeuchi & Lin 2002; Birnstiel et al. 2010):

$$V_k^{\text{rad}} = \frac{V_g}{1 + \text{St}^2} + \Delta U_k. \quad (50)$$

The first term is directly imposed by the radial motion of the gas that moves with advective velocity V_g (section 2.1). The second term ($\Delta U_k = U_k - u < 0$) is the radial drift velocity of the particle with respect to the gas (section 2.4.3). This drift increases with particle size until $t_s \sim \Omega^{-1}$ or $\text{St} = t_s \Omega \sim 1$, but then decreases for larger sizes (see Eq. [40]). In the terrestrial planet region, meter size particles drift most rapidly, but further out in the disk where gas densities are low and the pressure gradient can be very strong, much smaller particles drift inward the most rapidly (Brauer et al. 2008; Hughes & Armitage 2010).

In our code we track the radial drift across radial bin boundaries for individual migrator mass bins. We do this by calculating the inward drift time of the migrator across (logarithmically spaced) radial bins of width ΔR :

$$t_k^{\text{rad}} = -\frac{R}{V_k^{\text{rad}}} \left(1 - e^{-|\Delta R|}\right), \quad (51)$$

where the radial drift velocity for larger particles is generally a negative quantity (consistent with our sign convention, see Sec. 2.1 or 2.2.2). This allows us to calculate for every migrator mass bin k how much mass is drifting out of the local radial bin in a time $\Delta t(R)$:

$$M_k^{\text{drift}} = M_k^{\text{m}} \frac{2\Delta t(R)}{t_k^{\text{rad}}}, \quad (52)$$

where the factor of 2 assumes that the drift time from the bin's midpoint is representative. Equation (52) is the maximum amount of mass that can drift out of a radial bin in time Δt , and does not take into account the fragmentation of some particles (see Sec. 2.4.6).

It is possible that some migrators with $m \sim m_*$ have positive outward drift if, for example, α_t is sufficiently large (which leads to more vigorous collisions and smaller m_*) that the gas advection term (first term on the RHS of Eq. [50]) can overwhelm the radial component of the headwind-driven drift velocity. Under such circumstances, the redistribution of these migrators is done using the radial diffusion-advection equation (Sec. 2.2.2).

Self-consistently modeling a globally evolving nebula requires that we consider the presence of Evaporation Fronts (EFs) which are regions in the disk where phase changes between solids and vapor can occur. The evaporation of radially drifting material, and subsequent recondensation of outwardly diffusing vapor, can have three main effects. First, it can increase the abundance of vapor inside an EF, with implications for chemistry and mineralogy. Second, it can increase the fractional abundance of solid material available *just outside* the EF, perhaps by a factor of ~ 10 or more (e.g., Cuzzi & Zahnle 2004; Ciesla & Cuzzi 2006; Garaud 2007), with implications for accretion. Third, it can significantly change the composition of solid material outside the EF from

“cosmic abundance” values. We will illustrate all these effects in this paper; a more detailed study will await future publications.

Rather than treating an EF as a sharp boundary, we allow for evaporation (or condensation) to occur over a small range of radii covering a midplane temperature range $2\Delta T_{\text{EF}} \sim 0.1 - 1$ K relative to the nominal species evaporation temperature T_i (see Table 2). The fractional solid abundance $\alpha_i^{\text{v,d}}$ of a species i (with density ρ_i) at some radial location R and at some local temperature T , is transformed into vapor linearly as the calculated midplane temperature changes over the temperature range $T_i - \Delta T_{\text{EF}} \leq T \leq T_i + \Delta T_{\text{EF}}$ (Sec. 2.3.1). This gradual radial transition in solids abundance, which can span a significant radial range, mimics the anticipated effect (as described below) of “buffered” temperature changes across an EF as material is evaporated or condensed, rather than allowing unrealistic (and numerically problematic) abrupt radial changes in opacity and temperature just inside an EF. This simple numerical treatment captures the essence of the actual condensation process in which material first evaporates at the midplane, and then at increasingly higher altitudes with decreasing distance from the star as the disk gets warmer (Davis 2005; Min et al. 2011). The effect is seen in the constant midplane temperature regions in our simulations (e.g., see Fig. 1).

In our code, dust grains are effectively treated as aggregates of chemically distinct monomers (although see Sec. 2.4.1) whose fraction of species i can be quickly removed or emplaced. Larger particles that are followed explicitly (Sec. 2.4.4) are assumed to lose that fraction of their material that is of evaporating or condensing species i as they migrate through the EF for species i , and their masses and mean densities are adjusted accordingly. Their evaporated material is then added to the local vapor inventory. Better models of the largest particles whose interiors are somewhat insulated from ambient nebular conditions, and could potentially transport very volatile species from very cold to warmer regions (e.g., see Estrada et al. 2009), will require physical evaporation rates and internal structure models. We do not treat the kinetics of evaporation and condensation here (see discussions in Cuzzi et al. 2003; Ciesla & Cuzzi 2006). We plan to include these effects in future work.

2.4.6. Probability of Destruction and “Lucky Particles”

In our treatment of growth, the particle mass such that the sticking coefficient first approaches zero for equal mass particles represents the “bouncing” barrier. That is, such a collision is energetic enough to prevent any sort of sticking, but not energetic enough to fragment the particle (e.g., Güttler et al. 2010; Zsom et al. 2010). Our nominal fragmentation mass m_* (section 2.4.2) is also a convenient reference value, at which particles of equal mass fragment each other under local nebula conditions. In practice, we employ a statistical scheme for the probability of destruction of a migrator. The scheme utilizes a Gaussian PDF of relative velocities for a given impactor mass, with rms velocity equal to the mean (Carballido et al. 2010; Hubbard 2012; Pan & Padoan

2013).

The collision rate of target migrators of mass m' with projectile particles of masses $m \leq m'$ is given by (*cf.* Eq. [29])

$$\mathcal{R}_{\text{coll}}(m', m) = \pi(r' + r)^2 b(m) \Delta V_{\text{pp}}(m', m), \quad (53)$$

where $b(m) = \rho_{\text{d},m}/m$ is the number density of particles of mass m , and the subscripts refer to either the volume density of dust or migrators. The probability that a migrator of mass m' will suffer fragmentation as it grows during time Δt can then be obtained from

$$\mathcal{P}(m') = \int_t^{t+\Delta t} dt' \int_{m_0}^{m'} \pi(r' + r)^2 \Delta V_{\text{pp}}(m', m) \times \zeta(m', m) f(m, t') dm \quad (54)$$

where $\zeta(m', m)$ is an integral over a Gaussian distribution of relative velocities covering a range equal to or greater than the critical impact velocity $V_c = \sqrt{2Q_*(m + m')/m}$:

$$\begin{aligned} \zeta(m', m) &= \frac{1}{\sqrt{2\pi} \Delta V_{\text{pp}}(m', m)} \int_{V_c(m)}^{\infty} e^{-\frac{(V' - \Delta V_{\text{pp}})^2}{2\Delta V_{\text{pp}}^2}} dV' \\ &= \frac{1}{2} \left[1 - \text{erf} \left(\frac{V_c - \Delta V_{\text{pp}}}{\sqrt{2}\Delta V_{\text{pp}}} \right) \right] \end{aligned} \quad (55)$$

We discretize Eq. (54) for use in our calculations as described in Appendix A.6. Although other workers have utilized a Gaussian scheme as we do here, others have argued that the distribution should be Maxwellian (e.g., Galvagni et al. 2011; Windmark et al. 2012b). Garaud et al. (2013) have developed a more detailed model in which she shows that the mean and rms square velocities are not the same. Furthermore, our approach to calculating ζ is more akin to that of Windmark et al. (2012b), whereas Garaud et al. (2013) argues that the relative velocity (in our notation V') should be included in the integral over the PDF in order to recognize that collisions of particles with larger collision velocities have a higher collisional frequency than those with lower collision velocities. We intend to examine the more detailed model of Garaud et al. in future work.

Using our formalism, we calculate the fraction of migrators within every migrator mass bin that is destroyed during every growth step. The amount of mass returned to the dust distribution for any mass m' is then $M_{\text{dest}} = \mathcal{P}(m') M_m(m')$ where $M_m(m')$ is the total mass in migrators with mass m' . This mass is subtracted from the total mass contained within the m' mass bin prior to determining how much mass drifts out of a radial bin (and thus a factor $1 - \mathcal{P}$ is included in Eq. [52]).

We find quite generally that growth stalls at masses slightly-to-moderately larger than the fragmentation barrier mass m_* and radius r_* . We will represent this particle radius where growth stalls to be r_M which also is the particle containing the bulk of the total mass of migrators in a radial bin. This result of stalled growth is

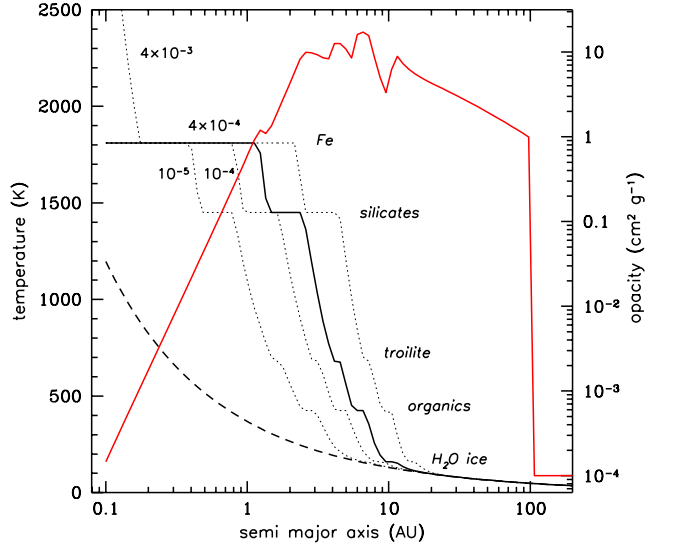


Figure 1. Initial profiles of the Rosseland mean opacity (red curve), and temperatures at the midplane (solid black curve) and photosphere (dashed curve) for our fiducial model with $\alpha_t = 4 \times 10^{-4}$. Additional midplane temperature curves are shown (dotted curves) for different values of α_t . The nearly flat regions in the temperature profiles correspond to the location of EFs as labeled.

fairly robust unless the nebula turbulence is very small, in which case incremental growth can proceed to large sizes because the particle layer becomes very dense near the midplane, and collision velocities are low.

As was seen by Windmark et al. (2012a,b) and Garaud et al. (2013), we also find that a small fraction of migrators are able to grow to larger sizes because they have grown large enough to have a low probability of destruction. We refer to these migrators as “lucky particles”, and characterize the *largest* particle in each radial bin by radius r_L . However, previous studies (except for Drazkowska et al 2013, who imposed a “pressure bump” to prevent loss by drift) have not allowed for the significant radial drift of such particles, which greatly reduces their abundance. While rare, such particles can transport material over large radial distances. Treating the growth of these “lucky” migrating particles simultaneously with their radial drift and nebula evolution is a significant advantage of our code over previous global models.

3. RESULTS

3.1. Baseline model

We choose as our fiducial model a nebula with a stellar mass of $M_* = 1 M_\odot$, an initial disk mass of $0.2 M_\odot$ and a scaling factor $R_0 = 10$ AU (see Sec. 2.1). The radial grid in our evolutions spans a range from $0.5 - 1000$ AU using 96 logarithmically spaced bins, chosen to make optimal use of the Haswell CPUs (12-core, 24 processors) at the NAS Pleiades cluster used in our simulations. In our code, radial bin width is only a concern for radial drift of migrator particles, because other properties that communicate across the grid such as gas and dust evolution

are fully implicit². All simulations in this paper span up to 2×10^5 years, and use variable stellar luminosity L and particle strength Q_* (except in sections 3.5 and 3.6 where these parameters are kept constant).

We employ a constant turbulent viscosity parameter $\alpha_t = 4 \times 10^{-4}$ as our baseline, though we explore a model that uses a constant $\alpha_t = 4 \times 10^{-3}$. As noted in Section 1, recent studies of purely hydrodynamical instabilities suggest that $\alpha_t > 10^{-4}$ (Nelson et al 2013, Marcus et al 2013, 2015; Stoll and Kley 2014). We do not model disks with lower values of α_t . Such models have been explored in detail (e.g., Weidenschilling 1997, 2000, 2004, 2011); vanishingly small α_t leads to rapid *in situ* growth by sticking and/or collective instabilities rather than the delayed growth, and extensive redistribution of solids, which is the primary focus for this paper and arguably in better agreement with observations (Sec. 1).

In the following sections, we consider models with fragmentation (F) only, then bouncing and fragmentation (BF) and finally add mass transfer (MTBF) as described in Sections 2.4.2 and 2.4.4. In forthcoming papers, we will explore radially and vertically variable α_t profiles (e.g., Bai & Stone 2011; Kalyaan & Desch 2015), which introduce another layer of complexity.

In this work, we choose to cut off the *initial* distribution of solids at 100 AU (where the initial gas surface density Σ quickly drops off to $\ll 1 \text{ g cm}^{-2}$). Other workers have chosen similar cutoffs (e.g., Brauer et al. 2008; Birnstiel et al. 2010); while arbitrary, this initial condition simply provides a convenient reference point from which to follow the solids evolution. The motivation is that the strong pressure gradients at the outer edge of the nebula will lead to rapid inward migration of even the smallest grains unless one assumes sufficiently high values of α_t which leads to outward transport of solids as the gas disk spreads in spite of the presence of a strong pressure gradient (e.g., see Sec. 3.7).

In **Figure 1** we show the initial midplane temperature and opacity profile for our fiducial model (solid curves). The corresponding photosphere temperature is shown by the dashed curve. The initial disk temperature is sufficiently hot at the midplane for our high α_t model (Sec. 3.7) that all of the EFs for the species used in this paper (see Table 2) are present. Although midplane temperatures in EF regions appear flat, there is a small gradient in temperature (Sec. 2.4.5) over which evaporation of volatiles is assumed to take place. It is over these transition radial ranges that the opacity decreases linearly. For comparison, we plot the temperature profiles for different values of α_t (dotted lines) to show the sensitivity to the choice of this parameter. Even for a value of $\alpha_t = 10^{-5}$, the disk is relatively hot in the inner regions because the initial stellar luminosity is $\sim 12 L_\odot$ (D’Antona & Mazzitelli 1994). In this work we adopt a constant value of $10^{-4} \text{ cm}^2 \text{ g}^{-1}$ for the gaseous opacity. In the hot, innermost regions this may be an underestimate because gaseous opacity is a function of temperature (e.g., Ferguson et al. 2005). However, for our models, dust is usually present at all locations in the disk

² A minimum requirement we impose is that the timestep used in our simulations is much smaller than the drift time of the fastest migrating particle across a radial bin. For all of our simulations presented here, this is easily satisfied.

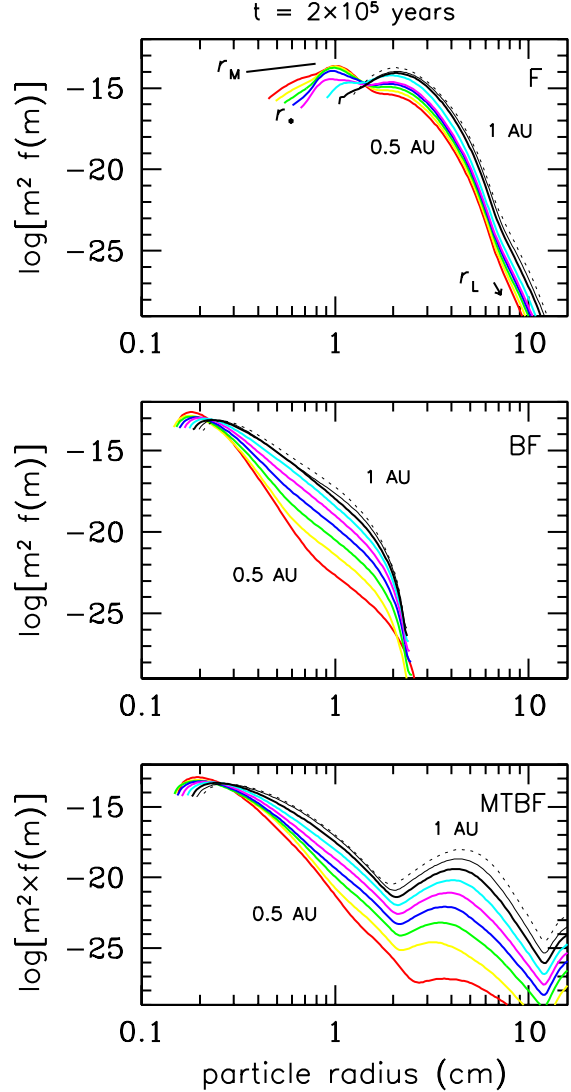


Figure 2. This figure shows several of the *actual* histograms of particle size distributions, as mass volume density per bin of width dm , for three different cases and several distances from the star. The lower boundary of these plots aligns with the upper boundary of the “dust” power law distribution at r_* , that extends downward to $0.1 \mu\text{m}$ radius. The method of determining these distributions is described in section 3.1.1. As is specifically indicated in the upper panel, the peak in this distribution represents the radius r_M which characterizes most of the net mass. The *largest single particle* in each distribution, at the far right end, provides our value of r_L . It is clear that the mass contained in these “lucky” particles is extremely small. In the lower panel one sees secondary peaks in $m^2 f(m)$ (g cm^{-3}), which are likely due to mass transfer as suggested by Windmark et al. (2012a) and Garaud et al. (2013). Though we might regard these as “breakthrough” particles, they are actually not *that* much larger than r_M , and *still* contain much less mass than particles of size r_M . This figure should be kept in mind for interpreting the remaining figures where only r_M and r_L are shown.

so that the Rosseland mean opacity is dominated by this component. In future work, we will incorporate a gaseous opacity table into our models.

3.1.1. Typical particle size distributions

Before discussing the different cases in detail, we show some typical particle size distributions in **Figure 2**.

Three of our cases (discussed below) are shown in the three panels. The curves in each panel are actual calculated distributions of particle mass volume density as a function of particle radius for particles with $r > r_*$, calculated with 100 bins per decade radius; recall that particles with $r < r_*$ are modeled by a “dust” distribution which is a powerlaw extending downward and to the left of the values shown. Each family of curves is for several different subsolar distances between 0.5 – 1 AU. Values of the fragmentation radius r_* , the mass-containing radius r_M (shown for the red curve only), and the largest “lucky” particle radius r_L are indicated in the top panel. The downward arrow indicates that the largest particle is actually below the range plotted which covers seventeen orders of magnitude in mass volume density. In future plots we will only show these three characteristic values, but the distributions of Fig. 2 underlie them all. In the lower panel, secondary peaks are seen which are most likely due to mass transfer as will be discussed later.

3.2. Fiducial model with fragmentation (“F”)

In our model, the fragmentation size is defined by that particle mass $m' = m_*$ that gives $S_* = 0$ in Eq. (31). The value of m_* will depend on ambient nebular conditions, as well as the particle strength Q_* , which is composition dependent (Eq. [32]) for the bulk of the simulations we present here.

Figures 3 and 4 show the results of a fragmentation-only model “F” in our nominal, moderately turbulent disk. The temperature (black curves) and Rosseland mean opacity (red curves) are plotted in the top panel of Fig. 3 at evolution times of 10^4 , 10^5 and 2×10^5 years. Early on, the disk remains relatively hot in the inner regions as seen by the persistence of the silicate EF at 1 AU even after 10^5 years, but the temperature quickly drops to much lower values by 2×10^5 years. This cooling is a direct consequence of the lower opacity associated with rapid particle growth when only limited by fragmentation. Evaporation fronts can clearly be seen to evolve over time, with the organics and water ice EFs at 425 K and 160 K, respectively, being the most prominent at later times (solid curve).

Fractional masses of different components are shown in the lower panel of Fig. 3. Here, the red curves refer to the dust, magenta to the migrator and green to the vapor fractions, respectively. Peaks appear in the fractional masses of the dust and migrator populations outside of EFs, because migrating particles passing through them release their volatiles into the vapor component, and some of this vapor subsequently diffuses outward across the EF to recondense onto grain surfaces. This effect has been seen in previous simulations (Cuzzi & Zahnle 2004; Ciesla & Cuzzi 2006; Garaud 2007). Relatively strong peaks in the fractional masses of solids at 10^5 years can be associated with the organics and water ice EFs, whereas at 2×10^5 years these peaks have migrated inwards considerably as the disk cools. A less prominent silicate peak is also seen at 10^5 years, that has all but vanished at later times, but this is because the silicate EF is no longer on our computational grid, and the inner boundary cannot relay information about what is occurring inside itself. The organics enhancement³ is then largest at around 1.5

AU, while the water ice peak lies near 5 AU. The solid phase mass enhancements map well with the the opacity shown in the top panel. That is, the highest opacities in the inner disk at all times are associated with the peaks in solids. A steady transport of material from the outer regions to the inner regions maintains a significant population of smaller particles, which keeps the opacity high even as particles grow, and maintains a high temperature. This can be seen by noting that at 10^4 years, there is still a lot of material in the outer disk out to 100 AU (large opacities and fractional masses there). By 10^5 years, for these specific models, the bulk of the material in the outer nebula has effectively been transported into the inner nebula, though some material still remains in the outer disk (at fractional masses of $\lesssim 10^{-6} - 10^{-5}$). We see overall enhancements in the inner regions of a factor of $\sim 2 - 3$, though it is mostly present in the vapor component (green curves). The inner nebula situation changes significantly by 2×10^5 years where much of the material at $R \lesssim 1$ AU has drifted inwards leaving much lower fractional masses of solid material, and thus much lower opacity leading to cooler overall temperatures.

The relatively rapid transport of solids to the inner regions occurs because a fragmentation-only model allows larger particle sizes to be reached relatively quickly in the outer nebula, and in relatively large numbers. In the middle panel of Fig. 3 we plot particle sizes of interest (black curves), particle Stokes numbers for r_M and r_L (blue curves) and the mean particle density of the dust (red) and migrators (magenta) at 2×10^5 years. The first thing to notice is that the fragmentation barrier size r_* has been reached almost everywhere in the disk. This is indicated by the presence of a heavy dashed curve at all distances (actually the situation was reached at around 5×10^4 years). Migrator particles also form early on, which accelerates inward solids transport. Once the fragmentation barrier has been reached, further incremental growth is hampered by the gradual destruction of particles $r > r_*$ with time, and the size of particle that carries most of the mass in the migrator size distribution (r_M) does not stray far from the fragmentation size. The characteristic “hump” outside of 3 – 4 AU corresponds to the transition between weaker and less sticky silicate particles inside the water ice EF, with the stronger and stickier icy particles (with larger Q_*) outside the EF. Indeed for this case, outside the ice EF, most of the mass has reached $r_M \sim$ meter size. Although incremental growth by sweepup of particles too small to fragment large targets leads to “lucky” particles approaching $r_L \sim$ meter size even for some distance inside the ice EF, these particles are very few in number and contain a negligibly small portion of the mass (see Fig. 2). This distribution of sizes essentially stays the same between 5×10^4 and 2×10^5 years, although there is some variation in transi-

moderately refractory, carbon-rich materials seen in comet Halley and primitive carbonaceous chondrites, which volatilize at roughly 400K (Grady & Wright 2003; Pollack et al. 1994). In what is probably an oversimplification, we further assume that these materials behave like normal volatiles, able to reversibly evaporate and recondense. In reality, their “evaporation” might be closer to an irreversible decomposition into simpler molecules such as CO and/or CH₄. This refinement is deferred to future work, but there will be implications for opacity, solids mass enhancement and nebula chemistry.

³ For this introductory work we assume that “organics” are the

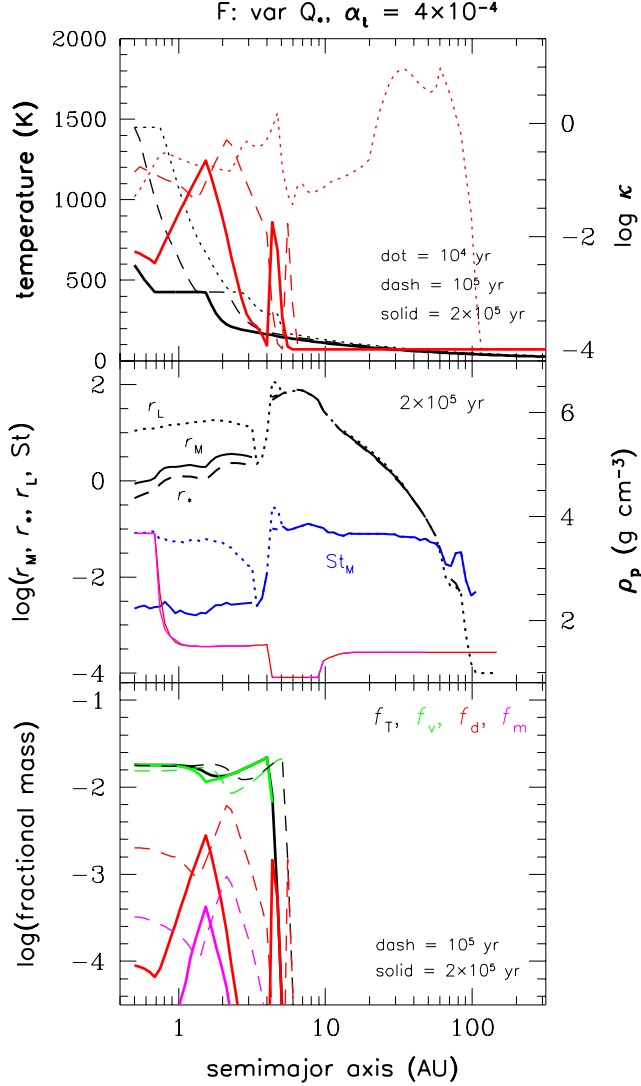


Figure 3. Fiducial model with fragmentation only (F). upper panel: Temperature (black) and opacity (red) plotted at three different times. middle panel: Fragmentation radius r_* (dashed), particle radius that carries most of the mass r_M (solid black) and largest particle radius r_L (solid black curve). The Stokes numbers for r_M and r_L are shown in blue. Also plotted are the mean particle densities for dust (red) and migrators (magenta). lower panel: Fractional masses shown at two different times. The F model is characterized by rapid growth and drift, leading to depletion of the outer disk and only modest enhancements in the inner nebula. However, the largest particle sizes can be > 1 m. See text for details.

tion boundaries due to the radial motion of the EFs.

The particle Stokes numbers (blue curves in the middle panel of Fig. 3) help to demonstrate why there is systematic mass transfer from the outer nebula to the inner nebula. The solid Stokes number curve refers to r_M and the dotted Stokes curve refers to the largest particle in the size distribution which include the “lucky” particles $r_L > r_M$. They diverge inside the ice line, where only rare lucky particles have such large values of St and r_L . Even while, near the ice EF, particles of about 1 m radius can be found, the high gas densities mean that $St < 1$ everywhere except at the outermost edge of the solids disk

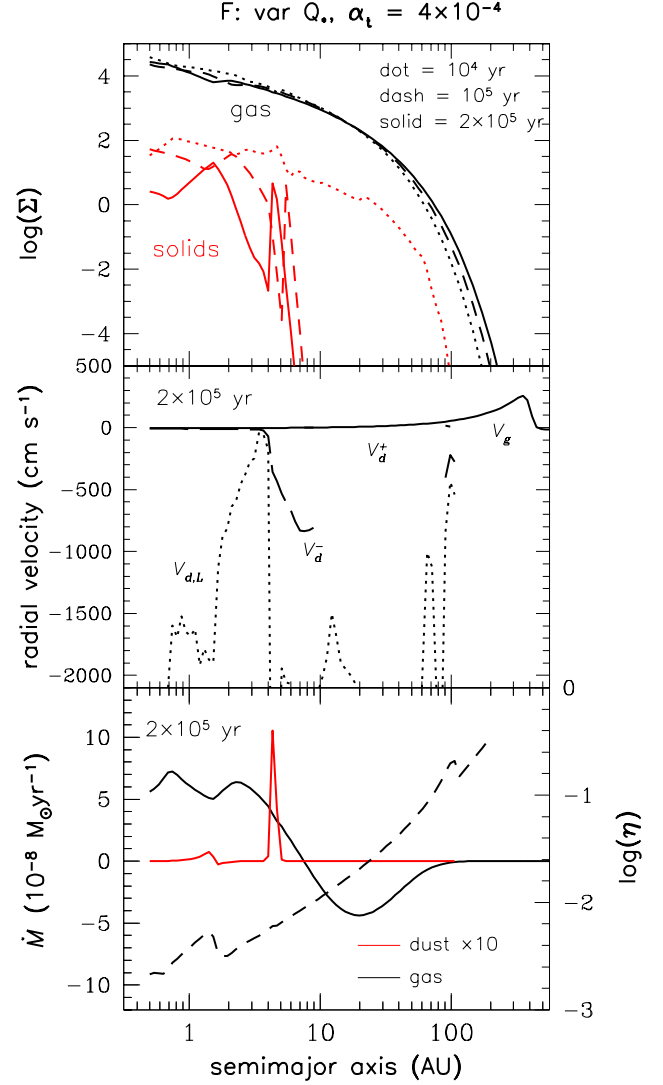


Figure 4. Fiducial model with fragmentation only (F). upper panel: Gas (black) and dust (red) surface densities at three different times. middle panel: Radial velocities of the gas (solid), largest particle (dotted), and mean inward (long dashed) and outward (short dashed) components of the dust population at 2×10^5 years. lower panel: Mass accretion rates for the gas (solid black) and the dust component (red curve). The vertical scale for the dust component is enhanced by a factor of ten for clarity. The dashed curve denotes the pressure gradient. For the fiducial choice of α_t , the evolution of the gas is modest, but substantial changes in the solids arise due to rapid growth and inward migration. See text for details.

(~ 200 AU) where the gas density is very small. Recall from Eq. (40) that for $St < 1$, the radial drift velocity is proportional to St . Inside the ice EF, St_M drops by almost two orders of magnitude because of the smaller Q_* , causing the bulk of particles to drift inward more slowly than outside the ice EF. This explains why there is a pileup of solid material inside the ice EF. The fact that r_L gradually decreases from just outside the water ice EF to the inner nebula is due to the fact that even the lucky particles are not growing fast enough to overcome the radial drift barrier. This is discussed in more detail in Sec. 4 (see Fig. 18). The maximum drift rate for par-

ticles is at $St = 1$ (Eq. [40]), but particles with $St \lesssim 1$ are still drifting faster as they grow larger, so these particles are suffering a gradual but steady loss inwards. Because the radial drift barrier cannot be overcome means that eventually most all material will be lost at later times.

Interestingly, the maximum Stokes number St_L is roughly *constant* outside the water ice EF, at around a value of ~ 0.1 . A simple relationship explains this behavior in the fragmentation-dominated regime (Weidenschilling 1988; Cuzzi & Weidenschilling 2006; Birnstiel et al. 2009, 2011). One merely sets the collision speed ΔV_{pp} equal to the fragmentation speed $u_f \sim \sqrt{2Q_*}$. Since $\Delta V_{pp}^2 \sim 2St\alpha_t c^2$ for identical particles (Ormel & Cuzzi 2007, note Birnstiel et al. drop the numerical factor), the largest particle in fragmentation equilibrium has Stokes number

$$St_* = \frac{u_f^2}{2\alpha_t c^2} = \frac{Q_*}{\alpha_t c^2}, \quad (56)$$

and c is nearly constant across the outer disk at least. Even in the inner disk where c varies somewhat more significantly, St is nearly constant, but at a smaller value commensurate with the lower Q_* for silicates.

In the Epstein flow regime, which applies to most of the particles shown in Fig. 3, the Stokes number can be written as (e.g., Birnstiel et al. 2011)

$$St = \frac{2r\rho_p}{\Sigma}. \quad (57)$$

For a roughly constant Stokes number as a function of semimajor axis, $r \propto \Sigma$ implying that the decrease in r_* and r_M in the outer regions simply mirrors the decrease in gas surface density. However, the behavior in the *inner* nebula is not reliably predicted from these formulae because the particle sizes are not strictly in the Epstein regime, but often in the transitional or full Stokes flow regime (which is generally ignored in other models). Though we cannot easily find simple expressions for expressing St in terms of the transitional formula we use, we can still give estimates for St when $r \gtrsim \lambda_{mf}$ (see Appendix A.4):

$$St = \frac{16}{3} \frac{\rho_p}{\Sigma} \frac{rc}{C_d \Delta V_{pg}} \simeq \begin{cases} \frac{2}{9} \frac{\rho_p r^2 V_K}{R \mu_m} & Re_p < 1; \\ \frac{1}{4} \frac{\rho_p^{5/6} r^{4/3}}{(\alpha_t^{1/2} \Sigma)^{1/3}} \left(\frac{V_K}{R \mu_m} \right)^{1/2} & Re_p < 800, \end{cases} \quad (58)$$

where in the case $Re_p > 1$ the particle-to-gas relative velocities ΔV_{pg} are assumed to be due to turbulence. In this work, the largest particles we grow have near unity particle Reynolds numbers. In general, for relatively smaller particles, the assumption of turbulent driven relative velocities is probably adequate unless α_t is very small. However, as particles grow larger or in the outer nebula, their relative velocities may be driven by headwind effects and closer to $\sim \eta V_K$. Later in Sec. 4 we will compare these estimates to our simulations directly.

Also in the middle panel of Fig. 3, the particle internal densities are plotted for both the migrator and dust particles as a function of semimajor axis. The “cosmic

abundance” particle density of $\sim 1.5 \text{ g cm}^{-3}$ is maintained in the outermost nebula, but significant changes in mean particle density have occurred in regions where EFs are or were found. The smoothness of the particle density profiles reflects the process of sublimation from drifting particles at EFs, followed by outward diffusion, recondensation, and advection. The most striking example of this process is evident in the region between 5 – 9 AU where the density of local solid material has essentially dropped to the density of water ice. The radial extent of this water-ice enhanced region is partly a result of outward diffusion of vapor and advection of icy grains, but (in this case) also of the inward evolution over time of the water ice EF to its current location at ~ 4 AU. The magnitude of this enhancement may be slightly overestimated *if* some amount of the drifting water ice were not evaporated inside the EF, but somehow buried and trapped in migrators to be carried further inwards. Finally, we note that slight differences in the density of migrators versus the “dust” population outside of EFs are due to the fact that we assume that condensation of vapor follows the surface area of particles (dominated by the smaller particles).

For the same case “F”, **Figure 4** shows the evolution of gas (black curves) and solids (red curves) surface density at three different times (top panel), and (at 2×10^5 years) the radial velocities of solids and gas (middle panel) and the gas and solids accretion rates (lower panel). The gas radial velocities (middle panel, solid curve) are relatively low due to the choice of α_t , and change from inward ($V_g < 0$) to outward flow ($V_g > 0$) at around 7 AU (see below). Also in the middle panel we plot the radial velocities of the largest particle $V_{d,L}$ (dotted curve, corresponding to the dotted curve in the middle panel of Fig. 3) which shows how quickly in most places these particles are drifting inwards. Variations in $V_{d,L}$ are due to differences in the size (and mass) of particles as well as transitions through EFs (Sec. 2.4.5). We also plot the radial velocities of the inward (V_d^- , long dash) and outward (V_d^+ , short dash) drifting components of the dust population (Sec. 2.2.2). The (small) outward flow of the smallest grains (due to advection and diffusion) explains why there are solids further out than the initial 100 AU solids cutoff. The inward drift is strong in the outer disk and explains how the outer disk has been cleared of most of its material. We note that V_d^- decreases sharply in the inner disk and eventually becomes similar to V_g . This decrease can be associated with the drop in St inside the water ice EF, and leads to the subsequent pileup of solid material in the inner nebula.

Reversal of the radial mass flow driven by viscosity occurs around 7 AU, with outward flows beyond this value, but in spite of this, by 2×10^5 years the bulk of the outer nebula solids have collapsed to within this radius. This can be seen in the surface density plot (top panel) where although the gas surface density has not evolved considerably due to the low α_t , the changes in the solids over time are pronounced (it is even more apparent in the lower panel of Fig. 3). At 10^4 years there is still a considerable amount of solid material out to 100 AU, but by 2×10^5 years, peaks in Σ_d outside the organics and water ice EFs are well defined, supplied by inwardly drifting material. Inside 7 AU, the advection of material

is inward, and although some vapor may diffuse outward to recondense, this appears to remain well enough inside the radius of mass flow reversal so that there is no longer an effective outward transport mechanism and material will remain confined to the inner nebula.

Other effects are more subtle. In the lower panel of Fig. 4, sharp decreases in radial drift and an ensuing pileup of solids at the water ice EF are associated with a spike in the total accretion rate of solids \dot{M}_d (red curve). Just inside the water ice peak one finds that there is a bump in the gas accretion rate that corresponds to a local minimum in the pressure gradient (dashed curve). The radial drift of the lucky particles drops at 1.5 AU; this is associated with a local decrease in r_L , related to a peak in the total migrator mass and the locally increased erosion that results.

3.3. Fragmentation and bouncing (“BF”)

When the so-called “bouncing barrier” is included in our fiducial model, the situation changes considerably. Because the particles are growing more slowly and remain smaller (see below) the opacity is larger and the temperature in the inner nebula remains high even after 2×10^5 years (see **Figure 5**, top panel), remaining more or less unchanged from its value at 10^5 years. Also, the water ice EF is found further out, at around 7 AU. The opacities are still decreasing with time in the outer nebula and increasing in the inner nebula, but remain generally larger than in the pure fragmentation case F. The fractional masses (lower panel, Fig. 5) again show enhancement peaks in the solids near the organic and water ice EFs corresponding to local peaks in the opacity, but not so much the silicate EF. Between 10^5 and 2×10^5 years, the EFs evolve only slightly in this case, so unlike the fragmentation-only case F, the enhancements *in the solids* are higher outside EFs - in fact, exceeding the enhancements of the vapor for the organics EF. The *total* enhancement of condensibles, in both solid and vapor form - in the inner regions is as high as $\sim 5 - 6$ (black curve) by 2×10^5 years. The overall fractional mass of migrators is similar ($\sim 10^{-3}$) to the fragmentation case, but they are now present everywhere in the innermost regions. A sharp cutoff in the migrator population around 5 AU is because particle sizes have not yet reached the fragmentation barrier outside this location. Interestingly, though no peak in the dust outside the silicates EF is quite discernable, the migrators do show a noticeable enhancement.

Particle sizes plotted in the middle panel of Fig. 5 demonstrate that in most of the disk, the largest particle has not reached the fragmentation size ($r_L < r_*$) - so the heavy dashed curve for r_* does not appear. The bouncing barrier has slowed the growth rate considerably because sticking becomes zero for equal mass particles at much smaller sizes than in the fragmentation-only case. In general, the bouncing barrier (BB) restricts eligible collision partners for growth to a narrower range of smaller projectile sizes - causing *all* particles to grow more slowly. Still, as long as a population of small particles remains, the BB is not impermeable and we expect that the fragmentation barrier will be reached at later times.

After 2×10^5 years, only particles inside the water ice EF have reached r_* (heavy dashed curve appears) which

is understandable since the larger Q_* outside this EF means it will take much longer to reach the larger fragmentation limit r_* (*cf.* Fig. 11, Sec. 3.5). It is apparent that r_* , r_M , and r_L in the inner nebula are smaller in this case than in case F. This seems counterintuitive since the strength remains the same; however, regarding r_M and r_L , the reason is that the number density of dust particles is much higher and the probability of destruction for particles of size r_M and r_L is proportional to the number densities of the smaller particles they are colliding with (see Eq. [53]). St_M is lower than St_* which we argue is due to a slow growth or drift related effect which we discuss in Sec. 4.1.

The smaller and inwardly decreasing value of r_* is explained in a different way. The Stokes numbers (blue curves) are smaller by an order of magnitude than in case F. A smaller St_* is explained by the higher opacity, temperature, and stronger radial temperature gradient than the lower and constant temperature in case F at 2×10^5 years (see Eq. [56], also see discussion, Sec. 4), and this leads to a smaller r_* . The bulk of particles in the inner nebula have $St_M \lesssim 10^{-3}$ causing them to drift at a much slower rate, and to be retained for longer periods before being lost with an ensuing increase in mass enhancement. Outside the water ice EF, we see a similar trend in St_M as in case F, but at smaller values because the fragmentation size has not been reached.

Finally, the internal density of dust and migrator particles (red and magenta curves, middle panel) retains interesting variability. In general, the internal density profiles are characterized by decreases just outside the various EFs; this is due to enhancement in the evaporating species as it diffuses back across the EF and condenses on to dust and migrator particles. The radial range over which the density decreases is due not only to vapor condensation but to the diffusion and advection of smaller dust grains. The interplay is quite complex though, as we will see below from gas and dust accretion rates. In particular, the density variation outside the water ice EF for case BF does not span the same radial extent as in case F, because the EF has been relatively stationary over the simulation time in case BF. However, its edges are less sharp because of the more significant outward advection and diffusion of smaller icy grains.

The radial velocities of the various particle sizes plotted in **Figure 6** (middle panel) are lower than for case F, reflecting slower radial migration of smaller particles. The location where V_d^- becomes similar to the gas radial velocity is slightly further outward due to the smaller particle size, and in fact occurs just outside the organics EF. The inward drift of lucky particles reaches a minimum speed at this point, and increases inwards up to the silicate EF which is at the inner edge of the computational grid. The more complex behavior seen in the dust and gas accretion rates compared to case F again emphasizes that there is inward advection of material in the inner regions, although at speeds less than the gas velocity, but also outward diffusion at EFs further affecting the accretion rate. The gas accretion rate shows variation through the organics and water ice EFs, because particles containing most of the mass are small and traveling with the gas. The mass accretion rates of both the gas and dust become more similar at these points implying that the dust is apparently influencing the gas

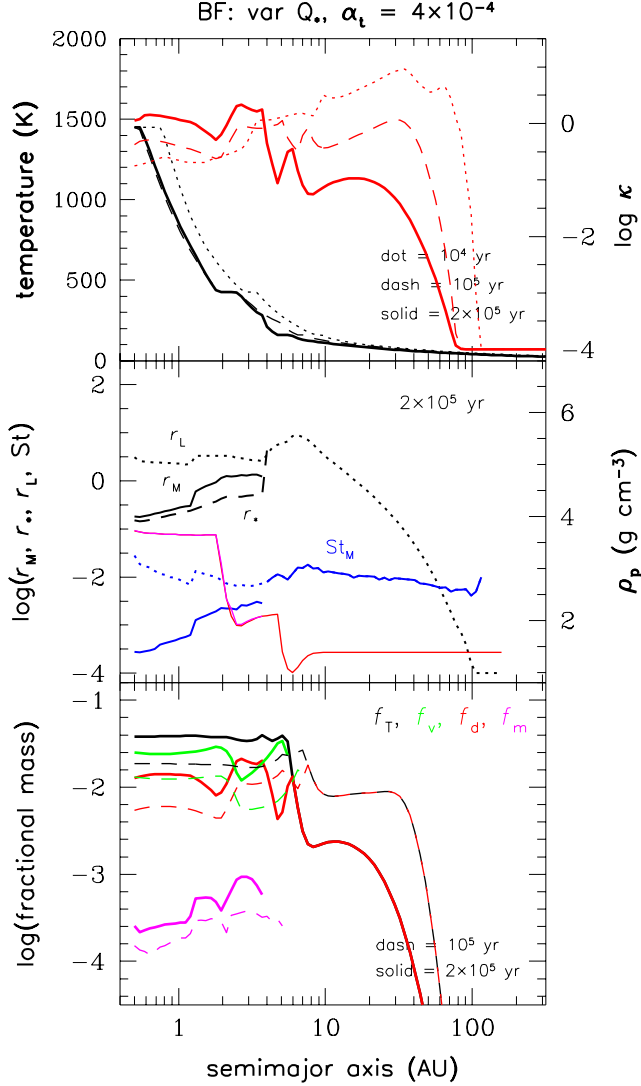


Figure 5. Fiducial model with bouncing and fragmentation (BF). Panel descriptions same as Fig. 3. When the bouncing barrier is included in our simulations, particles grow more slowly and remain relatively small over the period of the simulation ($r \geq r_*$ inside ~ 5 AU only). Lucky particles are also smaller compared to the F case. As a result the temperature remains hot in the inner nebula, and opacities are generally larger there as well. Particle growth in the outer disk is still sufficient to lead to significant inward transport, though much less than the F case. Smaller particles also lead to relatively large enhancements in dust and vapor in the inner nebula. See text for details.

evolution even though the solids-to-gas-ratio is not near unity. The reason is probably because opacity peaks lead to temperature gradient fluctuations, that lead to radial viscosity variations through the sound speed c , and thus corresponding variations in the gas radial flow.

3.4. Fragmentation, bouncing and mass transfer (“MTBF”)

The process of mass transfer (in high velocity collisions) encompasses an abbreviated range of conditions (Sec. 2.4.4), but can have a significant effect on certain aspects of particle growth over long periods

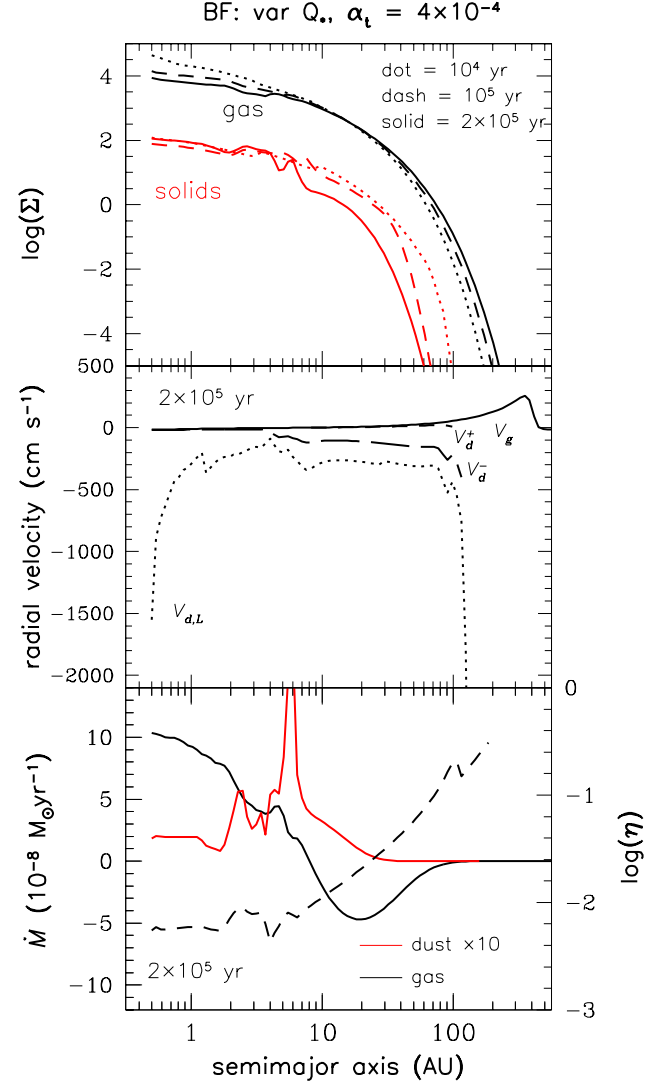


Figure 6. Fiducial model with bouncing and fragmentation (BF). Panel descriptions same as Fig. 4. Because growth times are longer, and particles generally smaller, the dust surface density has evolved much less than the F case after 2×10^5 years. The radial velocities of the particles sizes of interest all reflect this trend. The dust mass accretion rate is larger because more mass is in the dust, and shows substantial variation due to interaction with the various EFs. See text for details.

(Windmark et al. 2012a,b, 2013; Garaud et al. 2013). In **Figures 7 and 8** we show the results of our fiducial model that also includes mass transfer. The evolution of temperature (top panel, Fig. 7) somewhat differs between this case and the previous case BF, in that T in the innermost nebula is slightly higher by 2×10^5 years, even though the water ice EF has moved inwards. The opacities also are similar in magnitude, but their radial distribution is different. The water ice EF has a larger radial extent here. Compared to the BF case, there is a much larger drop in the opacity inside the ice EF and a much larger opacity enhancement outside it, suggesting (like in case F) that there is a larger difference between particle sizes inside *vs.* outside the water ice EF. The large contrast across the water ice EF is also visible in

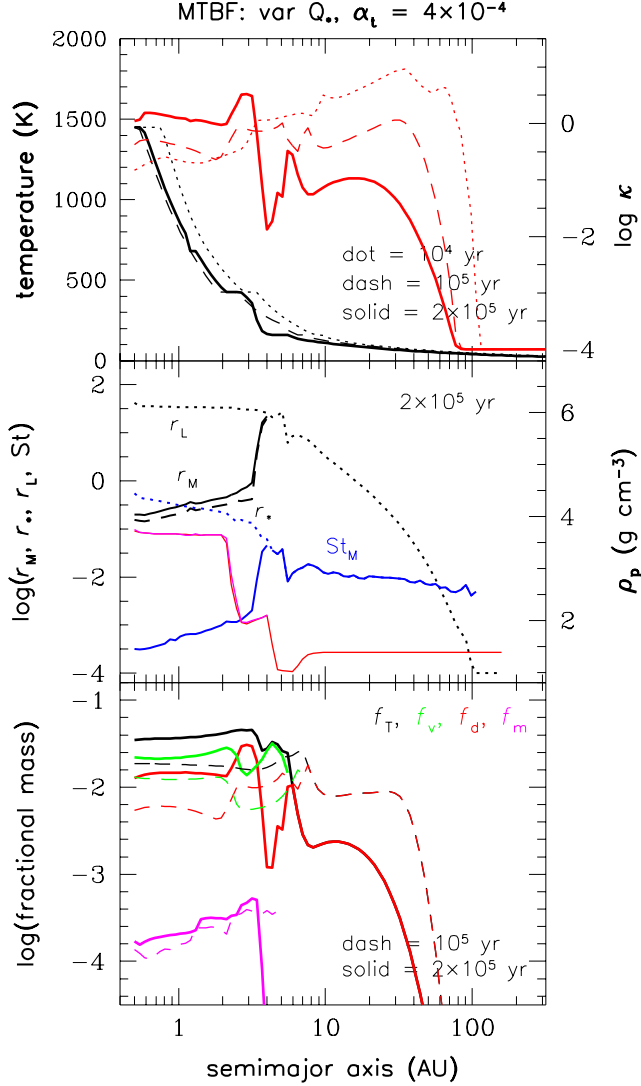


Figure 7. Fiducial model with mass transfer, bouncing and fragmentation (MTBF). Panel descriptions same as Fig. 3. In general, the MTBF case is quite similar to BF with the exception that growth in the migrators is slightly faster, and particle sizes are a bit larger. Overall, the enhancements one finds in both the dust and vapor in the inner nebula are similar to the BF case, except that more mass appears in the dust and less in the vapor. The temperatures in the silicate rich region are slightly hotter as well. See text for details.

the fractional mass plot (lower panel). The outer disk remains similar to case BF, but differences in the inner regions can be associated with the evolution of the particle size distributions. Overall, the total enhancement in the inner nebula is similar to the BF case, a factor of $\sim 5 - 6$, though with slightly more in the solids component and less in the vapor.

The contrast between particle sizes inside and outside the water ice EF is shown in the middle panel, where compared to case BF, growth at the larger sizes is faster and as a result the fragmentation size r_* has been reached further out in semimajor axis by 2×10^5 years. The effect of mass transfer appears to lead to two things. A slightly larger value of r_M relative to r_* most easily seen inside $R < 1.2$ AU, and consistently larger lucky parti-

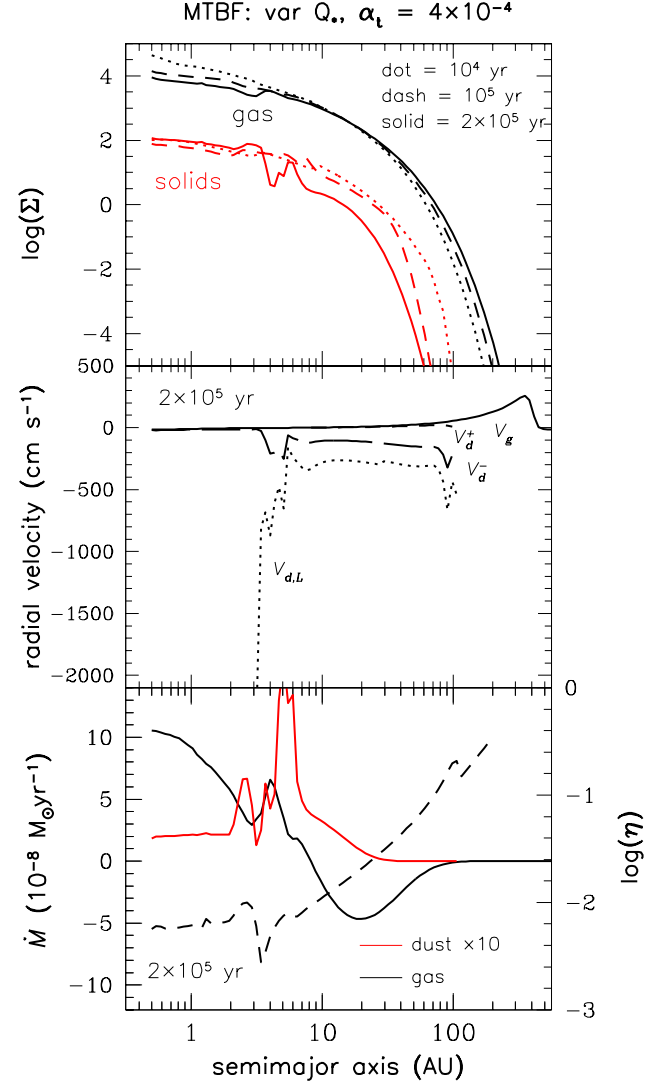


Figure 8. Fiducial model with mass transfer, bouncing and fragmentation (MTBF). Panel descriptions same as Fig. 4. The overall trends are similar to the BF case, especially in the outer nebula. Differences in the inner nebula can be attributed to the evolution of the particle size distribution when mass transfer is included. See text for details.

cles. These effects are much more evident when comparing the middle and lower panels of Fig. 2 which shows particle size distributions over this radial range. The lower panel, which refers to the MTBF case, is characterized by secondary peaks which are indicative of particles that are benefitting from particle collisions in which the growing particle accretes more mass than is eroded (see Sec. 2.4.4). A slight dip in r_L appears outside the the water ice EF which is associated with the large spike in fractional mass there. The particle mean density profiles are not much different from the BF case, except in the water ice enhanced region, with the differences tied to the different radial extents of the organic and water EFs in the two cases. In the ice-enhanced region just outside the ice EF, both r_M and r_L are larger when mass transfer is playing a role.

The velocity trends in **Figure 8** are qualitatively sim-

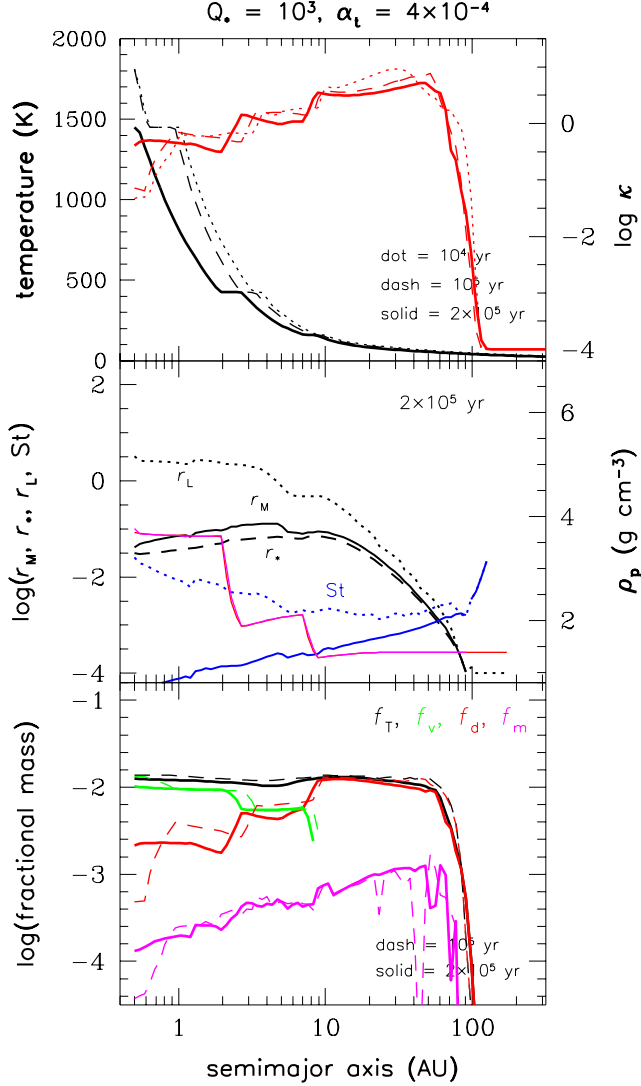


Figure 9. MTBF model assuming a constant fragmentation energy $Q_* = 10^3$ (Q103). Panel descriptions same as Fig. 3.

ilar to the BF case. The most noticeable differences appear in the radial velocities (middle panel). The presence of much larger lucky particles inside the water ice EF that are migrating inwards with relatively larger radial velocities (Eq. [40]), accounts for the much steeper inwards increase in $V_{d,L}$ compared to the BF case. Also, whereas V_d^- drops off gradually to its lowest value in the BF case between $\sim 3 - 4$ AU, a relatively sharp bump appears in the MTBF case because the fragmentation barrier has been reached and most of the mass here is in larger particles which influence the gas. This coincides with a stronger peak in \dot{M} than what was seen at the same location in the BF case. The corresponding pressure gradient also takes a much sharper drop here (lower panel).

3.5. Models with constant Q_*

We have employed a variable Q_* (and bouncing barrier) in all of the models presented thus far, motivated by experimental results that suggest that icy aggregates are

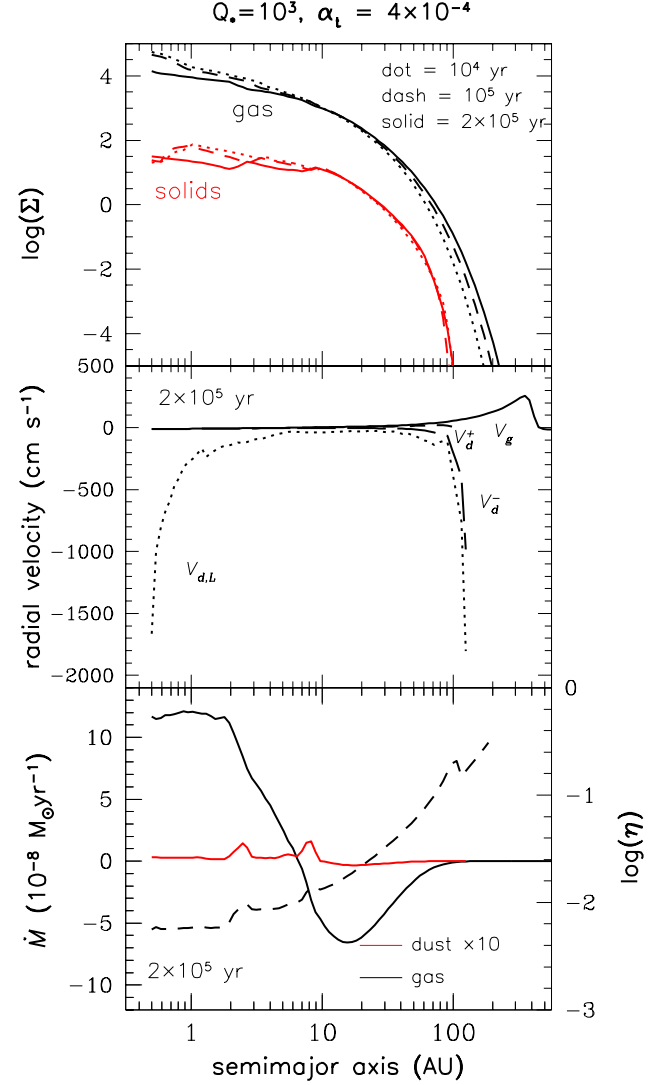


Figure 10. MTBF model assuming a constant fragmentation energy $Q_* = 10^3$ (Q103). Panel descriptions same as Fig. 4.

stickier and indeed stronger, at the velocities in question, than silicate aggregates (see Sec. 2.4.2). In this section, we present MTBF simulations that assume constant values for material strength, choosing two extreme values for $Q_* = 10^3$ and $Q_* = 10^7$ which would correspond to fragmentation velocities of ~ 30 cm s $^{-1}$ and ~ 30 m s $^{-1}$, respectively. Of these two, results of Beitz et al. (2011, for silicates) suggest that the larger value is especially unrealistic.

In **Figures 9 and 10**, we show our simulation results for $Q_* = 10^3$. Not surprisingly, this small value of Q_* means that particle sizes (middle panel, Fig. 9) are much smaller throughout the entire disk. As an example, $r_* \simeq 0.18$ cm at 1 AU in the MTBF case (where $Q_* = 10^4$ for silicate grains) whereas $r_* \simeq 0.02$ cm for this case, nearly an order of magnitude smaller. The maximum fragmentation size occurs around 10 AU. Because particles remain smaller, Stokes numbers are smaller which means there is less radial drift (and loss) of material over 2×10^5 years. The Stokes numbers for r_M decrease

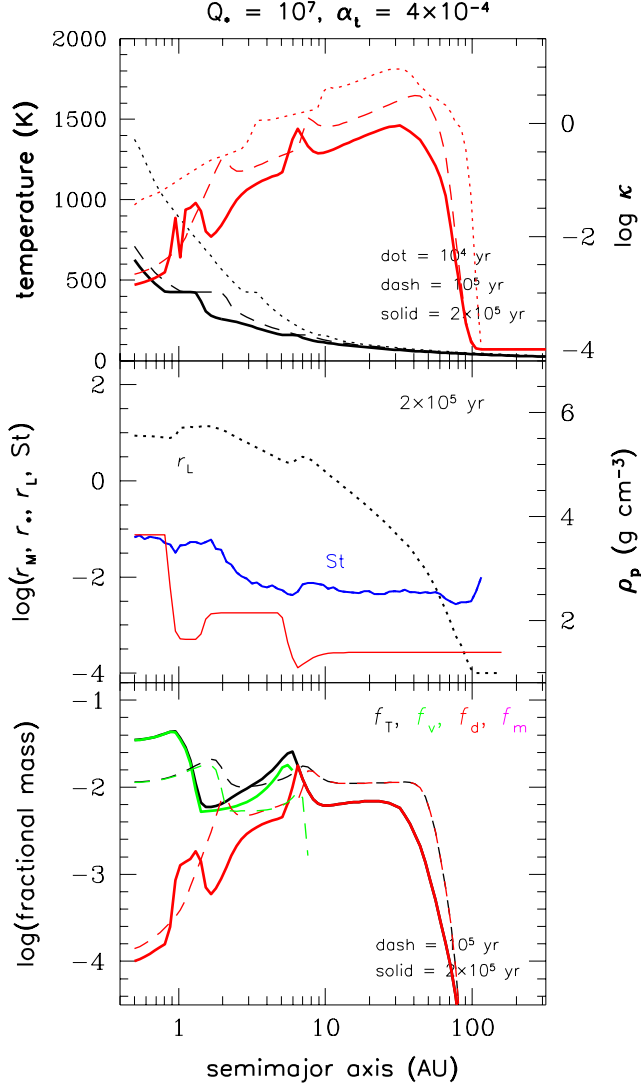


Figure 11. MTBF model assuming a constant fragmentation energy $Q_* = 10^7$ (Q107). Panel descriptions same as Fig. 3.

monotonically from larger values in the outer disk to $\text{St}_M < 10^{-4}$ in the innermost regions, and we do not see the roughly constant values as we did in the previous cases. Interestingly, however, we do see the St_L roughly constant, or $r \propto \Sigma$, relationship hold for the lucky particles in the outer nebula.

The temperature and opacity (upper panel) and the fractional masses (lower panel) further emphasize the sluggish disk evolution this case results in. The disk has only cooled significantly in the last 10^5 years, but still remains relatively hot partly because of a gradual increase in inner nebula opacity due to a small enhancement of solids. Unlike other cases we have seen previously, the outer edge of the water ice EF has moved very little, with a slight increase in radial extent. Because the fragmentation barrier is at such small sizes, migrators appear throughout the disk at a fraction of $\sim 10\%$ of the dust component. Moreover, the fractional mass in the outer disk has remained similar to its initial value because the gas and dust are still well coupled. Despite

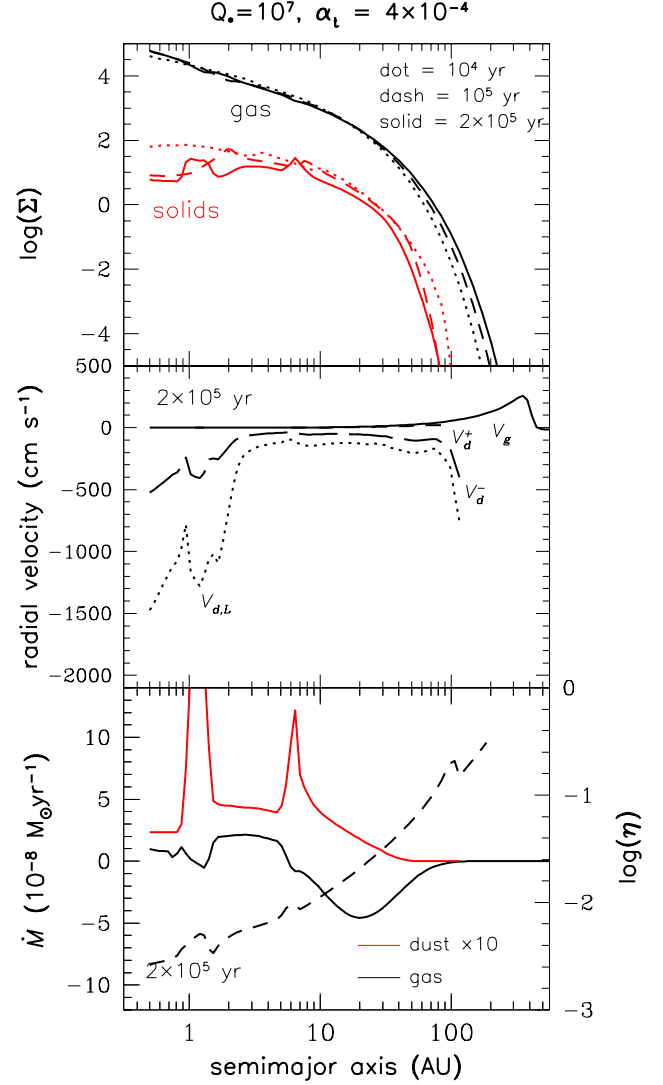


Figure 12. MTBF model assuming a constant fragmentation energy $Q_* = 10^7$ (Q107). Panel descriptions same as Fig. 3.

the sharp pressure gradient at the outer edge (dotted curve, Fig. 10, lower panel) a significant amount of solid material has advected outward, beyond 100 AU. The radial velocities in Fig. 10 (middle panel) are very close to the gas velocity everywhere except approaching the disk edges. In fact the inward drifting dust velocity component V_d^- diverges from nearly zero only at the outer edge of the nebula solids disk. The surface densities (upper panel) also show generally little evolution, and the dust accretion rate (lower panel) is muted. A low Q_* model thus appears to be a way to minimize the amount of solids loss over long timescales, as previously suggested by Birnstiel et al. (2009).

Figures 11 and 12 for $Q_* = 10^7$ show an entirely different behavior. In this case, the fragmentation size is so large that even after 2×10^5 years, $r < r_*$ everywhere (heavy dashed curve does not appear), even though $r_L \sim r_M$ is as large as ~ 10 cm in the inner nebula (Fig. 11, middle panel, dotted curve). The Stokes number neatly follows the nearly constant theoretical

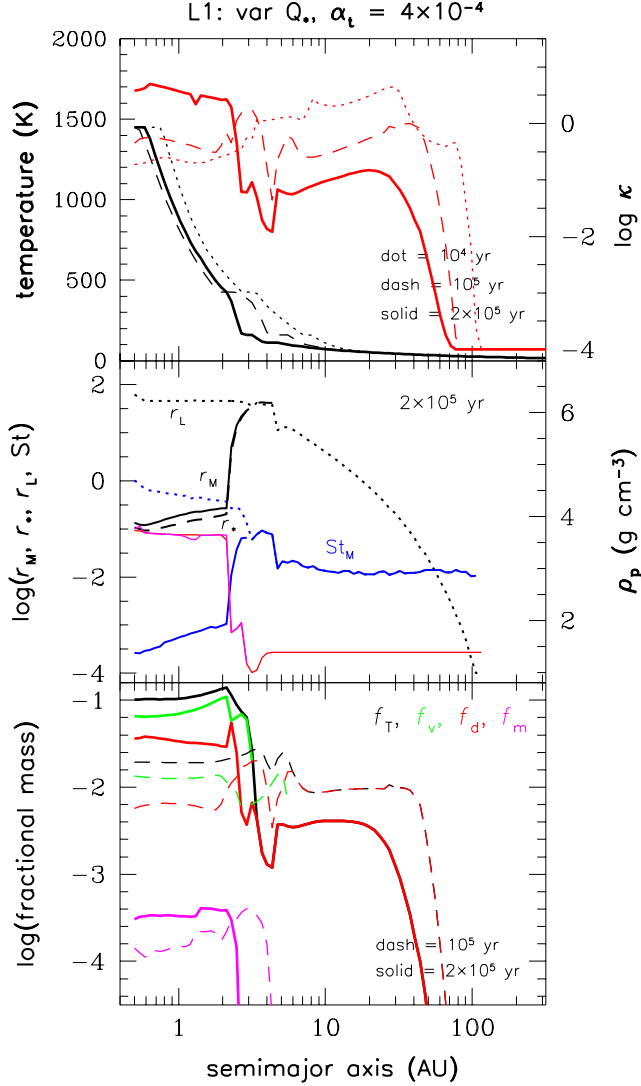


Figure 13. MTBF model assuming a star with 1 solar luminosity (L1). Panel descriptions same as Fig. 3.

“equilibrium” value in the outer disk, giving $r \propto \Sigma$ (see Sec. 3.2) but diverges from this relationship in the inner regions possibly because these relatively large particles may be in the transitional Stokes regime. The disk temperature (top panel) decreases quickly because the particles grow relatively quickly, and much of the material in the inner disk is beginning to be lost, leading to the substantial decrease in opacity. Despite the systematic loss of material, we still see two strong peaks in opacity due to the enhancements outside the organics and water ice EFs. These are also mirrored in the fractional masses (lower panel). We note an apparent peculiar difference between this case and other cases we have shown so far: the outer nebula solids disk has not “collapsed” as far as other models, despite the fact that the higher Q_* here allows growth to much larger particles, which should drift more quickly. The explanation is that the bouncing barrier we assume here (as in the case of $Q_* = 10^3$) is also a constant set at the silicate value, but is *not* scaled with Q_* (see Sec. 2.4.2), so that the dis-

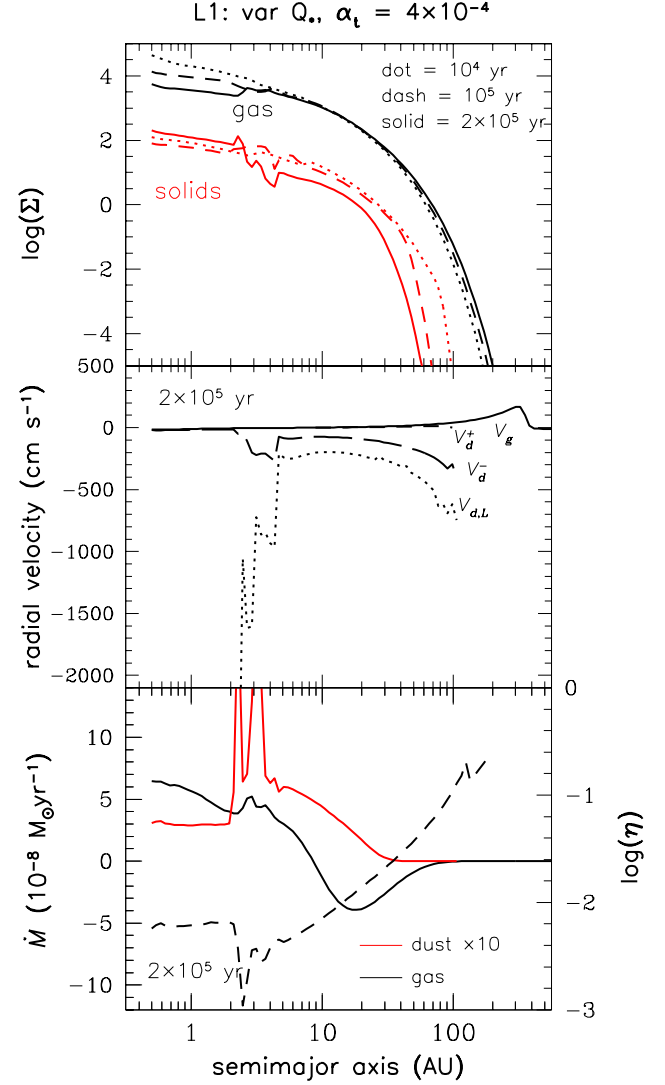


Figure 14. MTBF model assuming a star with 1 solar luminosity (L1). Panel descriptions same as Fig. 3.

parity between the bouncing and fragmentation barriers is especially considerable in this case. Not only does this mean that growth is slower since larger particles can only grow from particles smaller than the bouncing size, but the number density of those bouncing barrier-or-smaller-sized particles is always decreasing here because they are not being replenished by fragmentation.

Finally, looking at the radial velocities in Fig. 12 (middle panel), we see that the radial drift rates are larger in the inner nebula for both the largest particles ($V_{d,L}$) and the dust (V_d^-), explaining the significant loss of material from the inner nebula, the opposite of what was found in other cases. In this case, the gas surface density (top panel) has evolved the least of all the cases we have shown thus far, with values very close to the initial profile even after 2×10^5 years. In fact, in the innermost region, the gas density profile has become even steeper. This is because the rapid growth and loss of inner solar system solids has led to the lowest opacity, producing the fastest cooling and lowest viscosity. Remember that results like

this depend on the α_t -model prescription for viscosity increasing with temperature. The steady inward migration of material is also evident from the dust accretion rate that remains positive throughout the disk. The gas accretion rate is much less strong in this case in the inner regions because of the rapid cooling and steeper surface density.

3.6. A $1 L_\odot$ model

We have explored an MTBF model in which we fix the luminosity at $1 L_\odot$, as presented in **Figures 13 and 14**. Previous models have all used the time dependent luminosity model of D’Antona & Mazzitelli (Table 3, 1994) where the initial luminosity is of order $\sim 12 L_\odot$ and decreases to $\sim 3 L_\odot$ after 1 Myr. Thus here we can compare the effects of luminosity in the MTBF model. The primary effect one would expect is on the disk temperature (top panel of Fig. 13). We find only subtle differences in the overall temperature profiles, which are primarily associated with the radial extent of the water ice and organics EFs, and the overall steepness of the temperature profile inside this location. In particular, the gradient is so steep that the organics EF is traversed within one radial bin. The inner nebula shows only small changes because its energetics is dominated through these stages by local viscous dissipation rather than stellar irradiation. Differences in the Rosseland mean opacity profiles suggest that growth is proceeding a bit more rapidly in the outermost portions of the disk, at least at the earliest stages (10^4 years). This is also evident in the fractional mass plots (lower panel). The 10^5 year fractional mass curves look quite similar for this case and the fiducial MTBF case, but have slightly larger radial extent because of the location of the EFs. However, by 2×10^5 years the vapor and dust content in the inner regions are considerably higher than in the MTBF case, with an overall enhancement of an order of magnitude over the initial profile. The Stokes numbers corresponding to r_M and r_L (middle panel) are even flatter across the outer disk (and higher than in the MTBF case, which may explain why the outer disk evolved faster in the early stages here). In the inner nebula, there are also differences in the particle sizes relative to the MTBF case, which may derive from the increased number density of particles making mass transfer only slightly more effective for particles growing from r_* to near the size of r_M .

In **Figure 14**, the gas accretion rate profile is flatter, and its magnitude lower than the MTBF case. This is once again due to the steeper temperature gradient. In particular, one finds that the pressure gradient plummets much more sharply through the organics EF with this location corresponding to the sharp decrease in the solids accretion rate at ~ 2 AU just inside the strong organics peak. The peak in \dot{M}_d near the water ice EF is more intense, meaning that more solids are being delivered to the inner disk at this time compared to the MTBF model. Although a higher St_M in the outermost part of the nebula implies faster radial drift rates, these are hardly noticeable in the radial velocity plot (middle panel). In general, the radial velocities are similar to the MTBF case. Overall, the $1 L_\odot$ model makes little difference to disk temperature evolution at these early stages, though the outer disk is colder, and this may have led to

the subtle changes that we see in this model compared with the variable (higher) luminosity MTBF case. At later times, the higher (more realistic) luminosities may play a more important role in a relative sense.

3.7. MTBF model with high α_t (“HA-MTBF”)

As a final case, we compare a more viscous disk to our fiducial MTBF model; here the turbulence parameter $\alpha_t = 4 \times 10^{-3}$ (**Figures 15 and 16**). We expect that regions which are dominated by viscous heating should be hotter in this model, and indeed **Fig. 15** (top panel) shows high temperatures extending to larger distances from the star at the nominal time of 2×10^5 years. It is interesting that the higher α_t disk starts hotter than the nominal MTBF disk and cools to the current values, whereas in the fiducial MTBF model (and L1 as well) the temperature cools and then actually increases to the value at 2×10^5 years. The greatest differences we see between the two values of α_t , apart from the full silicates EF being present, have to do with the radial extent of both the organics and water ice EFs. Both fronts are further out, but are also smaller in radial extent than the MTBF model. The systematically decreasing T is naturally due to the decrease in Rosseland mean opacity as particles grow. Yet, the MTBF case shows an increasing T despite having larger particles because the enhancement leads to a higher opacity. In the HA-MTBF model, there is very little enhancement as is seen in the fractional mass (lower panel). Another clear effect of the more viscous disk is that the nebula gas evolves more strongly outwards, carrying a significant amount of solids with it (**Fig. 16**, upper panel). The strong outflow of solid material is also evident in Fig. 15 (lower panel) where after 2×10^5 years, the edge of the solids disk extends to about ~ 300 AU. Although the fraction of migrators is comparable between this and the MTBF case, the dust fraction in the innermost disk is less by an order of magnitude. Most of the solids are in the vapor phase.

The particle sizes (middle panel) also differ in an understandable way from the fiducial MTBF model. The relative velocities between particles are larger for the larger α_t , which means that the bouncing and fragmentation barriers are both reached for smaller particles. Comparing the middle panel of Fig. 15 with that of Fig. 7, we see that the fragmentation size r_* is now over an order of magnitude smaller. Interestingly, even while the *mass-containing* particles are smaller here, the *lucky* particles are not too much different in size from those in the fiducial MTBF case - so particles here can get even luckier relative to the nominal fragmentation barrier! This again may be due to the radial drift barrier being the limiting factor in how large these particles can grow (see discussion on Stokes numbers, Sec. 4). Increasing α_t by an order of magnitude has led to a smaller St_M in the inner regions - also by an order of magnitude, consistent with Eq. (56). However, St_M values are hardly changed outside the water ice EF. This suggests that the inner nebula is obeying fragmentation-barrier limitations, but something else - probably radial drift - is playing a role in the outer nebula (see Sec. 4.1).

In Figure 16, top panel, we can see that the larger α_t for this case has evolved the gas density much more, with Σ already at values typical of or smaller than a minimum mass nebula (e.g., Hayashi 1981) outside $\sim 4 - 5$ AU,

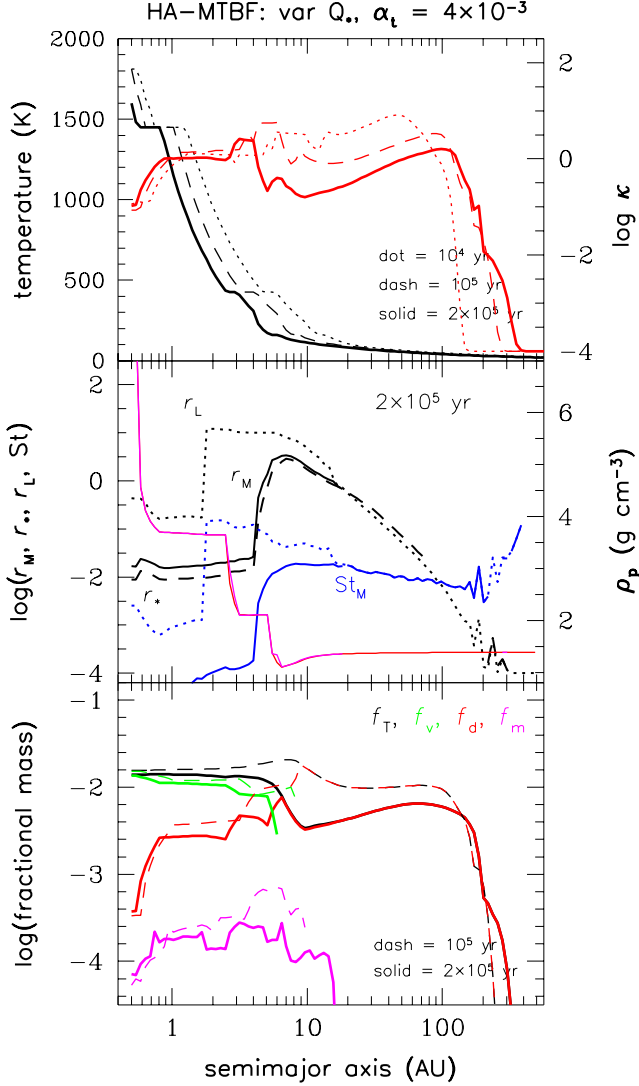


Figure 15. MTBF model assuming $\alpha_t = 4 \times 10^{-3}$ (HA-MTBF). Panel descriptions same as Fig. 4.

while inside the evolution has not proceeded as quickly and is similar to the MTBF value at 2×10^5 years because of the hotter, steep temperature gradient disk. In fact, the accretion rate of the gas (lower panel) shows that \dot{M} lingers close to zero between $\sim 1 - 4$ AU indicating very small gas advection velocities⁴. The mass flux reversal occurs much further out in the disk than the fiducial MTBF model, as one might expect with a much more viscous disk. The variations in \dot{M}_d are due to the various EF transitions but are more muted than the fiducial MTBF case again because of a low level of mass and opacity enhancement. The ‘bumps’ in solids as seen in the fractional mass profile may still be building up, however. Finally, the radial velocities (middle panel)

⁴ This is mainly due to the steepness of the temperature gradient. From inspection of Eq. (2), we can see how V_g can become positive. For example, if the temperature $T \propto R^{-s}$, it is easy to show that a reversal in sign will occur if, ignoring a term in the surface density $\propto \partial \ln \Sigma / \partial \ln R < 0$ for simplicity, $2 - s \lesssim 0$, where s is the power law exponent.

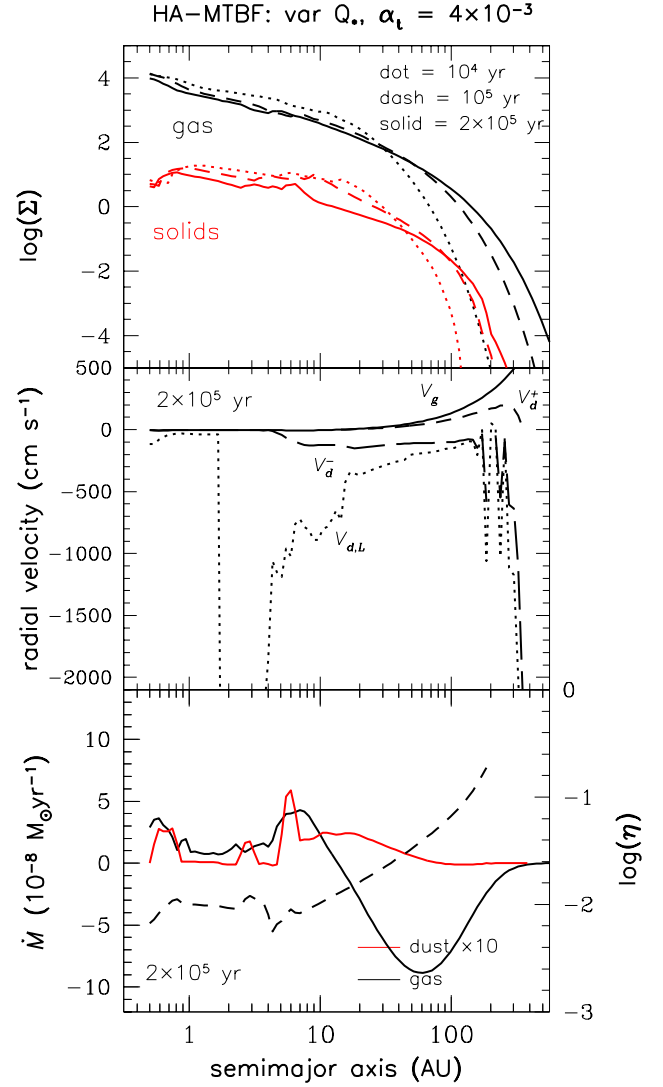


Figure 16. MTBF model assuming $\alpha_t = 4 \times 10^{-3}$ (HA-MTBF). Panel descriptions same as Fig. 4.

demonstrate that outward transport is more significant than the lower viscosity models. The gas radial velocity V_g increases more steeply in the outer nebula, and this affects the sizes (and amount) of particles that have positive (outward) velocities V_d^+ . The inward drifting solids component V_d^- is stronger than in the fiducial MTBF case, suggesting that at later times, vast regions of the outer nebula (between the water ice EF and ~ 100 AU) the disk may become depleted in solids.

4. DISCUSSION

In this section we review the effects of different sticking/bouncing/fragmentation schemes on particle size distributions, and note some implications regarding mm-cm wavelength observations of extrasolar disks (Sec. 4.1). Also in Sec. 4.1, we digress into how the tradeoff between growth and drift in *evolving* nebulae may explain a small but interesting difference between our results and previous work. Next, we look more closely at general implications of growth and drift for radial redistribution of

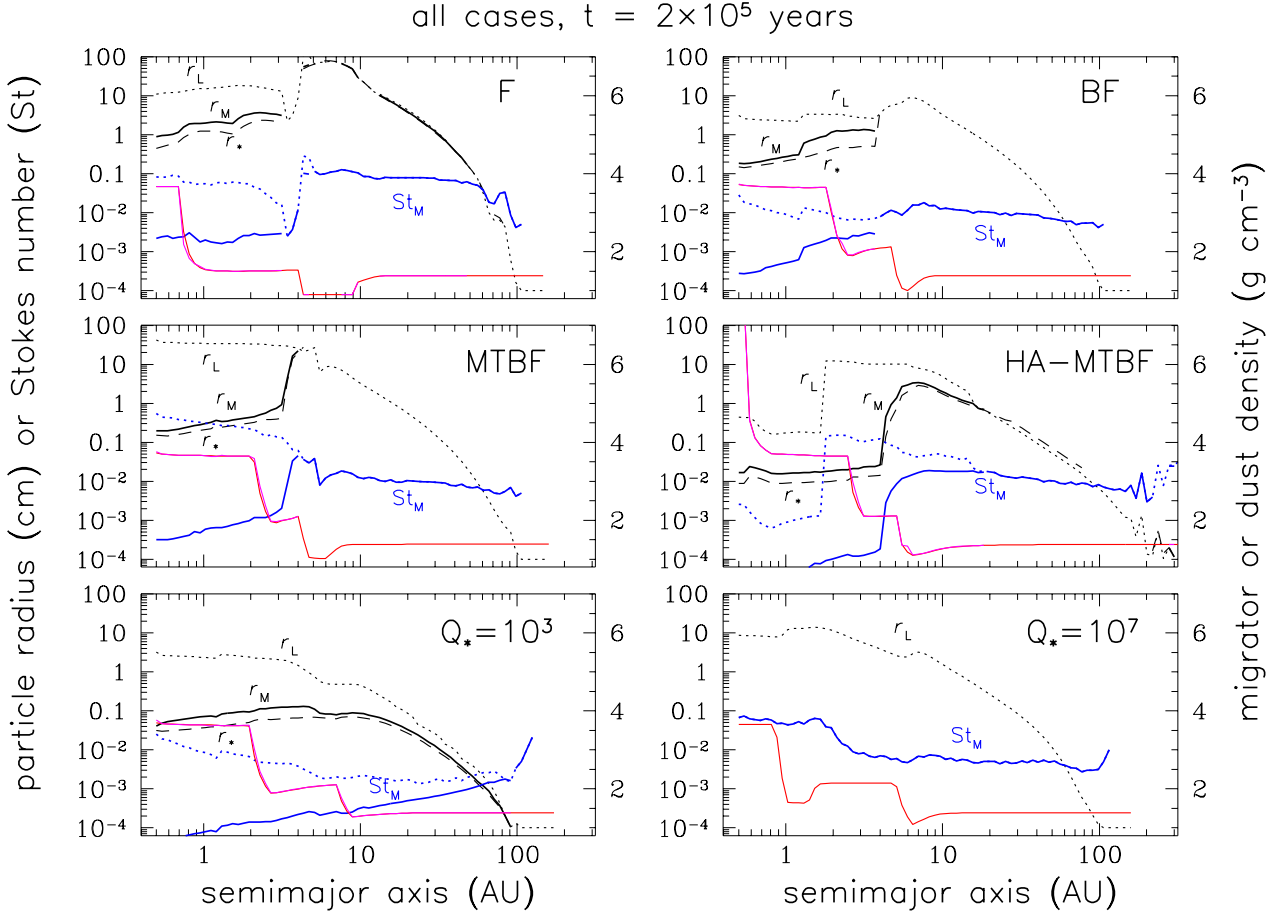


Figure 17. Summary of the particle size distributions after 2×10^5 years for a suite of models we have presented in this paper.

mass (Sec. 4.2), and note implications for meteorites, planetesimal formation, and perhaps even the radial distribution of planets. In Sec. 4.3 we look more closely at the effects of Evaporation Fronts, specifically on producing large objects enriched in, *e.g.*, water ice. We next discuss implications of our self-consistent opacities, in particular for mechanisms of turbulence generation and nebula gas evolution (Sec. 4.4). We conclude with some caveats and a short discussion of future work.

4.1. Particle size distributions; the drift and bouncing barriers

In **Figure 17** we collect the particle size distribution results after 2×10^5 years for the suite of models described in Sec. 3. Though there is considerable variation in particle sizes across the models, there are specific trends that are characteristic of all of these results.

In all figures, particle radii are shown in black and the corresponding Stokes numbers in blue. Particle internal densities are shown by the red/magenta curves. Recall that r_* (dashed lines) is the fragmentation radius, and r_M (solid lines) is the radius dominating the total particle mass. When r_* and r_M are plotted, the dotted line (r_L) refers to the largest “lucky” particle in a radial bin. Since particles of radius r_L contain a negligible amount of mass (section 3.1.1), we emphasize the mass-dominant particle

r_M . Recall that, if the heavy black lines for r_* and r_M do not appear, it indicates that the largest particle r_L (which in this case *does* contain most of the mass) has not yet reached the fragmentation size r_* .

The critical role of composition-dependent strength Q_* for limiting particle size is clear. In all the nominal cases where we allow icy particles to be stronger than ice-free particles, a matching step-function is seen in r_M and St_M . The constant Q_* cases, naturally, do not show this step. This simple result is explained, to first order, by the significant change in the fragmentation barrier (equation 56) when Q_* changes so significantly (see below for more discussion). In section 4.2 we discuss how this size difference leads to strong mass enhancement/depletion differences between the inner and outer nebula. Another general result is that while “lucky” particles $r_L \gg r_M$ can be found throughout the inner nebula (although carrying negligible mass), the outer nebula is devoid of such particles. That is, in the outer nebula the size distribution cuts off more sharply at its largest size. The same result is manifested in the Stokes number plots; this is discussed below. The most realistic cases (MTBF and HA-MTBF) show a peak in St_M and r_M just outside the ice EF, probably because of the locally enhanced solids mass. However, this does not hold true in the inner nebula where there is little if any correlation with the inner EFs and the distributions in r_M and St_M , with perhaps the exception of case F. The near-constant values of St_M

in most of the plots in Fig. 17 suggest fragmentation-dominated regimes, as can be understood from equation 56 in section 3.2 (recalling that T is only weakly varying in, at least, the outer nebula).

For our most realistic models (BF and MTBF), the inner nebula where the asteroids and terrestrial planets form (where the particle strength is lower because ice is absent) is capable of supporting growth only to 0.1–several mm radius, as has been shown previously (Zsom et al. 2010). This size is typical of “chondrules” which dominate unmelted meteorites. Our particles are not themselves “chondrules”, which *most* workers believe have been melted as freely-floating nebula objects, but represent aggregates of the right size to serve as their precursors. Just outside the ice EF, radii range from several dm to almost a meter. This might seem surprising in view of the iconic “meter-size barrier”, which is generally placed at $St \sim 1$ in a Minimum Mass Solar Nebula (Cuzzi & Weidenschilling 2006), but notice from the Stokes number curves that St_M remains in the range 0.01 – 0.1 because at this early stage the nebula gas density remains fairly high. This means that radial drift velocities and collisional velocities are still *increasing* as these particles grow. The sizes of particles in the outermost nebula depend most strongly on the strength of turbulence and the assumptions of the sticking model. Around 30 AU for case F, particles can reach 1 cm radius, but for other, more plausible cases, sizes at 30 AU are closer to 1 mm because of the inhibiting role of bouncing. Thus, even at this early stage, “bouncing” has played an important role in limiting the sizes of particles detectable by mm-submm observations (for more discussion see “Dissipation” below).

Our results thus generally agree with the results of previous workers (e.g., Brauer et al. 2008; Birnstiel et al. 2009, 2010; Zsom et al. 2010) that the fragmentation and bouncing barriers (along with radial drift; see below) limit particle growth. When only fragmentation is included (F), growth is quite rapid and stalls at particle sizes that are the largest amongst all of these cases. Yet, because particle growth reaches larger sizes, the disk mass drains most rapidly into the inner nebula due to radial drift (see Fig. 3, lower panel), with important consequences, as discussed below. The bouncing barrier (BF case), even if mass transfer is added (MTBF case), effectively reduces the rate of growth because a target particle is limited in the size of particles it can grow from. Thus in Fig. 17, we see that the fragmentation barrier has not been reached in the outer nebula by 2×10^5 years for the BF and MTBF cases. Like previous workers (e.g., Windmark et al. 2012a,b; Garaud et al. 2013; Drazkowska et al. 2013, 2014) we find that incorporating high-speed mass transfer (see Fig. 2) can allow the growth of a small number of “lucky particles” to sizes $r_L > r_*$; however, the mass contained in this population is extremely small at best, and they are absent in regions dominated by drift (see below).

Figure 18 compares several important metrics for a subset of these models to the observed, mass-dominant value St_M (solid blue). As noted above, the near-constancy of the mass-dominant particle Stokes number St_M through regions where Q_* is constant is largely explained by Eq. (56, red solid curve for St_*). However, while all the models follow the general trend of St_* , and

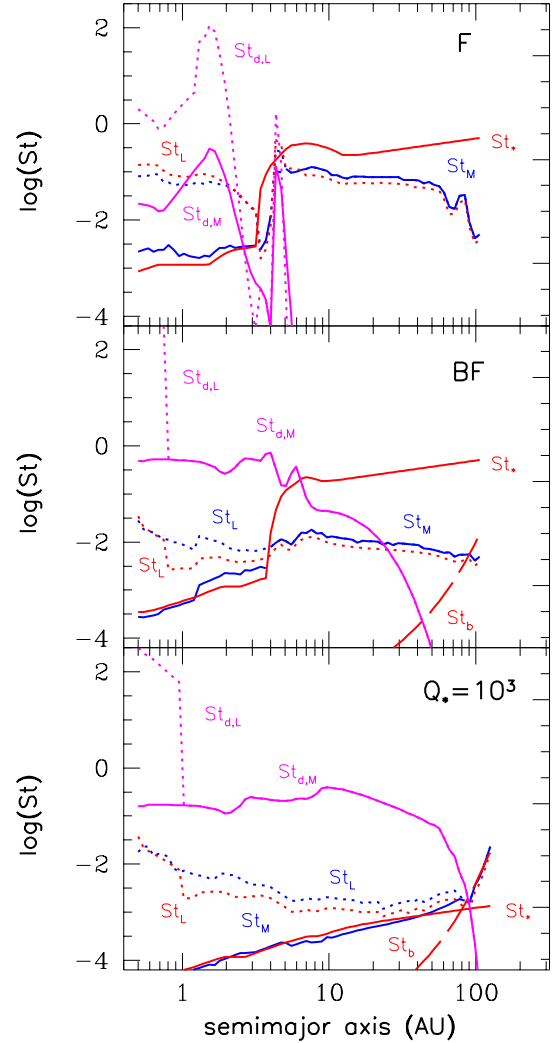


Figure 18. Comparison of our estimates for the fragmentation, bouncing, and radial drift Stokes numbers to the computed Stokes numbers for models F, BF and Q103 after 2×10^5 years. Radial drift dominates the outer disks in models F and BF. $St_* > St_M$ because systematic velocities are comparable to the turbulent velocities for these sizes. Only in model Q103 is $t_d > t_{gr}$ in the outer disk. See text for details.

quantitative agreement is excellent for the moderately realistic F, BF, and MTBF cases in the inner nebula (and at all radii under conditions of weak particles for $Q_* = 10^3$), quantitative agreement is poor in the outer nebula once bouncing and Mass Transfer are introduced (in the sense that $St_M < St_*$). This disagreement arises because Eq. (56) *assumes* that the collision velocity is dominated by turbulent relative velocities, and it turns out that, at least for the models presented here, given the small values of St_M , the large values of η in the outer nebula drive systematic drift-and-headwind related velocities that exceed the turbulent velocities, so Eq. (56) is an overestimate of the fragmentation barrier size. When bouncing is included, the discrepancy (vertical offset) increases since approach to the fragmentation barrier is now slower (particles larger than r_b can now only grow

from the small fraction of particles $r < r_b$), and St_M is “quenched” at smaller, non-equilibrium values by the evolving radial drift barrier, as described below. In the low-strength $Q_* = 10^3$ case, the fragmentation barrier is reached quickly everywhere with $St_M \sim St_*$. In the *inner* solar system, for cases F, BF, and MTBF, turbulent relative velocities dominate so the nominal St_* expression appears valid in all three cases. However, looking deeper, the situation actually presents a subtle puzzle, and to understand this we now estimate “limiting” Stokes numbers for bouncing and drift.

Digression: role of the “Drift Barrier” in setting r_M and r_L : We can derive a limiting condition for bouncing by setting $S_b(m = m' = m_b) = 0$ in equation (30), leading to $V_b^2 = C_0/m_b$. As in deriving the fragmentation limit, we set V_b equal to the typical collision velocity in turbulence for some radius r_b : $\Delta V_{pp} = c\sqrt{St_b}\alpha_t$, where the particle size can be related, approximately, to the corresponding St_b (using Eq. (57); also see, e.g., Birnstiel et al. 2011). We thus get the bouncing barrier Stokes number St_b :

$$St_b \simeq \left(\frac{6C_0\rho_p^2}{\pi\alpha_t c^2 \Sigma^3} \right)^{1/4}, \quad (59)$$

for which, in typical conditions, the strongest dependence is on the gas surface density.

While the importance of a “radial drift barrier” has been known since the early work of Weidenschilling (1988 *et seq.*), it has only recently been quantified and its influence is still being assessed. For instance, Brauer et al. (2008) simply assumed that $St = 1$ represented the radial drift barrier; this was echoed by Birnstiel et al. (2009, 2010). Birnstiel et al. (2012a) used a more realistic approach based on finding the particle size for which growth and drift timescales were equal. We follow the approach of Birnstiel et al. (2012a) and generalize it in several ways.

We derive our expression for the radial drift limited Stokes number St_d by comparing the radial drift time $t_d = R/U_r \sim R/\eta V_K St$ to the particle growth time $t_{gr} = m/\dot{m}$. As in Eq. (43), $\dot{m} \sim \pi r^2 \rho_d \Delta V_{pg} S$, where $S < 1$ is some average sticking coefficient which we will take as ≤ 0.5 for specifics. Approximating $\Delta V_{pg} \sim c\sqrt{\alpha_t} St$ as the turbulent relative velocity, whether for same-size or different-size particles (Ormel & Cuzzi 2007), and the near-midplane density to be $\rho_d = \Sigma_d/2h_d = f\Sigma\sqrt{St}/\alpha_t/2H$ ($f = f_d$ here), we get $t_{gr} = 2/3f\Omega$, essentially the same as Birnstiel et al. (2012a, their Eq. 13). Then, we simply define the particle radius r_d as the “drift barrier”, such that $t_d \lesssim t_{gr}$:

$$r_d \gtrsim \frac{3\sqrt{2}}{8} \frac{fS\Sigma}{\rho_p\eta}. \quad (60)$$

Note that the “drift barrier” is not simply determined by a drift velocity, but also depends on the *growth rate* through the amount of material available locally and the typical sticking coefficient. We relate r_d to a corresponding drift-limited Stokes number St_d , in either the Epstein

or Stokes regime, using Eqns. (57) or (58):

$$St_d \simeq \begin{cases} \frac{3\sqrt{2}}{4} \frac{fS}{\eta} & r_d < (9/4)\lambda_{\text{mfp}}; \\ \frac{1}{16} \frac{V_K}{\rho_p R \mu_m} \left(\frac{fS\Sigma}{\eta} \right)^2 & Re_p < 1; \\ \frac{1}{10} \left(\frac{V_K}{\rho_p R \mu_m} \right)^{1/2} \left(\frac{fS}{\eta} \right)^{4/3} \frac{\Sigma}{\alpha_t^{1/6}} & Re_p < 800, \end{cases} \quad (61)$$

If particles have $St > St_d$, they are drifting faster than they can grow. The first expression, valid for the Epstein regime, corresponds to equation (17) of Birnstiel et al. (2012a); however, our expression includes a factor of $S < 1$ and retains the full value of η , which is not always well represented by c^2/V_K^2 as in equation (17) of Birnstiel et al. (2012a). In both cases, a higher local mass density makes it easier for growth to dominate drift (increases St_d), and a stronger radial pressure gradient makes drift more dominant (decreases St_d).

We can now compare the calculated Stokes numbers (in blue), for the mass-dominant (St_M ; solid) and largest (St_L ; dotted) particles with our estimated limiting “barrier” values for fragmentation (St_* ; red solid), bouncing (St_b , dashed red) and radial drift (St_d , solid and dotted magenta as related to r_M and r_L respectively). As an indication of where the Stokes-Epstein regime transition lies, we also plot our approximation Eq. (58) for the Stokes regime (dotted red, see Cuzzi & Weidenschilling 2006, and Sec. 3.2). Our actual models (blue curves) use a smoother bridging expression, averaging over all particle sizes; the discrepancy between the red and blue dotted curves indicates that the effects of Stokes drag actually extend over a broad range of nebula radii. The bouncing barrier is active almost everywhere ($St_b < St_M$); as mentioned earlier, St_b does not provide an impermeable barrier, but merely slows growth for larger particles, which in principle could still reach the fragmentation barrier r_* given a long enough time (in the absence of drift).

The subtle puzzle in Fig. 18 is that while Birnstiel et al. (2012a,b) found, in general, that the radial distribution of the *size* of the mass-dominant particles in the outer nebula corresponded very well to the radial variation of St_d when drift dominated growth (actually they present the corresponding r_d instead of St_d), our results show St_M to have the shape of St_* rather than that of St_d , even when drift dominates ($St > St_d$).

We believe the explanation lies in a non-equilibrium behavior to which the nebula gas evolutionary models presented here lend themselves, but perhaps those adopted by Birnstiel et al. (2012a,b) do not. **Figure 19** shows the contents of Fig. 18 for case F, at three different times. The “drift barrier” St_d is larger than St_M throughout the nebula at early times, so growth dominates everywhere. The fragmentation barrier is reached at larger distances as time goes on because at early times f is nearly constant, and growth is more rapid at smaller distances where Ω is smaller (see t_{gr} above Eq. 60). By $2 - 3 \times 10^4$ yrs, St_* is reached nearly everywhere, while $St_d > St_M$. Meanwhile, growth to large values of St_M leads to rapid inward mass loss by radial drift, which decreases f , which in turn decreases St_d , so by 5×10^4 yrs, St_d has fallen well below St_M in the outer disk and by 10^5 years even for $R > 5 - 7$ AU, and growth has ceased. There is, however, nothing to *decrease* particle sizes be-

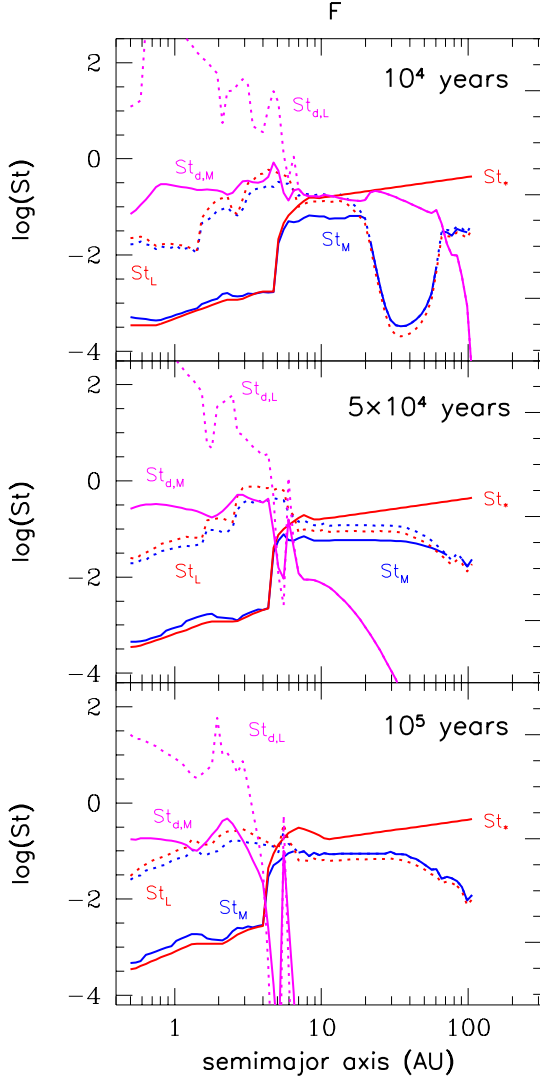


Figure 19. Comparison of the fragmentation, bouncing, and radial drift Stokes numbers to the computed Stokes numbers as a function of time, in case F. Here the transition from the growth dominated to the radial drift dominated regime is clearly shown. In a relative short time, the outer nebula solids are effectively transported to the inner nebula. See text for details.

cause $St_M < St_*$ still. Essentially the fragmentation-limited size of earlier times becomes frozen in, a fossil of an earlier era, while mass outside the ice EF continues to be lost to the inner nebula. A similar crossover behavior is seen for St_d and St_M in the BF and MTBF cases, at different times.

This behavior has interesting implications for mm-submm observations of disks. If it is true that the particle size distribution faithfully mirrors the instantaneous, underlying surface mass density, as in the models of Birnstiel et al. (2012a,b), then measurements of size through spectral index determinations should be consistent with inferences about total mass. Yet, Birnstiel et al. (2010b) actually come up with inconsistencies when comparing models with observations; they found that ad hoc reduction in the surface mass density is required relative to the model. While case F (Fig. 19) is

an extreme and indeed implausible case (the dominance of drift means that almost no mass is left over to form ice giants), the general decoupling of particle size distribution from simultaneous surface mass density provides a cautionary note. Other models (such as the MTBF case) also show an apparently fragmentation-limited size distribution represented by St_* nearly constant, but also show significant mass depletion relative to cosmic abundance. We believe that Birnstiel et al. (2012a,b) found a different behavior than do we because their underlying gas nebula, while formally evolving, is extremely large, so evolves in a much more leisurely way than does ours. It suggests that choice of initial disk size is something worthy of careful thought. As noted in section 2.1, different studies have adopted very different characteristic initial nebula lengthscales, and these differences may have unforeseen but interesting implications. For instance, it might be that if one *does* measure the solids surface mass density and particle size distribution of a disk simultaneously, one may be able to infer something about the evolutionary history of the region, and this is an exciting possibility.

Finally, the changing role of St_d vis-a-vis St_M helps us understand the variable abundance of “lucky” particles (the variable behavior of St_L vis-a-vis St_M) as seen across all the models of Figs. 18 and 19, in a simple way. In all cases, lucky particles vanish when $St_d < St_M$. This is because growing “lucky” particles relies on long periods of inefficiently sweeping up much smaller particles at a slow rate. Particles simply do not reside long enough in a region where drift dominates to exceed St_M , so their growth must have occurred entirely in environments encountered earlier, which are no longer present. As they drift inwards, they do grow, although too slowly to reach the fragmentation barrier. *Only* in a growth-dominated regime where drift is not a factor, can “lucky” particles $St_L > St_M$ appear. Inspection of Fig. 19 indicates that this rule holds across all three cases (as well as others not shown here). Lucky particles are common (although a negligible fraction of the total mass) in the inner nebula in all cases, because $St_d > St_M$ (Fig. 19). We note, however, that the frequency and abundance of lucky particles may be significantly increased if we implement porosity (Sec. 2.4.1). Okuzumi et al. (2012) find that if the particle porosity can get extremely high (volume density of $\sim 10^{-5}$) then drift behavior can change qualitatively. We explore this in future work.

4.2. Radial redistribution of mass, and some implications

We find that enrichment of the inner nebula in solids and vapor is a general, but not universal, result which seems dependent on the different Q_* associated with the inner outer nebula. As we have seen in our simulations, the higher fragmentation energy of icy particles allows them to grow large enough to drift radially in significant abundance over relatively short time scales, even with the bouncing barrier imposed. The lower fragmentation energy of silicate particles in the inner disk means that particles originating in, or drifting into, that region, after losing their ice, can only reach or maintain smaller sizes which do not drift quickly. Thus the high flux of material migrating into the inner regions from outside exceeds the loss flux towards the sun, leading to significant

enhancements in residual solids. Cuzzi & Zahnle (2004) identified the same effect with respect to vapor, which can become enhanced inside EFs because its inward removal rate by gas advection is smaller than its supply rate, in the form of solids drifting from outer regions.

It is illuminating to compare the mass enrichment/depletion results of the F, MTBF, and HA-MTBF cases (focusing on the red solid and dashed curves in the bottom panels of Figs. 3, 7, and 15; the MTBF and BF cases are fairly similar). The most obvious difference is in the outer nebula, where adding the bouncing barrier keeps particles, and associated radial drift loss, smaller. In case F, solids drain almost entirely from the outer nebula in $1 - 2 \times 10^5$ years, clearly problematic for outer planet formation. The HA-MTBF case represents another end of the spectrum, where the higher α_t keeps particles and their drift-loss smaller than the baseline F or MTBF cases, retaining outer nebula material longer and in higher abundance.

In the innermost regions, both the F and HA-MTBF cases show the least buildup of material but for different reasons. In the F case, particles become sufficiently large that they can be removed by drift on short timescales, even while growing. This effect becomes very strong between 10^5 and 2×10^5 years, after the outer nebula supply has ended, and even the inner nebula starts to drain away. Contrast this with the HA-MTBF case in which particle growth to larger sizes is limited by strong turbulence, Stokes numbers are low, and thus so is particle drift. As we pointed out before, the temperature gradient is also very steep so that the gas advection velocity is also small. Thus the solids distribution changes much more slowly. In the outer regions, strong outflow transports mass outwards countering the inflow from drift of larger particles. These effects conspire to keep enhancement low, though a peak is beginning to grow at the water ice EF suggesting that at later times enhancements may increase. For both these cases, the solids enhancements never gets large enough to lead to breakthrough growth to larger sizes (as in Brauer et al. (2008)). On the other hand, the slower particle growth rate of the MTBF case relative to the F case leads to smaller particles (but larger than the HA-MTBF case) which have slower radial drift rates, but relatively large enhancements of material in the inner nebula, at least at this stage in the evolution because of the strong mass inflow of material from the outer disk.

Previous workers (e.g., Stepinski & Valageas 1996, 1997; Ciesla & Cuzzi 2006; Garaud 2007; Brauer et al. 2008; Birnstiel et al. 2010) observed the transport of material from the outer disk to the inner regions, but generally did not see the same total enhancements as we do here. In all these studies one or more simplifications were made, but it is probably still true that the differential strength Q_* is the most important single factor. In the case of Stepinski & Valageas (1996, 1997), only icy material was treated, all solids vanished at the ice EF, no vapor tracking was included and a simplified particle growth algorithm was used, but some enhancement of solids in the ice-giant region was still seen due to inward drift from further out. While Birnstiel et al. (2010) did study differential strengths, their models merely changed the particle strength at the iceline without removing the associated icy material, so it is unclear just how large

an effect they would have predicted under more realistic assumptions.

At the next level of detail, one sees discrete radial peaks and valleys in the abundance of solid material, some quite narrow and pronounced. These peaks generally coincide with locations just exterior to various evaporation fronts (EFs) due to water ice, and “organics”, which dominate the condensible material in our model. We suspect that for our fiducial case, if the silicate EF were completely resolved within our radial grid, that a peak may appear there as well. Similar multiple features were pointed out by Garaud (2007). The radial locations of these peaks vary with the radial location of the respective EFs, which are in turn dependent on the viscosity, temperature, and ultimately opacity of the disk. Thus, the system is coupled thermally and dynamically to the particle growth process. One can even discern fluctuations in the *gas surface density* associated with these structures (see figures 4, 8, and 16, and section 4.4). Enhanced local mass density and/or smaller particles lead to higher opacity (as long as their size exceeds the peak thermal wavelengths), which affects midplane temperature and the EF. In case F, loss of solids leads to strongly falling opacity everywhere, and a cooling nebula, with more rapidly evolving EF locations. In cases MTBF and HA-MTBF, EFs actually evolve very little over the period of these simulations, allowing greater solids buildup behind them. The radial structure of the post-EF solids enhancements varies considerably, from an extremely narrow spike outside the water ice EF in case F (and MTBF), to somewhat broader “organic” buildups in cases MTBF and HA-MTBF (here a weak silicate buildup is present), each with associated opacity peaks. In fact, a glance at the red curves for \dot{M}_d in the lower panels of Figs. 4, 8, and 16 shows that even at the last time depicted, convergence of solids mass into narrow zones is still ongoing. While Garaud (2007) suggested that the amplitude of these peaks reaches a steady state in the long run, longer runs will be very instructive.

4.2.1. Implications of mass redistribution and particle size for planetesimal formation:

A subject of long-running interest is the still poorly-understood “primary accretion” of asteroids (in the inner nebula) and TNOs/KBOs/comet nuclei (in the outer nebula). Recently, attention has focused primary accretion scenarios in which such objects “form big”, leapfrogging the various barriers to accretion of which only the first few are discussed here (for the others, see Ida et al. 2008; Nelson & Gressel 2010; Gressel et al. 2012; Ormel & Okuzumi 2013). Two somewhat disparate avenues to primary accretion may be distinguished: “streaming instabilities” (SI) which operate nearly axisymmetrically in dense midplane layers (Goodman & Pindor 2000; Youdin & Goodman 2005), and “turbulent concentration” (TC) which is a clumpier process, acting throughout the nebula but also leading most effectively to planetesimals near the midplane (Cuzzi et al. 2001, 2008, 2010). A full discussion of this topic is beyond the scope of this paper (see Johansen et al. (2015) for a recent review). The conditions needed for SI are easier to assess, and we defer a discussion of the implications for TC to a future paper.

For SI to operate requires a midplane particle-to-gas ratio $\rho_d/\rho \gtrsim 1$ so the solids can drive the gas motions.

This has traditionally led SI advocates to focus on some combination of large particles, low turbulent intensity, and global enhancement of solids, usually due to late-stage removal of the gas. Related suggestions involve a reliance on “lucky particles” growing large enough to settle and lead to SI (e.g., Johansen et al. 2014), maybe if trapped at “pressure bumps” (Drazkowska et al. 2013), but it seems to us that under nominal conditions, “lucky” particles (those of radius r_L in our figures) are too rare and contain insufficient mass to drive collective effects such as SI (they might have other interesting implications as migrators, however). We believe it is more fruitful to explore the implications of the *mass-dominant* particles, represented by r_M and St_M . It is possible to express the local midplane value of ρ_d/ρ , simplifying Eq. (14, also see Appendix B) as in Cuzzi & Weidenschilling (2006) to $h_d/H = \sqrt{\alpha_t/St_M}$:

$$\frac{\rho_d}{\rho} = \frac{\Sigma_d}{2h_d} \frac{2H}{\Sigma} = f \frac{H}{h_d} = f \sqrt{St_M/\alpha_t}. \quad (62)$$

Figure 20 shows ρ_d/ρ with other quantities as a function of R (red dashed curve) for three representative models. In general, at this point in nebula evolution, $\rho_d/\rho < (\ll) 0.1$, but there is one intriguing situation in which ρ_d/ρ may eventually approach a value where SI might be possible, and it is right where longstanding expectations are that the first giant planet would form - just outside the iceline (most prominently, upper panel for L1). Moreover, this situation occurs quite early in nebula evolution and perhaps a longer simulation may eventually achieve this condition without the need to await photoevaporation or some other process to deplete the nebula gas. At this time and place, our results are showing particle radii of just over 1 cm, but recall that icy aggregates may not be able to compact fully and the identical St_M could arise for porous particles perhaps 10 or more times larger. Soon we will run our code for porous particles, and for longer times, to explore the possibilities for early planetesimal formation. While SI appears inoperative in the inner nebula at these timescales for α_t values studied herein or larger, because the weak silicate aggregates do not grow large enough to settle into the required dense layers, the particle sizes and density enhancements at these times are in the range of interest for TC, and also agree with what is seen in meteorites. It is increasingly suspected that *some* planetesimals *did* form in the inner nebula even at these early times, and it will naturally be of great interest to continue these simulations to the Myr timescales on which most observed chondrites form.

4.2.2. Other implications of mass redistribution for observations of different kinds:

The mass redistributions we see, fueled by the transport of material over large radial distances and the effects of Evaporation Fronts, have implications for a number of other currently puzzling observations. From the standpoint of mm-submm observations by ALMA and other radio observatories, the peaks and valleys in mass and opacity might provide a protoplanetary disk with a ringed appearance such as seen recently in HL Tau (Partnership, ALMA et al. 2015) and MWC 480

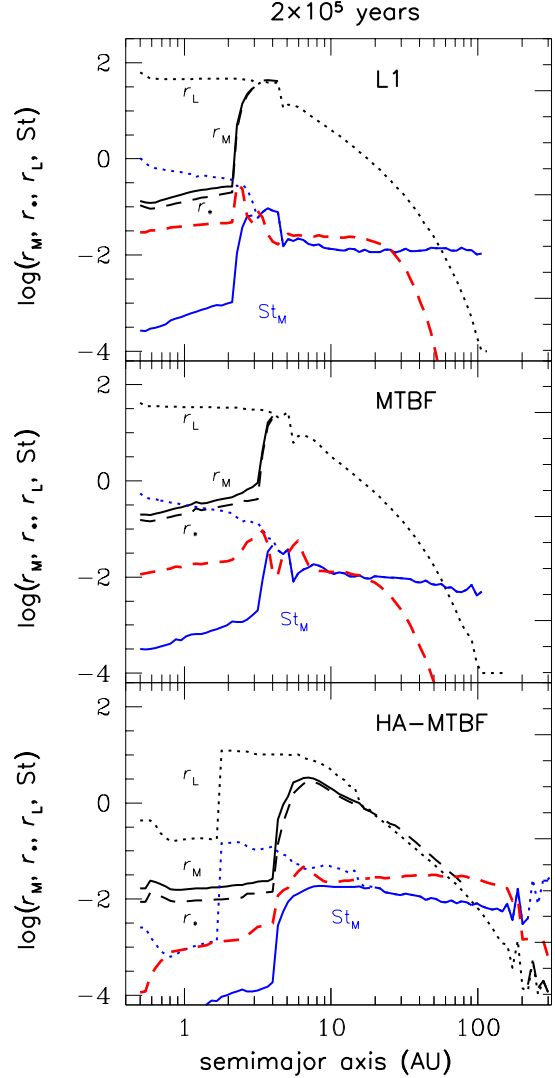


Figure 20. Radial profile of ρ_d/ρ near the midplane is shown in the red dashed line. Streaming instabilities require $\rho_d/\rho \gtrsim 1$. It appears that, for some cases (specifically the upper panel) SI may at some point be achievable over a narrow range of radii, right outside the ice EF - a location where the first giant planet has long been thought to arise. Of course, the absolute *location* where this circumstance occurs will depend on model parameters.

(Öberg et al. 2015). Our simulations to date have not included EFs for the “supervolatiles” thought responsible for the structure in MWC 480, but it would not be surprising to see a zoned or banded structure similar to that created by the ices, organics, and silicates we are currently modeling.

From the standpoint of meteoritics, a number of implications are evident. The enhancement of vapor in the inner nebula, a combination of evaporated water ice and “organics”, is especially large in the L1 case (factor of ~ 8). Depending on the state of the evaporated “organics” (see Sec. 4.5), whether CO, CH compounds, or higher hydrocarbons, the redox state of the inner nebula cannot help being influenced by this.

Another current meteoritics puzzle involves the anomalously high $^{17,18}\text{O}/^{16}\text{O}$ ratios seen in most chondritic ma-

terials relative to the sun (McKeegan et al. 2008), an enrichment that seems to appear some $1-2 \times 10^5$ years after the earliest “CAI” minerals condense, and to grow with time (Clayton 2003; Simon et al. 2012; Kita & Ushikubo 2012). Current thinking is that the heavy isotopes are liberated by a UV self-shielding process in the upper layers of the outer nebula (Lyons & Young 2005), become bound in icy particles, and drift inwards to evaporate in the inner nebula (Yurimoto et al. 2005). Photochemical models seem to be able to *produce* the needed material in a timely way (Lyons et al. 2009) but there has never been a demonstration that it could be transported to the inner nebula on such short timescales. Now, it seems at least several plausible models indicate that substantial outer solar system material can indeed reach the inner solar system within $1-2 \times 10^5$ years. More detailed models, coupling these transport models with $^{17,18}\text{O}$ formation rates in the outer solar system, are in order.

The peaks and valleys we see in the radial abundance of solids, even quite early on, may provide insight into the longstanding problem of the “small Mars” relative to Earth and Venus (Chambers 2001); planetesimals formed from such material through the entire terrestrial planet region might have been quite nonuniform in initial surface mass density. Naturally, the absolute locations of peaks and valleys depend on the actual radial locations of the various EFs, as they evolve with time. It will be of interest to see what longer runs reveal, but the mere occurrence of mass peaks and valleys with up to order-of-magnitude density contrast in the terrestrial planet region on radial scales of an AU or so are surely of interest. Moreover, all of our models show large-scale inward drift of outer nebula solids, to varying degrees. This effect alone might explain the compact surface *solids* mass densities inferred by Desch (2007) from early, compact giant planet configurations, even while the enveloping gas disk, with a certain amount of dust, might extend to much larger sizes. It is also well-known that “normal” (*i.e.* Kepler) planetary systems are much more packed with inner planets than is our solar system. The possibility of finding systematic causal factors for these important differences is intriguing.

4.3. Evaporation fronts; local refineries

Just outside EFs, we find significant peaks in the solids mass, created when drifting, vaporized material diffuses back outside the EFs, recondenses on small grains, and advects or diffuses some distance before becoming accumulated into a larger particle. These peaks and valleys in the fractional mass of solids, which move as the EFs evolve, may be observable in protoplanetary disks, as mentioned in Sec. 4.2. Additionally, we see that EFs lead to a distillation effect whereby the *composition* of material residing some distance outside each EF is enriched in the volatile that has just passed through that EF, and returned to recondense, leaving behind the more refractory material it had evaporated from, which continues to grow and drift radially inwards (Garaud 2007, previously referred to EFs as barriers to inward drift for the associated species). The red and magenta curves in the middle panels of Figs. 3, 7, and 15 track this compositional distillation through the internal *density* of local solids. For example, just outside the water ice EF the particle density drops from its “cosmic abundance” value

of roughly 1.5 to a nearly pure water ice value of 1, indicating that the solids there have become highly enriched in water ice relative to cosmic abundance. Of course, the same effect would occur outside each EF and would occur for the various EFs we are not tracking here as well. It is a way of creating radial belts of solids with very different composition than material on either side. The radial width and shape of these refinery or distillation zones depends on α_t primarily, but to some degree on the nature of the growth-by-sticking assumptions. Moreover, the radial zones evolve with time as the EFs and the mass flux through them vary, so longer simulations will be needed to what happens at later times. One can imagine interesting meteoritic and astrophysical chemistry associated with the EFs for silicates, troilite, and organics as well. This is a potentially rich area which also has implications for circumplanetary disks, and will be developed in future studies.

One prediction can be made in this regard, which we should mention here. The ice-enriched nature of solids immediately outside the ice EF, combined with our preceding results mentioned above, that the most likely place for early planetesimal formation to occur by SI is just outside the water EF, leads us to predict that Jupiter, say, if that were the planet first formed just outside the snow line, wherever that arose due to energetics details, would have a *water-enhanced core* relative to cosmic abundance. Perhaps Juno can test this prediction.

4.4. Nebula opacity

We have followed the evolution of EFs using a self-consistent calculation for the photospheric and mid-plane temperatures, that employs a new model to compute the Rosseland mean opacity of aggregate particles (Cuzzi et al. 2014a). The opacity depends on particle size, number density and composition, so it depends on the evolving particle size distribution and abundance. We have found that the opacity in the outer disk becomes quite small if growth proceeds quickly (particles growing larger than a thermal wavelength have smaller cross-section per unit mass), and/or if the loss of material to inward drift is high (less material). This tendency is weaker for models with higher α_t that keep particles smaller, allowing them to be retained longer and be more easily carried outwards as the disk spreads. In the inner region, the opacity can become larger with time, even though particles are growing to larger sizes (although slowly) if supply of material from the outer regions can keep the mass densities high. A sustained high opacity can maintain higher temperatures in the inner regions for longer periods. We also note that the radially variable opacity can even, apparently, lead to “lumps” in the *gas surface density*, because the opacity affects the local temperature and thus the viscosity in our α -model.

The evolution of opacity is important for two new hydrodynamic instabilities which apparently lead to sustained turbulence, without any need for magnetic fields or ionization, and are thus extremely important to the inner solar system which has been regarded as “dead” or at best “dull” from the standpoint of turbulence (Nelson et al. 2013; Turner et al. 2014; Stoll & Kley 2014; Marcus et al. 2013, 2014). The new instabilities (as currently understood) require a suitably rapid thermal equilibration, and thus prefer lower Rosseland mean

opacities. The limiting opacities have been estimated by Nelson et al. (2013) to be on the order of $1 \text{ cm}^2 \text{ g}^{-1}$ (perhaps up to $5 \text{ cm}^2 \text{ g}^{-1}$; Umurhan, personal communication 2015). In the outer nebula, our opacities remain at or below these nominal thresholds, but in the mass-enhanced inner nebula regions, opacities reach larger values. Whether the corresponding instabilities are damped or not under these conditions is thus a pressing topic for future study, perhaps even in a coupled fashion with particle growth.

4.5. Caveats and Future Work

There are several areas in which the code can be improved, which will be introduced in later papers. The initial conditions for the models in this paper are consistent with the earliest times in the nebula, but we have not added ongoing infall from the parent cloud. Such effects can be included through relatively simplified approaches (e.g., Birnstiel et al. 2010; Yang & Ciesla 2012).

None of the models presented here have reached a situation in which the mass fraction of vapor in the enhanced inner nebula exceeds the local H_2 -He gas density, but at least one has come within a factor of ~ 10 (the L1 model, Sec. 3.6) prompting us to consider that this situation may arise for a given model or at longer simulation times. Since this added vapor affects the disk viscosity, it is important to include its effects when this occurs. Furthermore, the local gas density influences the process of grain growth through the relative and radial velocities, thus a more self-consistent treatment requires that the volatilized-condensible vapor component is included in any calculations that involve Σ .

There are several areas in which we can improve the treatment of particle growth and composition. Most pressing is to explore the role of porosity. The moments method we utilize for coagulation is ideally suited for this (Estrada & Cuzzi 2008). The fractal growth of particles by low velocity sticking of small monomers will cause the particles to have a much lower density than the solid density of the monomers themselves (e.g., Dominik et al. 2007; Ormel et al. 2008; Zsom et al. 2010). Coupled with the stickiness and strength of icy particles, it has been argued by some workers that these fluffy aggregates can grow large, but maintain low relative velocities, allowing for continued growth without compaction (Okuzumi et al. 2012; Ormel & Okuzumi 2013). In the extreme case that a particle grows with a fractal dimension of exactly two, the stopping times remain the same for a single monomer. Thus, a model like our Q107 case with higher porosity might allow particles to grow faster and overcome the radial drift barrier. Furthermore, as we have noted in Sec. 2.4.4, our assumption of a gaussian PDF for the relative velocities in our calculation of the migrator destruction probabilities has been called into question from more recent work (e.g., Galvagni et al. 2011; Windmark et al. 2012b), thus we intend to explore the more rigorous model of Garaud et al. (2013) in future modeling efforts. The choice of PDF may very well affect the frequency of lucky particles which may modify some of our conclusions here.

Other improvements concern our treatment of EFs. Currently we make the simple assumption that inwardly migrating particles lose all their volatiles at the corresponding EFs, while modeling the EF as a radial range

of nearly constant temperature, centered on the species evaporation temperature and buffered by evaporation of the associated source of opacity. Though this works well for particles of the size we are so far growing, it may fail to capture the case of a much larger particle where a particle's surface layers can insulate its material at depth while it drifts a considerable distance. Further sweepup of local refractories may effectively trap any volatiles remaining deep within the particle and offer a way to deliver volatiles deeper into the inner regions of the nebula (e.g., Supulver & Lin 2000).

We have also assumed that evaporation and condensation are reversible processes for simplicity, but this is certainly not always the case. In particular, the “evaporation” of “organics” may instead be a decomposition of the original complex molecules into nearly inconducible species like CO or CH_4 , which participate in gas-phase chemistry rather than recondensing outside of the “organics” EF. This loss of refractory, carbon-rich organics must, at some level, be a one-way street, because none of the most primitive carbonaceous chondrites contains more than about one-tenth of the carbon found in comets (see Cuzzi et al 2003 for a discussion and references). This loss of refractory organics may effect particle strengths as well, because organics are often found to be “sticky”, perhaps extending the range of “strong” particles to locations somewhat further inwards than the water ice EF.

Our radiative transfer treatment (section 2.3) assumes implicitly that the bulk of the energy released by viscous angular momentum transport is dissipated near the midplane, or at least in a fashion proportional to gas density, and is transferred vertically upward and outward to space, making the midplane the highest temperature location. However, in cases where viscosity is MRI-related (Turner et al. 2014), or VSI-related (Nelson et al. 2013; Stoll & Kley 2014), it may be that the dissipation maximizes at some altitude near one scale height, or even closer to the disk photosphere. Such a case can surely be modeled and probably parametrized for our evolutions. The magnitude of the effect can be estimated by considering that, in the worst case where the energy is dissipated right at the photosphere, half of it is lost to space immediately and half radiates downwards. So, the vertical temperature distribution (that we do not model) will become more nearly isothermal, but the midplane temperature at a given location may not change by more than a factor of $2^{1/4}$.

We expect there will be other innovations as our understanding of the problem improves, but our code is at least well suited and robust enough to readily accept all the new physics mentioned above. An additional layer of parallelization in mass bins will greatly speed up our code which will allow for more complexity, and will be implemented in the future. Finally, we note that this model can readily be applied to the circumplanetary disk environment.

Acknowledgements. We wish to thank Fred Ciesla, Sandy Davis, Steve Desch, Pascale Garaud, Uma Gorti, Phil Marcus, and Orkan Umurhan for helpful conversations. We especially thank Chris Ormel for bringing our attention to a flaw in our diffusion model, in an initial

version of the paper. We also wish to thank an anonymous reviewer for pointing out several aspects that will lead to the improvement of our models. We thank Cameron Wehrfritz for his help in the preparation of this manuscript. This work was supported by a grant from NASA's Origins of Solar Systems program and a large amount of cpu time awarded through NASA's HEC program, whose consultants also helped with parallelizing the code.

APPENDIX A: CODE ALGORITHMS

In Sections A.1-A.2, we describe how we separately solve the equations for the radial evolution of the gas (Eq. A-[1]), and that of the vapor and dust components (Eq. A-[11]) in the first two sections. In Sec. A.3., we then describe in more detail how the temperature and opacity are calculated. The calculations in Sections A.1-A.3 are all carried out at synchronization steps and thus are only done at regular intervals. In Sec. A.4. we further describe the details of how we solve for the relative velocities which are required for both coagulative and incremental growth. Sections A.5 and A.6 describe the algorithm for growth beyond the fragmentation barrier, and radial drift of migrators.

A.1. Gas Evolution Equation

We use an implicit finite differencing scheme to solve Eq. (1). Radial bins j are spaced logarithmically over the radial range $R_{\text{in}} \leq R_j \leq R_{\text{out}}$ such that

$$R_j = R_{\text{in}}(R_{\text{out}}/R_{\text{in}})^{\frac{j}{n_R-1}}, \quad (\text{A-1})$$

with $R_1 = R_{\text{out}}$ and $R_{n_R} = R_{\text{in}}$, and n_R is the total number of radial bins. We thus first rewrite Eq. (1) in logarithmic form, using equation [3] and the relation $\nu = \alpha_t cH = \alpha_t c^2/\Omega$:

$$\frac{\partial \Sigma}{\partial t} = \frac{3\Lambda}{R^2} \frac{\partial}{\partial \ln R} \left\{ R^{-1/2} \frac{\partial}{\partial \ln R} (R^2 \alpha_t T \Sigma) \right\}, \quad (\text{A-2})$$

where $\Lambda = \gamma k_B (\mu_H^2 GM_\star)^{-1/2}$. Finite differencing of Eq. (A-2) leads to the tridiagonal system $a_j \Sigma_j^{n+1} + b_j \Sigma_j^{n+1} + c_j \Sigma_{j+1}^{n+1} = e_j \Sigma_{j-1}^n + f_j \Sigma_j^n + g_j \Sigma_{j+1}^n$, where n is the time index for time t and $n+1$ for time $t + \Delta t_{\text{sync}}$. The coefficients are given by

$$\begin{aligned} a_j &= -\delta \Lambda R_{j-1/2}^{-1/2} (R_{j-1}/R_j)^2 \alpha_{j-1}^t T_{j-1}, \\ b_j &= 1 + \delta \Lambda (R_{j-1/2}^{-1/2} + R_{j+1/2}^{-1/2}) \alpha_j^t T_j, \\ c_j &= -\delta \Lambda R_{j+1/2}^{-1/2} (R_{j+1}/R_j)^2 \alpha_{j+1}^t T_{j+1}, \end{aligned} \quad (\text{A-3})$$

with $e_j = -a_j$, $g_j = -c_j$, $f_j = 2 - b_j$, and $\delta = (3/2)\Delta t_{\text{sync}}/(\Delta \ln R)^2$. Since bin spacing in our code is logarithmic, the $j \pm 1/2$ refer to the logarithmic center between bins j and $j \pm 1$.

A.2. Advection-Diffusion Equation

The advection-diffusion equation can be differenced in a similar way to that of the gas evolution. We begin by rewriting the RHS of Eq. (11) in logarithmic form

$$\frac{\partial \Sigma_i^{v,d}}{\partial t} = \frac{1}{R^2} \frac{\partial}{\partial \ln R} \left\{ D_{v,d} \Sigma \frac{\partial \alpha_i^{v,d}}{\partial \ln R} - R V_{v,d} \Sigma_i^{v,d} \right\}, \quad (\text{A-4})$$

where $\Sigma_i^{v,d} = \alpha_i^{v,d} \Sigma$, the first term on the RHS side is the diffusion term with $D_{v,d}$ the diffusion coefficient, and the second term on the RHS is the advective term. Dropping the specifics of whether we are treating vapor or the dust for now, and also suppressing the species subscript i , finite differencing again leads to a tridiagonal system for each species i , where the coefficients are for the *diffusion* term (1st term on RHS)

$$\begin{aligned} a_j &= -\delta \left(\Lambda_j^d R_j^{-2} \alpha_{j-1/2}^t \Sigma_{j-1/2} T_{j-1/2} R_{j-1/2}^{3/2} - \frac{1}{4} \alpha_j^t \Sigma_j T_j R_j^{-1/2} \Delta \ln R (\Lambda_{j+1}^d - \Lambda_{j-1}^d) \right), \\ b_j &= 1 + \delta \Lambda_j^d R_j^{-2} \left(\alpha_{j-1/2}^t \Sigma_{j-1/2} T_{j-1/2} R_{j-1/2}^{3/2} + \alpha_{j+1/2}^t \Sigma_{j+1/2} T_{j+1/2} R_{j+1/2}^{3/2} \right), \\ c_j &= -\delta \left(\Lambda_j^d R_j^{-2} \alpha_{j+1/2}^t \Sigma_{j+1/2} T_{j+1/2} R_{j+1/2}^{3/2} + \frac{1}{4} \alpha_j^t \Sigma_j T_j R_j^{-1/2} \Delta \ln R (\Lambda_{j+1}^d - \Lambda_{j-1}^d) \right), \end{aligned} \quad (\text{A-5})$$

with $\delta = (1/2)\Delta t_{\text{sync}}/(\Delta \ln R)^2$, and now, recalling Eq. (12) for D_d ,

$$\Lambda_j^d = \sum_k \frac{\rho_{k,j}^d}{\rho_j^d} \frac{\Lambda}{1 + \text{St}_{k,j}^2}, \quad (\text{A-6})$$

for the dust component, whereas $\Lambda_j^d = \Lambda$ for the vapor. The advection term (2nd term on RHS) requires that we use upwind/downwind differencing for the derivative that depends on the sign of the velocity $V_{v,d}$. If $V_{v,d} < 0$, we add terms to the a_j and b_j :

$$\begin{aligned} a_j &= a_j - \delta \Delta \ln R V_{j-1}^{n+1} R_{j-1} \Sigma_{j-1} / R_{j-1/2}^2, \\ b_j &= b_j + \delta \Delta \ln R V_j^{n+1} R_j \Sigma_j / R_{j+1/2}^2, \end{aligned} \quad (\text{A-7})$$

whereas if $V_{v,d} > 0$, we add terms to the b_j and c_j :

$$\begin{aligned} b_j &= b_j - \delta \Delta \ln R V_j^{n+1} R_j \Sigma_j / R_{j+1/2}^2, \\ c_j &= c_j + \delta \Delta \ln R V_{j+1}^{n+1} R_{j+1} \Sigma_{j+1} / R_{j+1/2}^2. \end{aligned} \quad (\text{A-8})$$

Finally, the remaining coefficients are $e_j = -a_j$, $g_j = -c_j$ and $f_j = 2 - b_j$ with velocities evaluated at current step n .

For the inner and outer edges of the disk, we impose a combination of Dirichlet and Neumann boundary conditions (Robin boundary condition) through the mass flux

$$\frac{\partial \alpha_i^{v,d}}{\partial \ln R} = -\frac{1}{D_{v,d} \Sigma} \left(\frac{\dot{M}_i^{v,d}}{2\pi} - R V_{v,d} \Sigma_i^{v,d} \right), \quad (\text{A-9})$$

where $\dot{M}_i^{v,d}$ is the mass flux of vapor (or solids) of species i . The boundary conditions are also made implicit, and

require the presence of ghost points just outside the boundaries. We extrapolate to find the values of the necessary quantities using polynomial methods.

Application of the inner ($j = n_R$) and outer ($j = 1$) boundary conditions requires that we alter the tridiagonal coefficients. We difference Eq. (A-9) by taking the derivative centered around the boundary points. In order to estimate the flux at time t^{n+1} for species i , we define $\dot{M}_{i,j}^{v,d} = \dot{M}_j^{v,d} \alpha_{i,j}^{v,d} / f_j^{v,d}$ where $\dot{M}_j^{v,d}$ is the total mass of solids or vapor in a bin. The modified coefficients for the boundaries, again dropping specifics of dust or vapor with the exception of the total fractional masses $f_j^{v,d}$ to avoid confusion, are then

$$\begin{aligned} b'_1 &= b_1 - a_1 \frac{\Delta \ln R}{\Lambda_1^d \alpha_1^d T_1 R_1^{1/2}} \left(2V_1^{n+1} + \right. \\ &\quad \left. \dot{M}_1 / \pi R_1 f_1^{v,d} \Sigma_1^{n+1} \right); \\ f'_1 &= f_1 - e_1 \frac{\Delta \ln R}{\Lambda_1^d \alpha_1^d T_1 R_1^{1/2}} \left(2V_1^n + \right. \\ &\quad \left. \dot{M}_1 / \pi R_1 f_1^{v,d} \Sigma_1^n \right); \\ b'_{n_R} &= b_{n_R} + c_{n_R} \frac{\Delta \ln R}{\Lambda_{n_R}^d \alpha_{n_R}^d T_{n_R} R_{n_R}^{1/2}} \left(2V_{n_R}^{n+1} + \right. \\ &\quad \left. \dot{M}_{n_R} / \pi R_{n_R} f_{n_R}^{v,d} \Sigma_{n_R}^{n+1} \right); \\ f'_{n_R} &= f_{n_R} + g_{n_R} \frac{\Delta \ln R}{\Lambda_{n_R}^d \alpha_{n_R}^d T_{n_R} R_{n_R}^{1/2}} \left(2V_{n_R}^n + \right. \\ &\quad \left. \dot{M}_{n_R} / \pi R_{n_R} f_{n_R}^{v,d} \Sigma_{n_R}^n \right); \end{aligned} \quad (\text{A-10})$$

with $c'_1 = a_1 + c_1$, $g'_1 = e_1 + g_1$, $a'_{n_R} = a_{n_R} + c_{n_R}$ and $e'_{n_R} = e_{n_R} + g_{n_R}$.

A.3. Opacity

We employ the opacity model of Cuzzi et al. (2014a) in order to calculate the variable Rosseland mean opacity κ of the evolving particle size distribution. Calculation of κ involves determining the wavelength-dependent, or monochromatic opacities κ_λ for a gas-particle mixture, which depend on an extinction efficiency $Q_e = Q_a + Q_s$ for grain size r and wavelength λ . The extinction is due to a combination of pure absorption, which is re-radiated as heat, at an efficiency Q_a , and scattering at an efficiency Q_s . Following Cuzzi et al. (2014a), we allow for nonisotropic scattering by adopting the common scaling (e.g., van de Hulst 1980)

$$Q'_e = Q_e - gQ_s = Q_a + (1 - g)Q_s, \quad (\text{A-11})$$

where the asymmetry parameter $g = \langle \cos \Theta \rangle$ is the first moment of the distribution of the scattered component, or phase function $P(\Theta)$, which describes the degree of forward scattering ($g > 0$, see Cuzzi et al. (2014a), their Eq. 3). Values of $g < 0$ are preferentially back-scattering and $g = 0$ is isotropic. Cuzzi et al. (2014a) give expressions for the absorption and scattering efficiencies in terms of the electric polarizability (van de Hulst 1980), which is a function of the particle size and complex particle dielectric constant.

Aggregate particles and Effective Medium Theory (EMT). We assume in our model that particles are compositionally heterogeneous, being granular aggregates of much smaller grains of all compositions that condense at the local temperature, as is consistent with observations of meteorites and interplanetary and cometary dust particles. Assuming our particles to be aggregates composed of much smaller elements which are themselves smaller than any relevant wavelength allows us to use Garnett Effective Medium Theory to calculate average refractive indices of their ensemble (see Appendix C, Cuzzi et al. 2014a). The Garnett model (see, e.g., Bohren & Huffman 1983) describes inclusions of some dielectric constant ϵ_0 embedded in a homogeneous medium of dielectric constant ϵ_m (which is vacuum here), and can be generalized to a multiple component, potentially porous medium composed of multiple species with different dielectric constants and volume fractions relative to the aggregate volume.

The monochromatic opacity κ_λ is then calculated from our averaged indices (obtained using Garnett theory) with

$$\begin{aligned} \kappa_\lambda &= \frac{1}{\rho} \int \pi r^2 n_d(r) [Q'_e(r, \lambda)] dr \approx \\ &\quad \frac{\pi}{\rho} \sum_k w_k^{\text{sim}} r_k^2 b_k Q'_{e,k}(\lambda), \end{aligned} \quad (\text{A-12})$$

where we have approximated the integral by a summation over all particle sizes k weighted by their discretized number densities b_k (cm^{-3}), and the w_k^{sim} are Simpson's trapezoidal rule coefficients. Note that $n_d(r) dr$ has been replaced with the bulk number density b_k which applies to both the dust and migrator populations. The bulk number density for the dust population is given by

$$b_k^d = \frac{2 - q}{1 - q} \rho_d \left(\frac{m_k^{1-q} - m_{k-1}^{1-q}}{m_L^{2-q} - m_{\min}^{2-q}} \right). \quad (\text{A-13})$$

In Eq. (A-13), ρ_d is the volume mass density of total solids in the column, m_{\min} and m_L the minimum and maximum masses in the dust particle size distribution (Sec. 2.4.1), and subsequently $b_k = b_k^m$ for migrator particles (Sec. 2.4.4). The Rosseland mean opacity is then calculated from Eq. (21).

The algorithm for calculation of the midplane temperature for each radial bin R_j is called at every t_{sync} in conjunction with the gas evolution and solids and vapor advection and diffusion. The calculation is iterative because the layer optical depth depends on the opacity through the evolving size distribution, which depends on T_j . We use a root finding technique to evaluate Eq. (20) in which each temperature estimate requires that we recalculate the dust fractions $\alpha_{i,j}^d$ and particle densities ρ_j^p , taking into account that the radial location can be an EF (Sec. 2.4.5), to determine κ . The new opacity estimate then determines a new T_j . Iterations continue until the change in T_j on any subsequent iteration is less than some tolerance level.

During the iteration process, there are as many as five possible circumstances regarding the previous bin temperature T_j and the new temperature T'_j ,

$$\begin{aligned}
1) & T_j < T_i + \Delta T_{\text{EF}}, T'_j > T_i + \Delta T_{\text{EF}}; \\
2) & T_j > T_i + \Delta T_{\text{EF}}, T'_j < T_i + \Delta T_{\text{EF}}; \\
3) & T_j, T'_j < T_i + \Delta T_{\text{EF}}; \\
4) & T_j > T_{i+1} - \Delta T_{\text{EF}}, T'_j < T_{i+1} - \Delta T_{\text{EF}}; \\
5) & T_i + \Delta T_{\text{EF}} < T_j, T'_j < T' < T_{i+1} - \Delta T_{\text{EF}};
\end{aligned} \tag{A-14}$$

which we consider when adjusting a radial bin's solids and vapor content. For example, in condition (1) and also condition (3) for the case in which $T_j < T'_j$, changes involve the conversion of solids of constituent i into vapor:

$$\begin{aligned}
\alpha_{i,j}^{d'} &= \alpha_{i,j}^d (T_i + \Delta T_{\text{ER}} - T'_j)(T_i + \Delta T_{\text{ER}} - T_j)^{-1}; \\
\alpha_{i,j}^{m'} &= \alpha_{i,j}^m (T_i + \Delta T_{\text{ER}} - T'_j)(T_i + \Delta T_{\text{ER}} - T_j)^{-1}; \\
\alpha_{i,j}^{v'} &= \alpha_{i,j}^v + \Delta \alpha_{i,j}^d + \Delta \alpha_{i,j}^m,
\end{aligned} \tag{A-15}$$

where, e.g., $\Delta \alpha_{i,j}^d = \alpha_{i,j}^d - \alpha_{i,j}^{d'}$. For the case in which all remaining solids are converted to vapor (condition 1) then $\alpha_{i,j}^d$ and $\alpha_{i,j}^m$ are simply added to $\alpha_{i,j}^v$. On the other hand, in a situation where vapor is condensing, for example condition (2), or also (3) but with $T_j > T'_j$ then we partition vapor onto both dust and migrators in the appropriate *area* fractions

$$\begin{aligned}
\alpha_{i,j}^{v'} &= \alpha_{i,j}^v (T'_j - T_i + \Delta T_{\text{ER}})(T_j - T_i + \Delta T_{\text{ER}})^{-1}; \\
\alpha_{i,j}^{d'} &= \alpha_{i,j}^d + x_j^s \Delta \alpha_{i,j}^v; \\
\alpha_{i,j}^{m'} &= \alpha_{i,j}^m + (1 - x_j^s) \Delta \alpha_{i,j}^v, \\
x_j^s &= \sum_{k=1}^{n_*} \pi r_k^2 \rho_k^d / (\sum_{k=1}^{n_*} \pi r_k^2 \rho_k^d + \sum_{k=n_*+1}^{n_L} \pi r_k^2 \rho_k^m),
\end{aligned} \tag{A-16}$$

where x_s is the area fraction of dust in solids. The iterated values of the mass fractions are then used to calculate the mean particle material densities and adjust the particle mass distributions. The final values of the mass fractions are assigned when the temperature has converged.

A special case in our code involves the conversion of troilite. Solid troilite is converted to vapor and metallic iron in the fraction $f_1 = 56/88$. For simplicity, we consider this reaction to be completely reversible, where more care must be taken in the reverse process to assure the fractions are correct.

A.4. Relative Velocities

In our calculations, we assign a single particle-to-gas and particle-to-particle relative velocity for the entire particle mass distribution (dust and migrators) within the subdisk “dust” layer, which is defined by the scale height h_D as described in section 2.2.3. This calculation uses a logarithmic spacing in particle radius from the minimum size r_{min} which is fixed in our code, to the largest size r_L .

The stopping times of solid particles t_k^s depend on the flow regime which depends on whether the radius of a particle is larger or smaller than the gas molecular mean free path (Sec. 2.2.1). For any height z , the stopping time for particle of mass m_k at radial location R_j is

$$t_k^s = \frac{2r_k^2 \rho_j^p}{3c_j \rho_j \lambda_j^{\text{mfp}}} \left[D_{t,j} + \frac{\lambda_j^{\text{mfp}}}{r_k} (A_t + B_t e^{-C_t r_k / \lambda_j^{\text{mfp}}}) \right], \tag{A-17}$$

where the gas density as a function of height is $\rho_j = \sqrt{2/\pi} (\Sigma_j / 2H_j) \exp[-\frac{1}{2}(z/H_j)^2]$ and the expression in brackets is the Epstein-to-Stokes regime transitional formula (Podolak et al. 1988), with coefficients $A_t = 1.249$, $B_t = 0.42$, $C_t = 0.87$ and

$$D_{t,j} = \frac{\rho_j c_j \lambda_j^{\text{mfp}}}{3\nu_m} - (1/\varepsilon) [A_t + B_t e^{-C_t \varepsilon}]. \tag{A-18}$$

where $\nu_m = \mu_m / \rho$ is the molecular viscosity, and $\mu_m = 1.3 \times 10^{-4} \text{ g cm}^{-1} \text{ s}^{-1}$. The transition between the Epstein and Stokes regimes is defined by $r_k \leq \varepsilon \lambda_j^{\text{mfp}}$ where the factor $\varepsilon = 9/4$ is typically used. In our code we have adjusted this value to get a smoother transition and found $3/2$ works better. For $r_k \ll \lambda_j^{\text{mfp}}$, the stopping time formula reduces to the Epstein regime $t_k^s = r_k \rho_j^p / c_j \rho_j$. For $r_k \gtrsim \lambda_j^{\text{mfp}}$, we utilize the Stokes regime equation

$$t_k^s = \frac{8}{3} \frac{\rho_j^p r_k}{\rho_j C_k^d \Delta V_k^{\text{pg}}}, \tag{A-19}$$

where ΔV_k^{pg} is the particle-to-gas relative velocity. The drag coefficient C_k^d depends on the particle Reynolds number $\text{Re}_k^p = 2r_k \Delta V_k^{\text{pg}} / \nu_m$ and is calculated using the prescription (Weidenschilling 1977):

$$C_k^d = \begin{cases} 24/\text{Re}_k^p & \text{for } \text{Re}_k^p < 1; \\ 24/\text{Re}_k^{0.6} & \text{for } \text{Re}_k^p < 800; \\ 0.44 & \text{for } \text{Re}_k^p \geq 800; \end{cases} \tag{A-20}$$

Since t_k^s depends on ΔV_k^{pg} for $\text{Re}_k^p > 1$, iterations will be required to determine the correct stopping time, and thus relative velocities.

We begin with equations (34-37) and solve for the gas radial and azimuthal velocities u and v at semimajor axis R_j as

$$u = \frac{\sum_k A_k \rho_k^d [B U_k + 2\Omega V_k] + 2B\Omega \eta V_K}{B^2 + \Omega^2}, \tag{A-21}$$

$$v = \frac{-\sum_k A_k \rho_k^d [(\Omega/2) U_k - B V_k] - \Omega^2 \eta V_K}{B^2 + \Omega^2}, \tag{A-22}$$

where $B = \sum_l A_l \rho_l^d$. These can then be inserted into the equations for the U_k and V_k and the individual component can be removed from the sums. That is, we solve for the component V_k (or U_k) by substituting the expression for v into the component equation for V_k (or U_k , e.g., Eq. [34] or [35]). This gives

$$V_k = \frac{(\Omega/2) F_k U_k + Y_k + \Omega^2 A_k \rho_k \eta V_K}{A_k \rho_k G_k}, \tag{A-23}$$

where $G_k = BA_k\rho_k^d - B^2 - \Omega^2$, $F_k = A_k^2\rho_k^d + B^2 + \Omega^2$, and

$$Y_k = A_k\rho \sum_{l \neq k} A_l \rho_l^d [(\Omega/2)U_l - BV_l]. \quad (\text{A-24})$$

Solving for the final expressions for the velocity components, we find

$$U_k = - \left[A_k\rho G_k Z_k + 2\Omega F_k Y_k + 2\Omega A_k\rho(\Omega^2 F_k + A_k\rho B G_k)\eta V_K \right] [(A_k\rho G_k)^2 + (\Omega F_k)^2]^{-1}, \quad (\text{A-25})$$

$$V_k = - \left[(\Omega/2)F_k Z_k - A_k\rho G_k Y_k + A_k\rho\Omega^2(BF_k - A_k\rho G_k)\eta V_K \right] [(A_k\rho G_k)^2 + (\Omega F_k)^2]^{-1}, \quad (\text{A-26})$$

where Z_k is given by

$$Z_k = A_k\rho \sum_{l \neq k} A_l \rho_l^d [BU_l + 2\Omega V_l]. \quad (\text{A-27})$$

The equations for U_k and V_k represent $2n$ equations that can be solved by matrix inversion using standard methods.

A.5. Migrator Growth and Radial Drift

If we define the mass of the dust subdisk in a radial bin R_j to be $M_j^{\text{sd}} = 2\rho_j^d h_j^d \mathcal{A}_j$ where the area of a radial bin is $\mathcal{A}_j = \pi(R_j^2 - R_{j+1}^2)$ and the subdisk layer height h_d is defined in Sec. 2.2.3), then the total mass of new “migrator” material created in time Δt_j is roughly (compare to Eq. [52] of section 2.4.5):

$$M_j^* \simeq M_j^{\text{sd}} \left(\frac{m_{\text{L}}^{2-q} - m_{*}^{2-q}}{m_{\text{L}}^{2-q} - m_{\text{min}}^{2-q}} \right)_j, \quad (\text{A-28})$$

Although the migrator population covers masses $m \geq m_*$, we consider the mass in this layer M_j^{sd} , including the fraction of dust lying in this layer, to be available for sweepup by all migrators. This mass does not reflect all the mass in radial bin j , as some fraction of “dust” occupies the upper layers beyond h_d . The migrator mass thus “created” in time Δt_j is assigned to the first total mass bin of the migrator population, $M_{1,j}^{\text{m}} = M_j^*$, while already existing total mass bins are shifted up by one in index.

Drift mass. Because we use an asynchronous time step scheme in our code, the timestep of a radial bin j is typically longer than that of bin $j-1$ which lies exterior to j . In order to account for the asynchronicity, we use a predictor/corrector method for the migrator mass drifting in. There are three circumstances that arise within this scheme: (1) a time step for bin $j-1$ was called at the same time as bin j ; (2) no time step was called for bin $j-1$ when a step for j was called; and, (3) it is a synchronization step in which all bins are called, but with the

appropriate time Δt_j^{sync} set for each radial bin such that all radial bins are brought to the same elapsed time. The synchronization step is the step in which all drift mass is accounted for. The three cases can be summarized as

$$M_{\text{pc}} = \begin{cases} M_{j-1}^{\text{drift},N} \frac{N_j \Delta t_j - (N_{j-1} - 1) \Delta t_{j-1}}{\Delta t_{j-1}} - \\ M_{j-1}^{\text{drift},N-1} \frac{(N_j - 1) \Delta t_j - (N_{j-1} - 1) \Delta t_{j-1}}{\Delta t_{j-1}}; \\ M_{j-1}^{\text{drift},N} (\Delta t_j / \Delta t_{j-1}); \\ M_{j-1}^{\text{drift},N} - M_{j-1}^{\text{drift},N-1} \times \\ \frac{(N_j - 1) \Delta t_j^{\text{sync}} - (N_{j-1} - 1) \Delta t_{j-1}^{\text{sync}}}{\Delta t_{j-1}^{\text{sync}}}, \end{cases} \quad (\text{A-29})$$

where $\Delta t_j^{\text{sync}} = N_{\text{sync}} \Delta t_{\text{min}} - N_j \Delta t_j$, and the superscript N refers to the most recent *stored* calculation, and $N-1$ the calculation previous to N .

Due to the nature of our parallelization of the code in radial bins, the most recent information for the drift mass is not available until a synchronization step. An individual radial bin j is assigned to a single processor, but requires information from $j-1$ regarding the mass drifting in. We store and use values from previous time steps for the mass that drifts out of bin $j-1$ into j and we use those as the basis of our calculation which leads to some small “out of phase” transport which is eventually corrected at a t_{sync} . Given that the amount of mass drifting in compared to the total mass of a bin is quite small, any temporary effect that may occur during regular time steps is minimal.

M_{pc} represents a total mass of migrators of various sizes available to drift inwards into radial bin j in time Δt_{j-1} , whose total mass per mass bin m_k is given by $M_{k,j-1}^{\text{drift}}$, such that $M_{j-1}^{\text{drift}} = \sum_k M_{k,j-1}^{\text{drift}}$. The actual mass available in the time step Δt_j (or in the case of a synchronization step, Δt_j^{sync}) is then scaled to $M_{k,j-1}^{\text{drift}'} = (M_{\text{pc}}/M_{j-1}^{\text{drift}})M_{k,j-1}^{\text{drift}}$. The particle mass distribution for bin $j-1$ will be different from bin j , thus we reinterpolate the drift mass distribution from bin $j-1$ onto the same particle mass range as bin j and add the contribution to the total migrator mass distribution $M_{k,j}^{\text{mig}}$. In the event that the particle mass range in bin $j-1$ does not all lie within the mass range of bin j , we (1) return to the dust population of radial bin j the mass of all migrators that are in sizes smaller than the fragmentation barrier mass of bin j ; and/or, (2) add new particle mass and total migrator mass bins to radial bin j for particles from bin $j-1$ that are larger than the most massive pre-existing particle in bin j .

Evaporation fronts. If radial bin j or $j-1$ (or both) lie within an EF, then inward drifting migrators will have their compositions altered through adjustment to the local nebula temperature. This means that some or all of their volatile will be removed and added to the vapor content. For an EF with evaporation temperature T_i , we adjust the mass fraction in species i of migrators from bin $j-1$

$$\alpha_{\text{EF}} = \alpha_{i,j-1}^{\text{m}} \left(\frac{T_i + \Delta T_{\text{EF}} - T_j}{T_i + \Delta T_{\text{EF}} - T_{j-1}} \right), \quad (\text{A-30})$$

with the evaporated fraction added to the vapor content of bin j :

$$\alpha_{i,j}^{\text{v}'} = \alpha_{i,j}^{\text{v}} + (\alpha_{i,j-1}^{\text{m}} - \alpha_{\text{EF}}) \frac{\Sigma_{j-1} \mathcal{A}_{j-1} M_{j-1}^{\text{drift}'}}{\Sigma_j \mathcal{A}_j M_{j-1}^{\text{m}}}. \quad (\text{A-31})$$

In Eq. (A-31) above, $M_{j-1}^{\text{drift}'}$ is the adjusted total mass of migrators drifting in to bin j in time Δt_j , M_{j-1}^{m} is the total mass of migrators in bin $j-1$, the ratio of which along with the ratios of gas density and bin area ensures we are adding the correct mass fraction to bin j . In the special case of the troilite EF, the above equation will have a $(1 - f_I)$ factor multiplied to the second term on the RHS, and we add the remaining factor f_I to the metallic iron dust fraction (see Appendix A.3).

Migrator growth. The incremental growth of migrators is described by Eq. (44). We assume that all migrator particles $m_{k,j}$ grow from both the dust content in the subdisk layer, and potentially other migrators to some new size $m'_{k,j}$ in time Δt_j . The fraction of dust and migrators accreted can be determined from the individual terms on the RHS of Eq. (44). The change in the total mass of migrators in mass bin k is estimated then from

$$\Delta M_{k,j}^{\text{m}} = \left(\frac{m'_{k,j}}{m_{k,j}} - 1 \right) M_{k,j}^{\text{m}}, \quad (\text{A-32})$$

which can be an overestimate for two reasons.

The first reason is that there is a limited amount of dust mass available in the subdisk that can be accreted. If it is found that more dust mass was accreted than lies within the subdisk, the excess is subtracted out and the particle sizes, densities and accreted mass are adjusted accordingly with the same factor taken from all sizes. Although the subdisk dust mass becomes negligible, more dust remains at higher altitudes, which can be mixed downwards by settling and diffusion.

The second reason is that the initial calculation can allow more mass to be accreted from migrator mass bin k by other migrators than is available in mass bin k . Under these circumstances, the entire redistribution of the migrators will need to be redone (perhaps multiple times) until only the mass available for accretion can be accreted. Under normal circumstances, after the growth calculation, we redistribute total migrator mass according to the fraction of Eq. (A-32) that was due to migrator accretion of other migrators. For every migrator total mass bin k , we loop over other migrator total mass bins $l \geq k$ (here l and l' represent dummy indices) and subtract out what those bins accreted from mass bin k

$$M_{k,j}^{\text{m}'} = M_{k,j}^{\text{m}} - (1 - f_\rho) \sum_{l \geq k} \Delta M_{l,j}^{\text{m}} \frac{S_{k,l} \rho_{k,j}^{\text{m}}}{\sum_{l'} S_{l',l} \rho_{l',j}^{\text{m}}}, \quad (\text{A-33})$$

where $S_{k,l} \rho_{k,j}^{\text{m}}$ represents the density fraction of material of particle mass bin k in the migrator population accreted by mass l , and $\sum_{l'} S_{l',l} \rho_{l',j}^{\text{m}}$ is the total density

fraction over all masses accreted by l , and is thus related to the total mass of migrator material available in the subdisk for a migrator to accrete from. The factor f_ρ is the fraction of dust accreted in Δt_j .

If it is found that more mass from a migrator bin is accreted than what is available (*i.e.*, $M_{k,j}^{\text{m}'} < 0$), we define a scaling coefficient for each bin k found to have more mass accreted from it than available:

$$\mathcal{A}_{k,j} = M_{k,j}^{\text{m}} \left[(1 - f_\rho) \sum_l \Delta M_{l,j}^{\text{m}} \frac{S_{k,l} \rho_{l,j}^{\text{m}}}{\sum_{l'} S_{l',l} \rho_{l',j}^{\text{m}}} \right]^{-1}, \quad (\text{A-34})$$

which weights the amount of material that is subtracted from a bin due to accretion from other bins, and becomes the coefficient for the sum on the RHS of Eq. (A-33). The overestimated mass is then $1 - \mathcal{A}_{k,j}$ which is subtracted out of $\Delta M_{k,j}^{\text{m}}$ once iterations that ensure the modified condition for Eq. (A-33) are satisfied for all k .

Once all growth calculations are done, as a final step we perform a reinterpolation of the mass histogram of migrators (including all related quantities) to a logarithmic mass bin spacing, and make sure that the criterion for the maximum number of bins per mass or radius decade is adhered to (see Drazkowska et al. 2013, 2014).

A.6. Particle Destruction Probability

Rather than adding another time consuming calculation in our migrator growth subroutine that would involve integration over multiple integrals to properly calculate the destruction probabilities, we discretize the destruction rates of a migrator particle of mass m_k due to dust and to other migrators as

$$\dot{\mathcal{P}}_k^{\text{d}} = \sum_{l=1}^{l_*} \mathcal{R}_{l,k}^{\text{coll}} \zeta_{l,k}, \quad (\text{A-35})$$

$$\dot{\mathcal{P}}_k^{\text{m}} = (1 - \mathcal{P}_k^{\text{m}}) \sum_{l=l_*+1}^k \mathcal{R}_{l,k}^{\text{coll}} \zeta_{l,k}, \quad (\text{A-36})$$

where summation to $l = l_*$ is over all dust masses up to the fragmentation barrier m_* , and the summation from $l_* + 1$ to k is over all migrators of mass m_k and smaller. Equation (A-36) for migrators contains an additional factor $\zeta_{l,k}$ that depends on the probability of *destruction* of migrators during the current time step. We account for the second integral (over time of growth) by using a discrete number of points over the time interval as it grows from m_k to m'_k . Different mass values between m_k and m'_k , along with their associated relative velocities, determine the destruction probability over the timestep. Because growth is relatively small in time Δt_j over a wide range of values of turbulent intensity α_t , a few points is generally enough, but more points are used when growth is fast, such as it might be the case for low α_t . The total probability of destruction of a migrator in mass bin k is

$$\mathcal{P}_k = \mathcal{P}_k^d + \mathcal{P}_k^m = \frac{\Delta t_j}{N_p} \sum_{p=1}^{N_p} \left(\sum_{l=1}^{l_*} \mathcal{R}_{l,k}^{\text{coll}} \zeta_{l,k} \right)_p + 1 - \exp \left[-\frac{\Delta t_j}{N_p} \sum_{p=1}^{N_p} \left(\sum_{l=l_*+1}^k \mathcal{R}_{l,k}^{\text{coll}} \zeta_{l,k} \right)_p \right], \quad (\text{A-37})$$

where the index p and N_p refer to the number of points used in the estimate. Once \mathcal{P}_k is determined, we can calculate the total mass of particles of size k destroyed as $M_k^{\text{dest}} = \mathcal{P}_k M_{k,j}^m$; this mass is returned to the dust population. Bins that suffer total destruction are removed if they are at the tail end of the distribution only. Bins with zero mass in the middle of the distribution are allowed.

APPENDIX B: PARTICLE DIFFUSIVITY AND SCHMIDT NUMBER

A quick survey of the fluid dynamics literature reveals that the term “Schmidt Number” (Sc) is widely used as the ratio of gas viscosity ν to particle diffusivity D_d for particles of arbitrary t_s . Minor complications arise if $Sc_g = \nu/D_g$, for the gas itself, is significantly different from unity (Stevenson 1990; Hughes & Armitage 2010, 2012) because many derivations of D_d relate particle diffusivity to gas diffusivity (Völk et al. 1980; Cuzzi et al. 1993; Cuzzi & Hogan 2003; Schräpler & Henning 2004; Youdin & Lithwick 2007); we will assume $Sc_g = 1$, but deviations are easily allowed for. Here we have adopted the formulation of D_d and Sc in Youdin & Lithwick (2007, henceforth YL07), who incorporated orbital dynamics effects. For discussion and validation of these formulations see Carballido et al. (2011), who also showed that the resulting particle layer thickness h_d varied as $St^{-1/2}$ for $St = 0.1$ to 100. This innocent-looking St -dependence, familiar from the results of Dubrulle et al. (1995, henceforth D95), hides several subtleties, and is not *quite* the final answer, as we sketch below.

A closed-form expression for the *particle* vertical scale height h_d can be obtained by integrating the vertical mass balance equation for the concentration *ratio* ρ_d/ρ (D95 Eq. 32; Garaud et al. 2007, henceforth G07, her Eq. 21), or treating mass balance using scaling arguments (Cuzzi & Weidenschilling 2006, henceforth CW06 (their Eqns. 4-7)). Written in terms of Sc , without worrying about its proper form (see however Schräpler & Henning (2004) for a pre-orbit-dynamics assessment), Eq. (22) of G07 for h_d/H is exactly reproduced (ignoring constants of order unity) by combining Eqns. (37) and (39) of D95 (but note that a factor of $\kappa_{t0} = 1/Sc$ has been lost in D95 Eq. (37), because Eq. (36) requires the normalized diffusivity $\bar{\kappa}_t = \kappa_{t0}\alpha_t/St$). Solving the diffusion equation for a particle/gas *ratio* is a preferred approach; because neither CW06 nor YL07 accounted for vertical variation of gas density; their expressions give $h_D > H$ when $St < \alpha_t$, which is unphysical.

CW06 assumed a constant gas density and so their result is directly comparable to the scale height h/H for the ratio ρ_d/ρ derived by D95 (her Eq. 36); in fact, it is

identical if both are expressed in terms of Sc generically. Thus, it can also be transformed to a proper particle layer scale height h_d/H using Eq. (39) of D95, also becoming identical (in terms of Sc , for a single particle) to Eq. (22) of G07 (again neglecting constants of order unity):

$$h_d/H = (1 + St Sc/\alpha_t)^{-1/2}. \quad (\text{B-1})$$

However, all these previous results from mass balance equations assumed a particle “settling time” t_{sett} given by the terminal velocity of a single particle under vertical solar gravity $= 1/St\Omega$. This is not appropriate for $St \gg 1$ particles which are underdamped, as pointed out by Weidenschilling (1984, 1988) who suggested using the inclination damping time of a layer of large particles ($= t_s$) as the “settling time” when $St \gg 1$. This idea was incorporated into the numerical models of Cuzzi et al. (1993) and used in a bridging expression constructed by YL07 (their Eq. 2) to derive their Eq. (6) for h/H , which ironically reduced exactly to the small- St ($Sc = 1$) expression in CW06 or Eq. (37) of D95. This is because (relative to the earlier expressions), the larger $Sc = 1 + St^2$ of YL07 (using their physically motivated Eq. 5) is exactly canceled by allowing for the slower “settling” times of very large particles. Equations (4-7) of CW06, substituting $Sc = 1 + St^2$ and $t_{\text{sett}} = t_s + 1/St\Omega$ from YL07, naturally lead to the same result: $h/H = (\alpha_t/St)^{1/2}$. While this has the proper behavior to account for the particle layers in the simulations of Carballido et al. (2011), which never exceed $0.1H$ in thickness, it remains nonphysical in the small- St regime for reasons noted above, so must be converted using D95 Eq. (39) into a true particle scale height:

$$h_d/H = (1 + St/\alpha_t)^{-1/2}, \quad (\text{B-2})$$

which is valid for all combinations of St and α_t in global turbulence, where the energetic eddy frequencies are comparable to the orbit frequency. In nonturbulent nebulae with densely settled midplane layers, the near-midplane turbulence is shear driven and eddy times τ_e are faster, requiring modification to these expressions; for discussions see Cuzzi et al. (1993) or YL07 (unfortunately Fig. 6 of YL07 does not correctly represent the model of Cuzzi et al. 1993, which also includes a dependence on τ_e , leading to the ambiguity of YL07 Fig. 7 discussed by Carballido et al. (2011), but this does not affect the overall results of YL07).

APPENDIX C: CODE TESTS

C.1. Coagulation

Our numerical code uses the moments method of Estrada & Cuzzi (2008) to solve the Smoluchowski equation (Sec.2.4.1) under the assumption that the dust distribution can be treated as a powerlaw $f(m) \propto m^{-q}$ up to some fragmentation mass m_* . The algorithm for the moments has been tested for both simple and realistic collisional kernels against the brute force solution to the coagulation equation for the cases in which the relative velocities between particles is systematic, or in the case where they are driven by turbulence. We specifically utilize the “modified explicit” approach to follow the growth of the largest particle r_L (Eq. (28), Estrada & Cuzzi

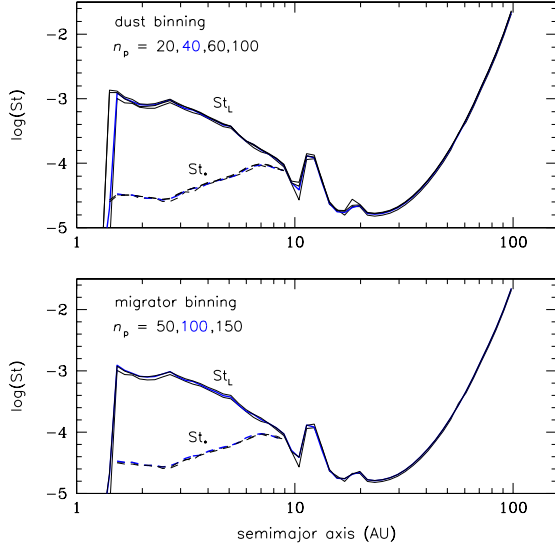


Figure 21. Upper panel: Comparison of the particle Stokes numbers after 10^3 years for four different choices for the number of bins per radius decade n_p for the dust population. The blue curve is our nominal choice for this paper. Lower panel: As above, but for the migrator population.

2008). This approach was also compared to the alternative growth formalism of Garaud (2007) and good agreement was found. Thus we do not repeat any tests of its accuracy here.

C.2. Mass and Radius Binning

In this section we check the influence of the choice of number n_p of logarithmically spaced bins per decade radius on the growth of particles in our code, both for the dust and migrator distributions. The moments method only requires a defined mass or radius histogram when calculating the collisional kernel, for example when solving for the particle-to-particle relative velocities, which must be integrated over in order to calculate the growth rate of m_L . This histogram is always well defined because of the strict adherence to a powerlaw in mass or radius. Nevertheless, because reasonably accurate growth requires sufficient sampling of the kernel quantities, especially for the migrators, the number of bins chosen per decade can have an effect on the results.

In the upper panel of **Figure 21**, we compare the Stokes numbers St_L and St_* (where defined) for a run of 10^3 years for the fragmentation only case and an assumed $\alpha_t = 5 \times 10^{-3}$, for four different choices of n_p . The blue curve represents the value we have chosen for this paper. Even given the variation of St_L over orders of magnitude, all of the choices produce very similar results with the lowest value $n_p = 20$ producing slightly more variation than higher values, but certainly within acceptable levels. The greatest difference occurs in the innermost bin, which also happens to coincide with the edge of an EF. This is not surprising since the temperature variation is quite sensitive to the particle size distribution. From these tests, it would appear that a choice of $n_p = 60$ (whose curve appears most similar to the value of 100) may be a best choice going forward. It is also

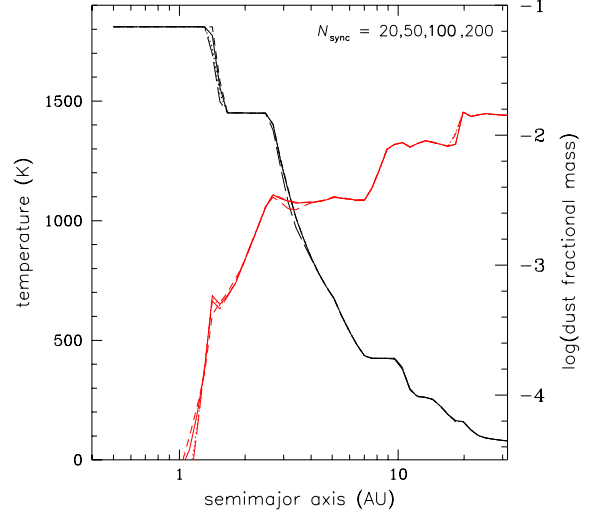


Figure 22. Temperature (black) and dust fraction (red) curves for different choices of the synchronization step. Our nominal choice is given by the solid curves. The relatively little variation indicates that the global processes such as the gas evolution and temperature calculation need not be done so frequently.

possible to vary n_p with R .

In the bottom panel of **Fig. 21**, we have instead varied the number of migrator radius bins per decade while using our nominal value for the dust distribution. We compare our nominal value for the migrator bins $n_p = 100$ (blue curve) to smaller and larger values and find that this choice is more than sufficient as the $n_p = 100$ and 150 lie right on top of each other. We note that our treatment of the migrator distribution binning is different from that of the dust distribution which is effectively Eulerian as are all the usual solutions of the Smoluchowski equation, which lead to the well-known concerns about mass resolution (Drazkowska et al. 2014). The migrator bins are, in fact, Lagrangian in that the migrator mass bins grow at different rates, and thus even a logarithmically equally spaced grid would become unequal in its spacing with time. However, in order to maintain a consistency of spacing, we rebin the migrator distribution, strictly conserving mass, after every iteration. The generally wide agreement between the variety of choices for n_p give us confidence that growth is being treated well at all particle sizes we achieve in our models.

C.3. Variation of N_{sync}

Global calculations in our code, such as the gas evolution, temperature and dust diffusion and advection do not need to be done every time step. This is the basis for our use of an asynchronous time stepping scheme. In this section we compare different choices of the number of steps N_{sync} our code executes before calling a synchronization step in which all properties of the nebula are brought to the same time.

In **Figure 22** we compare four different choices of N_{sync} with our nominal choice of 100 shown by the solid curves. We plot both the temperature (black curves) and the dust fractional mass (red curves) for the same model as above after 10^3 years. Again, we find that the agree-

ment across the different choices is more than adequate indicating that these processes are not changing quickly over a time scale of $N_{\text{sync}} \times \Delta t_{\text{min}}$. Most of the variation is due to the sensitivity of the temperature to changes in the particle size distribution. Even these appear to be minor, especially in this case of high α_t in which growth can be rapid.

REFERENCES

- Adams, F. C., & Shu, F. H., 1986, *ApJ*, 308, 836
- Bai, X.-N., 2014, *ApJ*, 791, article id. 137, 22
- Bai, X.-N. & Stone, J. M., 2010, *ApJ*, 722, 1437
- Bai, X.-N. & Stone, J. M., 2011, *ApJ*, 736, 144
- Bai, X.-N. & Stone, J. M., 2013, *ApJ*, 769, article id. 76
- Barranco, J. A., 2005 *BAAS*, 37, 1494, #196.02
- Beitz, E., Güttler, Blum, J., et al., 2012, *ApJ*, 736, 34
- Birnstiel, T., Dullemond, C. P., & Brauer, F., 2009, *A&A*, 503, L5
- Birnstiel, T., Dullemond, C. P., & Brauer, F., 2010, *A&A*, 513, A79
- Birnstiel, T., Ricci, L., Trotta, F., et al., 2010b, *A&A*, 516, L14
- Birnstiel, T., Klahr, H., & Ercolano, B., 2012a, *A&A*, 539, id.A148
- Birnstiel, T., Andrews, S. M., & Ercolano, 2012b, *A&A*, 544, id.A79
- Birnstiel, T., Ormel, C. W., & Dullemond, C. P., 2011, *A&A*, 525, id.A11
- Blake, G. and T. Bergin, 2015, *Nature* 520, 161
- Blum, J. & Münch, M., 1993, *Icarus*, 106, 151
- Blum, J. & Wurm, G., 2000, *Icarus*, 143, 138
- Blum, J., Wurm, G., Kempf, S., et al., 2000, *Phys. Rev. Lett.*, 85, 2426
- Bohren, C., & Huffman, D. R., 1983, *Absorption and Scattering of Light by Small Particles*, Wiley Press, New York
- Brauer, F., Dullemond, C. P., & Henning, Th., 2008, *A&A*, 480, 859
- Bridges, F. G., Supulver, K. D., Lin, D. N. C., et al., 1996, *Icarus*, 123, 422
- Carballido, A., Cuzzi, J. N. & Hogan, R. C., 2010, *MNRAS*, 405, 2339
- Carballido, A., Bai, X.-N., & Cuzzi, J. N., 2011, *MNRAS*, 415, 93
- Carballido, A., Stone, J.M., & Turner, N. J., 2008, *MNRAS*, 386, 145
- Carrera, D., Johansen, A., & Davies, M. B., 2015, eprint arXiv:1501.05314
- Cassen, P., 1994, *ApJ*, 112, 405
- Chambers, J. E., 2001, *Icarus*, 152, 205
- Chambers, J. E., 2010, *Icarus*, 208, 505
- Chiang, E. I., & Goldreich, P., 1997 *ApJ*, 490, 368
- Chiang, E. & Youdin, A., 2010, *AREPS*, 38, 493
- Ciesla, F. J., 2009, *Icarus*, 200, 655
- Ciesla, F. J., 2010, *Icarus*, 208, 455
- Ciesla, F. J., 2015, eprint arXiv:1501.01878
- Ciesla, F. J., & Cuzzi, J. N., 2006, *Icarus*, 181, 178
- Clayton, R. N., 2003, *Space Sci. Rev.*, 106, 19
- Connelly, J. N., Bizzarro, M., Krot, A. N., et al., 2012, *Science*, 338, 651
- Cuzzi, J. N., Davis, S. S., & Dobrovolskis, A. R., 2003, *Icarus*, 166, 385
- Cuzzi, J. N., Dobrovolskis, A. R., & Champney, J. M., 1993, *Icarus*, 106, 102
- Cuzzi, J. N., Dobrovolskis, A. R., & Hogan, R. C., 1994, 25th LPSC, 307
- Cuzzi, J. N., Estrada, P. R., & Davis, S. S., 2014, *ApJS*, 210, id. 21
- Cuzzi, J. N.; Hartlep, T.; Weston, B. & Shariff, K., 2014, 45th LPSC, id.2764
- Cuzzi, J. N., & Hogan, R. C. 2003, *Icarus*, 164, 127
- Cuzzi, J. N. & Hogan, R. C., 2012, 43rd LPSC, id.2536
- Cuzzi, J. N., Hogan, R. C. & Bottke, W. F., 2010, *Icarus*, 208, 518
- Cuzzi, J. N., Hogan, R.C., Paque, J. & Dobrovolskis, A.R., 2001, *ApJ*, 546, 496
- Cuzzi, J. N., Hogan, R. C., & Shariff, K., 2008, *ApJ*, 687, 1432
- Cuzzi, J. N., & Weidenschilling, S. J., 2006, In *Meteorites and the Early Solar System II*, 353
- Cuzzi, J. N., & Zahnle, K. J., 2004, *ApJ*, 614, 490
- D'Antona, F., & Mazzitelli, I., 1994, *ApJS*, 90, 467
- Davis, S. S., 2003, *ApJ*, 592, 1193
- Davis, S. S., 2005, *ApJ*, 620, 994
- Desch, S. J., 2007, *ApJ*, 671, 878
- Dominik, C. & Tielens, A. G. G. M., 1997, *ApJ*, 480, 647
- Dominik, C., Blum, J., Cuzzi, J. N., & Wurm, G. 2007, In *Protostars and Planets V*, B. Reipurth, D. Jewitt, and K. Keil, eds., (Tucson: Univ. of Arizona Press), 783
- Donn, B. D., 1990, *A&A*, 235, 441
- Draine, B. T., & Lee, H. M., 1984, *ApJ*, 285, 89
- Drazkowska, J., Windmark, F., & Dullemond, C. P., 2013, *A&A*, 556, id.A37
- Drazkowska, J., Windmark, F., & Dullemond, C. P., 2014, *A&A*, 567, id.A38
- Dubrulle, B., Morfill, G. E., & Sterzik, M., 1995, *Icarus*, 114, 237
- Dubrulle, B., & Valdetaro, L., 1992, *A&A*, 263, 387
- Dullemond, C. P., & Dominik, C., 2005, *A&A*, 434, 971
- Dullemond, C. P., van Zadelhoff, G. J., & Natta, A., 2002, *ApJ*, 389, 464
- Estrada, P. R., & Cuzzi, J. N., 2008, *ApJ*, 682, 515
- Estrada, P. R., & Cuzzi, J. N., 2009, 40th LPSC, #1241
- Estrada, P. R. & Cuzzi, J. N., 2014, 45th LPSC, id.2642
- Estrada, P. R., Mosqueira, I., Lissauer, J. J., D'Angelo, G., & Cruikshank, D. P., 2009, In *Europa*, ed. McKinnon, W., Pappalardo, R., Khurana, K., (Tucson: Univ. of Arizona Press), 27
- Fedkin, A. V. & Grossman, L., 2006, in *Meteorites and the Early Solar System II*, D. S. Lauretta and H. Y. McSween Jr. (eds.), Univ. Az. Press, Tucson, 279
- Ferguson, J. W., Alexander, D. R., Allard, F., Barman, T., Bodnarik, J. G., Hauschildt, P. H., Heffner-Wong, A., & Tamanai, A., 2005, *ApJ*, 623, 585
- Flock, M., Dzyurkevich, N., Klahr, H., Turner, N. J., & Henning, Th., 2011, *ApJ*, 735, 122
- Galvagni, M., Garaud, P., Meru, F., & Olczak, C., 2011, in *Proceedings of the International Summer Institute for Modeling in Astrophysics*, <http://escholarship.ucop.edu/uc/item/7n09f14x>
- Garaud, P., 2007, *ApJ*, 671, 2091
- Garaud, P. & Lin, D. N. C., 2004, *ApJ*, 608, 1050
- Garaud, P., Meru, F., Galvagni, M., and Olczak, C., 2013, *ApJ*, 764, 146
- Goldreich, P. & Ward, W. R., 1973, *ApJ*, 183, 1051
- Goodman, J. & Pindor, B., 2000, *Icarus*, 148, 537
- Grady, M. M., & Wright, I. P., 2003, *Space Sci. Rev.*, 106, 231
- Gressel, O., Nelson, R. P., & Turner, N. J., 2012, *MNRAS*, 422, 1140
- Güttler, C., Krause, M., Geretshauser, R. J., Speith, R., & Blum, J., 2009, *ApJ*, 701, 130
- Güttler, C., Blum, J., Zsom, A., Ormel, C. W., & Dullemond, C. P., 2010, *A&A*, 513, id.A56
- Hartmann, L., Calvet, N., Gullbring, E. & D'Alessio, P., 1998, *ApJ*, 495, 385
- Hayashi, C., 1981, *Prog. Theor. Phys. Supp.*, 70, 35
- Henning, Th., Il'In, V. B., Krivova, N. A., Michel, B., & Voshchinnikov, N. V., 1999, *A&AS*, 311, 405
- Hubbard, A., 2012, *MNRAS*, 426, 784
- Hubbard, A., 2013, *MNRAS*, 432, 1274
- Hueso, R. & Guillot, T., 2003, *Space Sci. Rev.*, 106, 105
- Hughes, A. L. H., & Armitage, P. J., 2010, *ApJ*, 719, 1633
- Hughes, A.L.H. & Armitage, P.J., 2012, *MNRAS*, 423, 389
- Ida, S., Guillot, T., & Morbidelli, A., 2008, *ApJ*, 686, 1292
- Johansen, A., Blum, J., Tanaka, H., et al., 2014, In *Protostars and Planets VI*, H. Beuther, R. S. Klessen, C. P. Dullemond, & Th. Henning (eds.), Univ. Az. Press, Tucson, 547
- Johansen, A., Brauer, F., Dullemond, C., et al., 2008, *A&A*, 486, 597
- Johansen, A., E. Jacquet, J. N. Cuzzi, et al., 2015, in *Asteroids IV*; P. Michel, F. E. DeMeo & W. F. Bottke, Jr.(eds.), Univ. Az. Press, Tucson; in press
- Johansen, A., Henning, T., & Klahr, H., 2006, *ApJ*, 643, 1219
- Johansen, A., Klahr, H., & Henning, Th., 2011, *A&A*, 529, id.A62
- Johansen, A., Oishi, J. S., MacLow, M.-M., Klahr, H., Henning, T. & Youdin, A., 2007, *Nature*, 448, 1022
- Johansen, A., Youdin, A. & Mac Low, M.-M., 2009, *ApJL*, 704, L75

- Jozwiak, D. E., Brownlee, D. E., Matrajt, et al., 2012, *Meteor. Plan. Sci.*, 47, 471
- Kalyaan, A., & Desch, S. J., 2015, 46th LPSC meeting, abstract no. 2206
- Kenyon, S. J., & Hartmann, L., 1987, *ApJ*, 323, 714
- Kita, N.T. & Ushikubo, T., 2012, *Meteor. Plan. Sci.*, 47, 1108
- Kita, N. T., Yin, Q.-Z., MacPherson, G. J., et al., 2013, *Meteor. Plan. Sci.*, 48, 1383
- Kornet, K., Rozyczka, M., & Stepinski, T. F., 2004, *A&A*, 417, 151
- Kothe, S., Güttler, C., & Blum, J., 2010, *ApJ*, 725, 1242
- Kusaka, T., Nakano, T., & Hayashi, C., 1970, *Prog. Theor. Phys.* 44, 1580
- Lambrechts M. & Johansen A., 2012, *A&A*, 544, A32.
- Lin, D. N. C., & Papaloizou, J., 1985, In *Protostars and Planets II*, ed. D. C. Black, M. S. Matthews, (Tucson: Univ. Arizona Press), 981
- Lynden-Bell, D., & Pringle, J. E., 1974, *MNRAS*, 168, 603
- Lyons, J. R., & Young, E. D., 2005, *Nature*, 435, 317
- Lyons, J. R., Bergin, E. A., Ciesla, F. J., et al., 2009, *Geochimica et Cosmochimica Acta*, 73, 4998
- Marcus, P., Pei, S., Jiang, & Hassanzadeh, P., 2013, *Phys. Rev. Lett.*, 111, 084501
- Marcus, P., Pei, S., Jiang, et al., 2014, arXiv:1410.8143
- McKeegan, K. D., Jarzembinski, G. J., Kallio, A. P., et al., 2008, 39th LPSC, March 10-14, League City, TX, no. 1321
- Meakin, P. & Donn, B., 1988, *ApJ*, 329, L39
- Min, M., Dullemond, C. P., Kama, M., & Dominik, C., 2011, *Icarus*, 212, 416
- Morfill, G. E., & Völk, H. J., 1984, *ApJ*, 287, 371
- Nakagawa, Y., Sekiya, M., & Hayashi, C. 1986, *Icarus*, 67, 375
- Nakamoto, T., & Nakagawa, Y., 1994, *ApJ*, 421, 640
- Nelson, R. P. & Gressel, O., 2010, *MNRAS*, 409, 639
- Nelson, R. P., O. Gressel, & O. M. Umurhan, 2013, *MNRAS*, 435, 3, 2610
- Öberg, K. I. et al., 2015, *Nature* 520, 198
- Okuzumi, S., Tanaka, H., Kobayashi, H., & Wada, K., 2012, *ApJ*, 106, 18pp
- Ormel, C. W., & Cuzzi, J. N. 2007, *A&A*, 413, 466
- Ormel, C. W., Cuzzi, J. N., & Tielens, A. G. G. M., 2008, *ApJ*, 679, 1588
- Ormel, C. W. & H. H. Klahr, 2010, *A&A*, 520, A43
- Ormel, C., & Okuzumi S., 2013, *ApJ*, 771, id. 44
- Pan, L. & Padoan, P., 2010, *J. Flu. Mech.*, 661, 73
- Pan, L. & Padoan, P., 2013, *ApJ*, 776, id.12, 37pp
- Pan, L. & Padoan, P., 2014, *ApJ*, 797, id. 101
- Pan, L., Padoan, P. & Scalo, J., 2014a, *ApJ*, 791, id. 48
- Pan, L., Padoan, P. & Scalo, J., 2014b, *ApJ*, 792, id. 69
- Paraskov, G. B., Wurm, G., & Krauss, O., 2007, *Icarus*, 191, 779
- Partnership, ALMA, et al., 2015, arXiv:1503.02649
- Pasek, M. A., Milsom, J. A., Ciesla, F. J., et al., 2005, *Icarus*, 175, 1
- Podolak, M., Pollack, J. B., & Reynolds, R. T., *Icarus*, 73, 163
- Pollack, J. B., Hollenbach, D., Beckwith, S., Simonelli, D. P., Roush, D. P., & Fong, W., 1994, *ApJ*, 421, 615
- Press, W. H., Teukolsky, S. A., Vetterling, W. T., & Flannery, B. P. 1992, *Numerical Recipes in Fortran: 2nd edition*, Cambridge University Press.
- Pringle, J. E., 1981, *ARA&A*, 19, 137
- Rafikov, R. R., 2005, *ApJL*, 621, L69.
- Raymond, S. N., Kokubo, E., Morbidelli, A., Morishima, R. & Walsh, K. J., 2014, In *Protostars and Planets VI*, H. Beuther, R. S. Klessen, C. P. Dullemond, and Th. Henning (eds.), Univ. Az. Press, Tucson, 595
- Ruden, S. P., & Pollack, J. B., 1991, *ApJ*, 375, 740
- Safronov, V. S., 1972, "Evolution of the protoplanetary cloud and formation of the Earth and planets"; Translated from Russian. Jerusalem (Israel): Israel Program for Scientific Translations, Keter Publishing House
- Safronov, V. S., 1991, *Icarus*, 94, 260
- Schräpler, R., Henning, T., 2004, *ApJ*, 614, 960
- Schräpler, R., & Blum, J., 2011, *ApJ*, 734, 108
- Sekiya, M., 1983, *Prog. Theo. Phys.*, 69, 1116
- Simon, J. I., Matzel, J. E. P., Simon, S. B., et al., 2012, 43rd LPSC, March 19-23, The Woodlands, Texas. LPI Contribution No. 1659, id.1340
- Shakura, N. I., & Sunyaev, R. A., 1973, *A&A*, 24, 337
- Shu, F. H., 1977, *ApJ*, 214, 488
- Smoluchowski, M., 1916, *Phys. Z.*, 17, 557
- Stepinski, T. F., 1998, *ApJ*, 507, 361
- Stepinski, T. F. & P. Valageas, 1996, *A&A*, 309, 301
- Stepinski, T. F. & P. Valageas, 1997, *A&A*, 319, 1007
- Stevenson, D., 1990, *ApJ*, 348, 730
- Stewart, S. T., & Leinhardt, Z. M., 2009, *ApJL*, 691, L133
- Stoll, M. H. R. & Kley, W., 2014, *A&A* 572, id.A77
- Supulver, K. D., & Lin, D. N. C., 2000, *Icarus*, 146, 525
- Takeuchi, T., & Lin, D. N. C., 2002, *ApJ*, 581, 1344
- Teiser, J., & Wurm, J., 2009, *MNRAS*, 393, 1584
- Testi, L., Birnstiel, T., Ricci, L., et al., 2014, in *Protostars and Planets VI*, H. Beuther, R. S. Klessen, C. P. Dullemond, and Th. Henning (eds.), Univ. Az. Press, Tucson, 339
- Tanaka, H., Himeno, Y., & Ida, S., 2005, *ApJ*, 625, 414
- Toomre, A., 1964, *ApJ*, 139, 1217.
- Turner, N. J., Fromang, S., Gammie, C., et al., 2014, in *Protostars and Planets VI*, H. Beuther, R. S. Klessen, C. P. Dullemond, and Th. Henning (eds.), Univ. Az. Press, Tucson, 666; eprint arXiv:1401.7306
- van de Hulst, H. C., 1980, *Multiple Light Scattering*, Vols. 1 and 2. Academic Press, New York
- Völk, H. J., Jones, F. C., Morfill, G. E., & Roeser, S., 1980, *A&A*, 85, 316
- Wada, K., Tanaka, H., Suyama, T. Kumura, H., & Yamamoto, T., 2009, *ApJ*, 702, 1490
- Wada, K., Tanaka, H., Okuzumi, S., Kobayashi, H., Suyama, T., Kimura, H., & Yamamoto, T., 2013, *A&A*, 559, id.A62
- Weidenschilling, S. J., 1977, *MNRAS*, 180, 57
- Weidenschilling, S. J., 1980, *Icarus*, 44, 172
- Weidenschilling, S. J., 1984, *Icarus*, 60, 553
- Weidenschilling, S. J., 1988, in *Meteorites and the Early Solar System* (J. Kerridge and M. S. Matthews, Eds.), Univ. Arizona press, Tucson, 348
- Weidenschilling, S. J., 1995, *Icarus*, 116, 433
- Weidenschilling, S. J., 1997, *Icarus*, 127, 290
- Weidenschilling, S. J., 2000, *Space Sci. Rev.*, 92, 295
- Weidenschilling, S., 2004, in *Comets II*, M. C. Festou, H. U. Keller, & H. A. Weaver (eds.), Univ. Ariz. Press, Tucson, 97
- Weidenschilling, S., 2006, *Icarus*, 181, 572
- Weidenschilling S. J., 2011, *Icarus*, 214, 671.
- Weidenschilling, S. J., & Cuzzi, J. N., 1993, In *Protostars and Planets III*, ed. E. H. Levy & J. I. Lunine (Tucson: Univ. Arizona Press), 1031
- Weidenschilling, S. J., Donn, B., & Meakin, P., 1989, in "The formation and evolution of planetary systems; Proceedings of the Meeting", Baltimore, MD, May 9-11, 1988 (A90-31251 12-90). Cambridge and New York, Cambridge University Press, 131-146; Discussion, p. 146-150.
- Weidling, R., Güttler, C., & Blum, J., 2012, *Icarus*, 218, 688
- Windmark, F., Birnstiel, T., Güttler, C., et al., 2012a, *A&A*, 540, id.A73
- Windmark, F., Birnstiel, T., Ormel, C. W., & Dullemond, C. P., 2012b, *A&A*, 544, L16
- Windmark, F., Birnstiel, T.; Ormel, C. W. & Dullemond, C. P., 2013, *Protostars and Planets VI* conference, Heidelberg, July 15-20, 2013. Poster #2B090
- Woolum, D. S., & Cassen, P., 1999, *Meteor. Plan. Sci.*, 34, 897
- Wurm, G., Paraskov, G. B., & Krauss, O., 2005, *Icarus*, 178, 253
- Yang, L., & Ciesla, F. J., 2012, *Meteor. Plan. Sci.*, 47, 99
- Yang, L., Ciesla, F. J., & Alexander, C. M. O'D., 2013, *Icarus*, 226, 256
- Youdin, A. N. & Goodman, J., 2005, *ApJ*, 620, 459
- Youdin, A., & Lithwick, Y., *Icarus*, 192, 588
- Yurimoto, H., Itoh, S., & Krot, A. N., 2005, *Workshop on Oxygen in the Earliest Solar System*, September 19-21, Gatlinburg, Tennessee, LPI Contribution No. 1278., p.39
- Yurimoto, H., Kuramoto, K., Krot, A. N., et al., 2007, in *Protostars and Planets V*, B. Reipurth, D. Jewitt, and K. Keil (eds.), Univ. Az. Press, Tucson, 849
- Zolensky, M. E., & 75 coauthors, 2006, *Science*, 314, 1735
- Zsom, A., Ormel, C. W., Güttler, C., Blum, J., & Dullemond, C. P., 2010, *A&A*, 513, id.A57
- Zsom, A., Sándor, Z., & Dullemond, C. P., 2011, *A&A*, 527, id.A10